Studies on Radioactive Background Mitigation for the PICO-500 Dark Matter Search Experiment

by

Shawn Paul Miller-Chikowski

A thesis submitted in partial fulfillment of the requirements for the degree of

Master of Science

Department of Physics
University of Alberta

Abstract

The PICO-500 dark matter search experiment features the next-generation bubble chamber detector designed by the PICO collaboration. The sensitivity and live-time of ultra-low background detectors, such as PICO-500, are crucially dependent on the radio-pure materials used in the construction. The PICO-500 detector is anticipated to achieve world-leading sensitivity in the spin-dependent dark matter regime, necessitating radioactive background control during the construction and assembly.

This thesis focuses on strategies and measurements related to mitigating radioactive backgrounds, specifically focusing on Radon-222, a gaseous and radioactive product of the Uranium-238 decay chain, and its progeny. The diffusive nature of radon prompts investigation into radon emanation from detector materials and radon permeation through a Parker PTFE Prädifa series NAE, FlexiSeal®, which is to be used in the PICO-500 inner vessel. The Parker PTFE seal permeation coefficient was determined using a noble gas extrapolation method and direct measurement using a radon emanation chamber detector, yielding $5.10^{+0.92}_{-1.10} \times 10^{-10}$ $\frac{\text{cm}^3\text{(STP)}\cdot\text{cm}}{\text{s}\cdot\text{cm}^2\cdot\text{cm-Hg}}$ and $5.37 \pm 0.49 \times 10^{-10}$ $\frac{\text{cm}^3\text{(STP)}\cdot\text{cm}}{\text{s}\cdot\text{cm}^2\cdot\text{cm-Hg}}$, respectively. The radon activity contribution from the PTFE seals in the PICO-500 detection volume was estimated to be 30.5 Radons/Day.

To prepare for the deployment of PICO-500, studies establishing cleaning strategies for the synthetic quartz vessels were developed. Full-sized PICO-500 natural quartz vessels were subjected to tests using ultra-pure water soap solutions to remove dust and particulates, which can also act as carriers for radon progeny. Using a 0.05-micron filtration and a customized cleaning system built at the UofA, surfaces of the vessels were documented to be cleaned to the IEST-STD-CC1246D-25 standard. Techniques to reach this standard consistently were developed for the synthetic quartz cleaning of PICO-500, which will be implemented at the SNOLAB facility.

Dedicated to my grandma, Donna Courchene (Chikowski), who is no longer with us

Owe onji egichi-apiitenimag ningookom-iban, Donna Courchene (Chikowski), gaawiin awaashime omaa e-ayaasig

Bigo miigwech ji-ikidoyaan owe onji miinigowisiwin zhigo gojijigewin gaagii-miiniyan. Nawaj awaashime gigii-miinzh apiich gaagii-inendaman. Mii zhigo omaa nindayaa megwaa. Zhigo sago gegiin. Apane'igo giga-bimaadiz ninde'ing zhigo omaa ozhibii'iganan. Gizaagi'in!

Translated by Wanda Baker and Jerry Sinclair

Acknowledgements

First and foremost, I would like to thank my sponsors, the Sagkeeng Anicinabe Nation, as I would not have had the opportunity to pursue this journey without their financial support.

I would like to give special thanks to my supervisor, Dr. Carsten Krauss. I am deeply grateful for his mentorship and invaluable teachings that have been instrumental in shaping my research journey. His guidance and support played a vital role in my personal and academic growth, empowering me to achieve milestones that I never thought possible. I owe a special debt of gratitude to him for his belief in my abilities and for fostering my development as a researcher. Additional thanks to the PICO collaboration for their high level of professionalism and valuable input, as well as the support staff and all members of the local PICO team at the University of Alberta, including Richard Soluk, David Auty, Michael Rangen, and the Physics Machine Shop personnel, with special thanks to Tony Vinagreiro.

I would like to thank my father, Shawn Chikowski, my mother, Tammy Miller-Bryant, Todd Bryant, my siblings, Kelsey Miller and Stealth Chikowski, and my partner, Jena Chengalanee, and her family. Their support, even if they may not fully comprehend my research, has been a source of strength and motivation throughout this journey.

To all my friends and family who have contributed in any way who were not mentioned above, I extend my deepest gratitude for your support, encouragement, and belief in my abilities. This thesis would not have been possible without your help and the help from those mentioned above. Thank you.

Table of Contents

List of Tables

List of Figures

List of Abbreviations

List of commonly used abbreviations

ADC	Analog to Digital Converter
Bi	Bismuth
CMB	Cosmic Microwave Background
DAQ	Data Acquisition
DM	Dark Matter
GeV	Giga-electronVolt
GPC	Gas Permeation Chamber
HDPE	High-density Polyethylene
HV	High Voltage
MeV	Mega-electronVolt
N_2	Nitrogen Gas
Pb	Lead
Po	Polonium
PTFE	Polytetrafluoroethylene
Ra	Radium
Rn	Radon
ROI	Region of Interest
Th	Thorium
TPC	Time Projection Chamber
U	Uranium
ULB	Ultra-Low Background
UofA	University of Alberta
UPW	Ultra-Pure Water
WIMP	Weakly Interacting Massive Particle

List of Symbols

List of commonly used symbols

α	Alpha Particle
β	Beta Particle
γ	Gamma Particle
ϵ	Detector Efficiency
A	Activity
C	Concentration
E	Emanation Rate
K_p	Permeation Coefficient
N_A	Avogadro's Constant
n	Moles
$\dot{n}$	Molar Flow Rate
P	Pressure
Q	Volumetric Flow Rate
R	Universal Gas Constant
r_{perm}	Permeation Rate Constant
S	Active Permeation Surface Area
T	Temperature
V	Volume

Chapter 1

Introduction

The mystery of dark matter is one of the longest unsolved problems in physics [1–3]. Astrophysical observations have shown that dark matter outweighs baryonic matter six to one and comprises 25% [4] of the universe, yet its nature is unresolved. Dark matter does not emit or absorb light (dark), and has only been measured through its gravitational effects (matter) on galactic scales. A leading theory, which will be discussed in more detail in Chapter 2, is that dark matter is a weakly interacting massive non-standard model particle referred to as a WIMP (Weakly Interacting Massive Particle) [5].

Addressing the dark matter problem has required considerable effort. Beyond the theoretical explorations and astronomical observations, there are many ongoing experiments focused on the direct detection of dark matter (Chapter 3) using ultra-low background detectors. A potential signal, suggestive of WIMP interactions, could be identified through a nuclear recoil event where a WIMP undergoes coherent elastic scattering off the nucleus of a target material atom. In this process, the coherence refers to the interaction of the WIMP with the entire atomic nucleus. The nuclear recoil is then the displacement of the target nucleus due to the kinetic energy transfer from the WIMP during the interaction. The energy deposition can be observed as heat, vibrations, light emission, radiation, ionization, or through the generation of secondary particles.

However, direct detection experiments face significant challenges beyond just identifying potential WIMP interactions. For instance, alpha decay—where an unstable nucleus emits a helium nucleus composed of two protons and two neutrons—introduces

background events as these alpha particles can deposit energy in the detector medium. Radon, a ubiquitous alpha-decaying radioactive gas, along with its decay products, represent a dominant source of radioactive backgrounds. Thus, to enhance the reliability and precision of ultra-low background detectors, selecting materials with minimal radon permeation and emanation rates is crucial.

Radon permeation involves the diffusion of radon gas through solid materials, with the rate of permeation influenced by several factors: the characteristics of radon gas, material properties such as thickness, surface area, and composition, as well as environmental conditions like temperature and pressure. Radon emanation, on the other hand, refers to the emission of radon gas from materials containing traces of uranium or thorium. Radon arises from the uranium and thorium decay chains, which end in stable isotopes, Lead-206 and Lead-208, respectively. Radon-222, a byproduct of the uranium decay chain, is gaseous under standard conditions, facilitating its diffusion within its surrounding environment. Two subsequent decay products of Radon-222, Lead-210 and Polonium-210, pose challenges for ultra-low background detectors for two primary reasons: Lead-210 possesses a half-life of 22.2 years [6], and Polonium-210 undergoes alpha decay. This alpha decay can produce a signal in ultra-low background detectors and, because of the 22.2 year half-life of Lead-210, would provide a steady background rate for the duration of low background experiments.

To achieve competitive detector sensitivity, the next-generation PICO dark matter detector will utilize a spring-energized seal design, which is a flange seal Prädifa series NAE, FlexiSeal® [7] manufactured by Parker and will be used within the inner vessel of the detector. This seal design incorporates a PTFE jacket encasing a cobalt-chromium-nickel helical spring, which offers two primary advantages: a low radon emanation rate (Appendix A), and reliable sealing performance in the -216°C to $+350$°C temperature range [7]. While this seal exhibits low radon emanation, the rate of radon permeation through the seal has not been investigated in literature.

In the next two chapters, aspects related to dark matter and direct detection are

discussed. Chapter 2 provides an overview of the dark matter phenomenon and presents evidence supporting its existence as a non-standard model particle, while Chapter 3 introduces direct detection experiments searching for WIMPs.

In Chapter 4, discussions on radon, its progeny, and an introduction to the recommissioned Radon Emanation Chamber, designed and constructed at the University of Alberta are presented.

Chapter 5 is centered on two distinct measurements of the radon permeability through the PTFE-encased spring-energized seal, which will be referred to as the Parker PTFE seal in this thesis. The initial method extrapolates the radon permeation coefficient using experimentally determined permeation coefficients of the five lower mass noble gases (Helium, Neon, Argon, Krypton, and Xenon) through a Parker PTFE seal, as a function of atomic diameter. The subsequent method involves a direct measurement of the radon permeation rate utilizing the Radon Emanation Chamber detector, from which the permeation coefficient is calculated. Quantifying the permeability of radon through the Parker PTFE seal is important for estimating the expected background rate for the PICO-500 dark matter search experiment.

Chapter 6 outlines the cleaning processes and radon mitigation measures applied to the PICO-500 replica natural quartz vessels, including an analysis of ultra-pure water samples to assess cleanliness levels. These steps are to be applied to the cleaning of the synthetic quartz vessels, which will be used in the PICO-500 detector. By developing a quantifiable cleaning process, potential background sources, such as dust (whether radioactive or non-radioactive) particulates and direct radon contamination, are mitigated.

In this thesis, the evaluation of radon permeation behavior and the development of cleaning procedures specifically aim to address radioactive background mitigation for the PICO-500 dark matter search experiment. The goal of this research is to enhance the reliability and precision of future dark matter detection experiments, particularly those utilizing synthetic quartz vessels.

Chapter 2

Evidence for Dark Matter

Evidence of a 'missing mass' problem first emerged from astronomical studies in the early 20th century [2, 3]. The existence of dark matter is primarily inferred from its gravitational effects observed on galactic scales, with the supporting evidence coming from studies of cluster and galactic dynamics [2, 8], mass distributions in galactic collisions [9], and temperature fluctuations within the Cosmic Microwave Background [4]. Notably, analysis of the Cosmic Microwave Background angular power spectrum suggests the potential existence of a particle not predicted by the Standard Model of Particle Physics, thus reinforcing the concept that dark matter is a yet-to-be-discovered particle.

2.1 Cluster Dynamics and Galactic Rotation Curves

In his seminal 1933 paper, 'Die Rotverschiebung von extragalaktischen Nebeln,' Fritz Zwicky provided evidence of 'missing mass' within the Coma Cluster [2]. Using redshift observations made by Edwin Hubble and Milton Humason from a 1931 publication titled "The Velocity-Distance Relation among Extra-Galactic Nebulae" [10], Zwicky found the average dispersion velocity of the cluster. By applying the Virial Theorem, Zwicky calculated the mass of the cluster. The Virial Theorem relates the time-averaged kinetic energy of a system in dynamic equilibrium to its potential energy, in this case, attributed to gravitational forces. Zwicky's assumption that the Virial Theorem could extend to applications beyond traditional thermodynamic systems was controversial at the time [11].

Zwicky's approach also involved estimating the total luminous mass within the Coma Cluster. He counted 800 galaxies, assuming each had a mass of 10^9 solar masses. Utilizing the Virial Theorem, he solved for the velocity dispersion, calculated to be 80 km/s [2, 3]. However, Doppler-shift measurements of emission lines from galaxies revealed an average velocity dispersion exceeding 1000 km/s [2, 3]. This significant discrepancy between the two methods to calculate the velocity dispersion indicates a mass density at least 400 times greater than that accounted for by luminous matter alone.

Zwicky revisited his investigations in a subsequent 1937 paper, refining his calculations regarding the Coma Cluster. Here, he identified an even larger discrepancy, with a mass density 500 times greater than what luminous matter could account for [12]. It is important to note, however, that Zwicky's calculations utilized a now outdated value for the Hubble constant ($H_0 = 558$ km/s/Mpc [12]) for galactic distance calculations. The currently accepted Hubble Constant is 69.8 ± 0.8 km/s/Mpc [4], which leads to a reduced mass-to-light ratio. Despite this, the fundamental observation remains unchanged: a substantial amount of matter exists that neither emits nor absorbs light. Zwicky referred to this missing mass as "dunkle Materie" (Dark Matter) [2], and the term has persisted in scientific discourse ever since.

Though Fritz Zwicky's application of the Virial Theorem applied to galactic clusters was not taken seriously at the time, more convincing evidence for the existence of dark matter emerged from gravitational anomalies observed by Vera Rubin and Kent Ford decades later. In 1970, Rubin and Ford's work, made possible by the advancement of a more precise spectrograph, revealed nearly constant orbital velocities of stars at the outer edges of galaxies, regardless of their distance from the centre (Figure 2.1) [8]. The anticipated radial dependence of the orbital velocity curve has two components: a linearly increasing relationship for stars within the galactic nucleus (approximated as a solid body) and a decreasing Keplerian curve beyond this dense region. In other words, Kepler's third law predicts that stars farther from the galactic nucleus should

display decreased orbital velocities proportional to $\frac{1}{\sqrt{R}}$ due to reduced mass density in the outer layer of galaxies. Yet, observations contradict this expectation, implying the presence of unseen mass at the outer edges of the galaxy [8]. To explain the anomalous orbital velocities in the outer edges, the unseen mass is hypothesized to be distributed in a spherical halo-like structure around the galaxy [13].

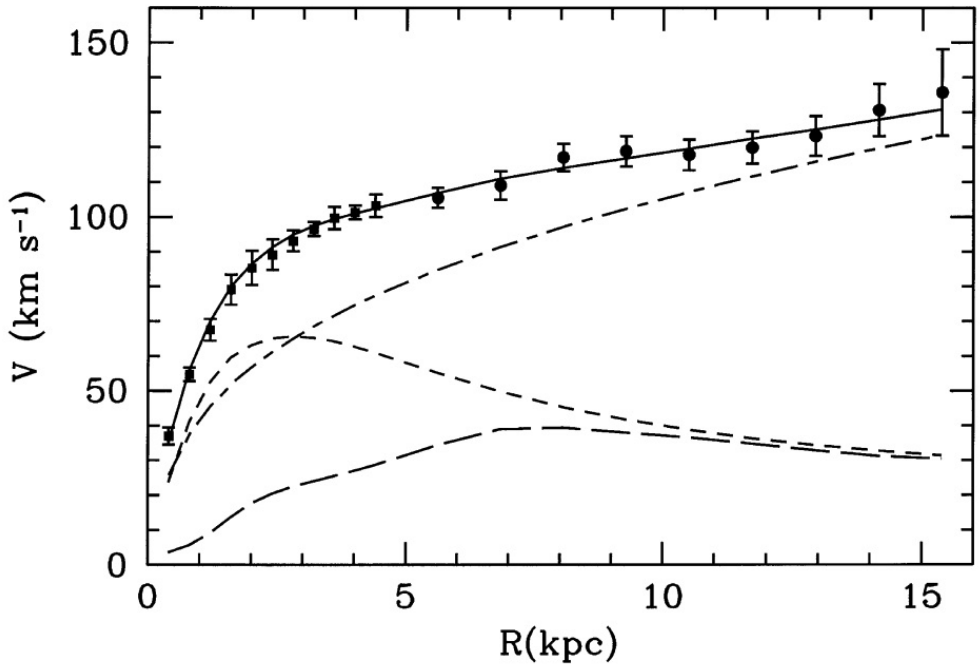

Figure 2.1: Rotation curve of the spiral galaxy M33. The solid line represents the best fit to the observational data. The dot-dashed, short-dashed, and long-dashed lines correspond to contributions from the halo, stellar disc, and gas, respectively [13].

A great example of a spiral galaxy exhibiting a mass discrepancy is Messier33 (M33). The galaxy's rotation curve is derived from Doppler shifts of the HI (21-cm line) emission of neutral hydrogen. Corbelli et al determined a dark halo mass of $5 \times 10^{10} M_{\odot}$ ($M_{\odot} = 1$ Solar Mass) and luminous baryonic matter (primarily gas) of $3 \times 10^{9} M_{\odot}$. Thus, approximately 95% of the mass of M33 is attributed to dark matter [13].

2.2 The Bullet Cluster

Another gravitational anomaly arises when examining the collision of clusters of galaxies. The study of these types of collisions facilitates mapping gravitational fields through gravitational lensing, a prediction of Einstein's general relativity, where light paths bend within gravitational fields. Strong lensing, caused by dense regions of mass, may generate multiple images or a ring of a background source (Figure 2.2), while galactic weak lensing can cause subtle galaxy shape distortions, which is key for studying large-scale gravitational distributions.

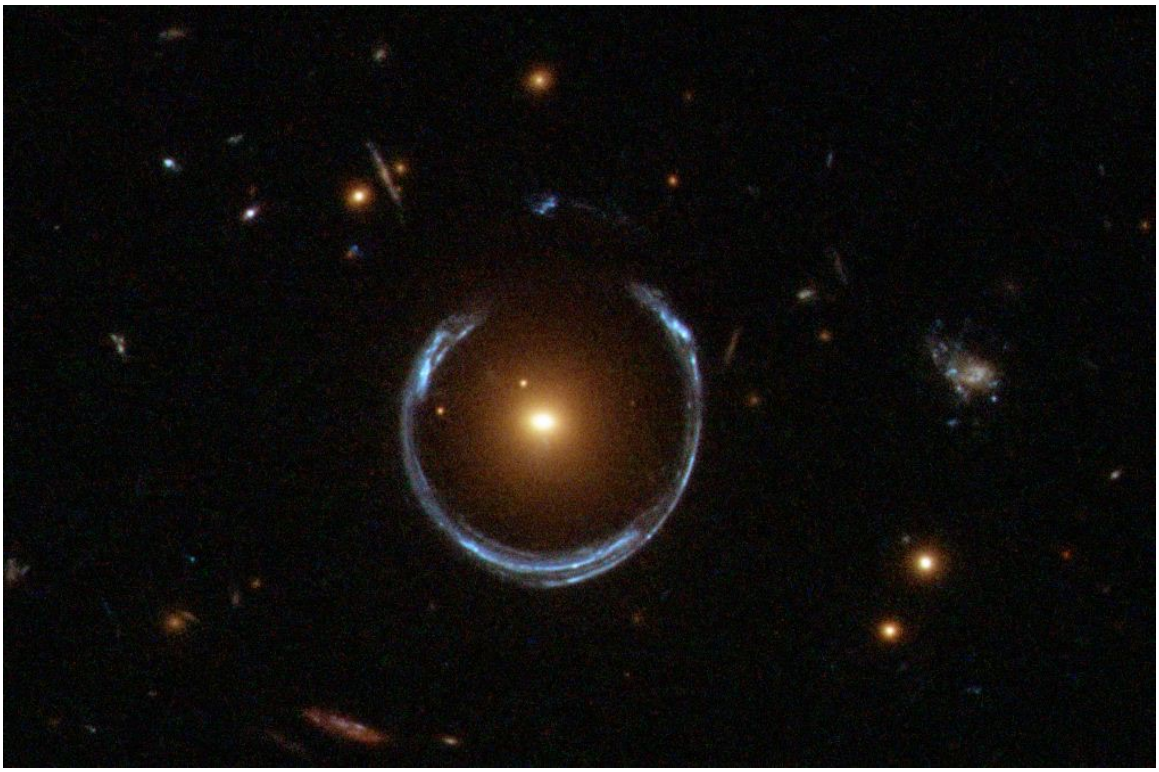

Figure 2.2: Cosmic Horseshoe (lensed galaxy SDSS J1148+1930): an example of strong gravitational lensing, displaying a distinct arc-like formation of light emitted from a background galaxy. The galaxy is significantly distorted and intensified by the gravitational influence of a massive foreground galaxy cluster. Credit: ESA/Hubble & NASA, CC BY 4.0 [14].

In the Bullet Cluster (1E 0657-56) collision between two galaxy clusters, weak lensing reveals the total mass distribution of the system. Figure 2.3 shows two regions:

the blue region, which outlines this mass distribution from weak lensing, and the magenta region, which shows the baryonic gas of the colliding galaxy clusters, visualized through x-ray emissions from the Chandra Observatory. During the collision, the gas interacted and was heated up to temperatures of 10^6 K, emitting X-rays. The interaction caused the gas of the two clusters to effectively slow down due to friction-forces. Consequently, they now trail behind the galaxies. Observations of the post-collision mass distribution reveal that it is largely separate from the hot galactic gas. This suggests that the majority of mass in the galaxies only interacts gravitationally as it passes through unimpeded. Further, the comparison of centre-of-mass calculations show that the total mass to hot gas is a factor seven times greater [15].

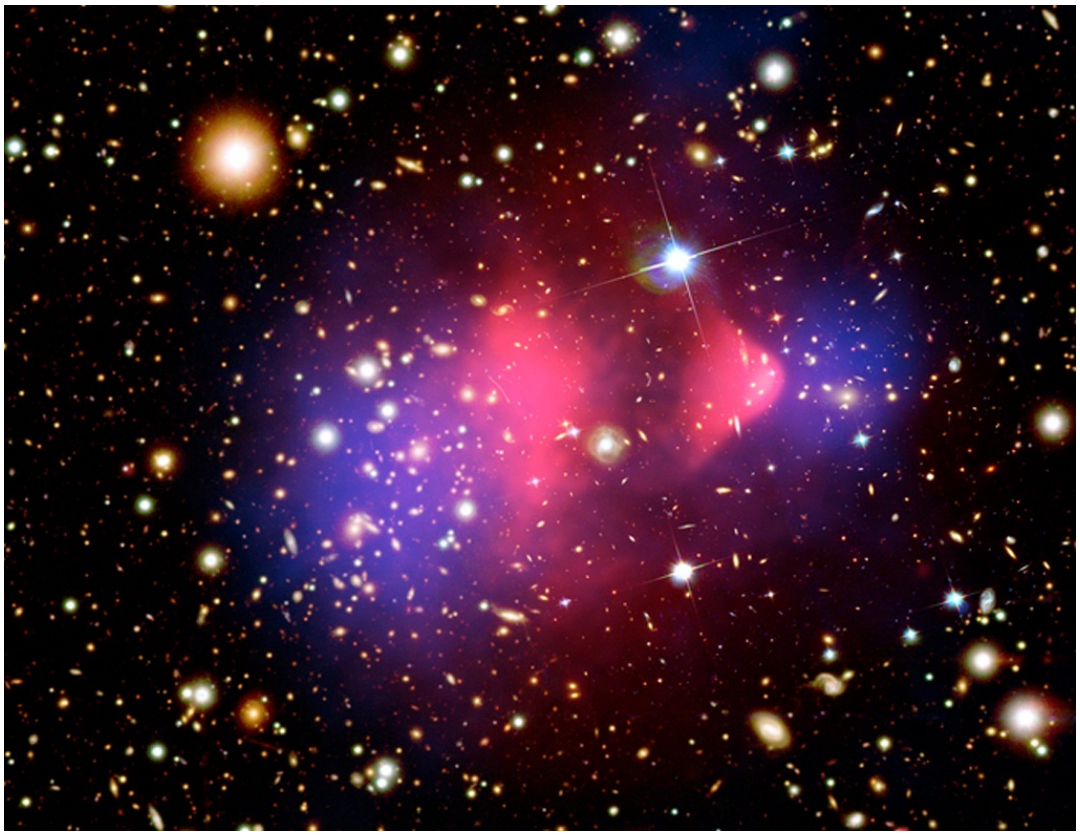

Figure 2.3: Mass distribution of the Bullet Cluster. The blue regions are locations of strong gravitational fields, while the magenta regions are areas of atomic hydrogen implying there is more mass in the cluster that is not visible. Credit: X-ray: NASA/CXC/CfA/M.Markevitch et al.; Optical: NASA/STScI; Magellan/U.Arizona/D.Clowe et al.; Lensing Map: NASA/STScI; ESO WFI; Magellan/U.Arizona/D.Clowe et al [9], CC BY 4.0.

2.3 The Cosmic Microwave Background

The Cosmic Microwave Background is the residual radiation from the early universe, appearing about 380,000 years after the Big Bang. Initially, the universe was a hot, dense plasma consisting of protons, electrons, and photons. As the universe expanded and cooled, reaching about 3000 K, electrons and protons combined during the epoch of recombination, forming the first hydrogen atoms. This reduced Thomson scattering, an elastic scattering process where low-energy photons interact with free, charged particles. Photons were able to propagate freely, marking the transition from an opaque universe to a transparent one. The Cosmic Microwave Background observed today (Figure 2.4) represents this decoupling era, providing insights into the early universe and dark matter.

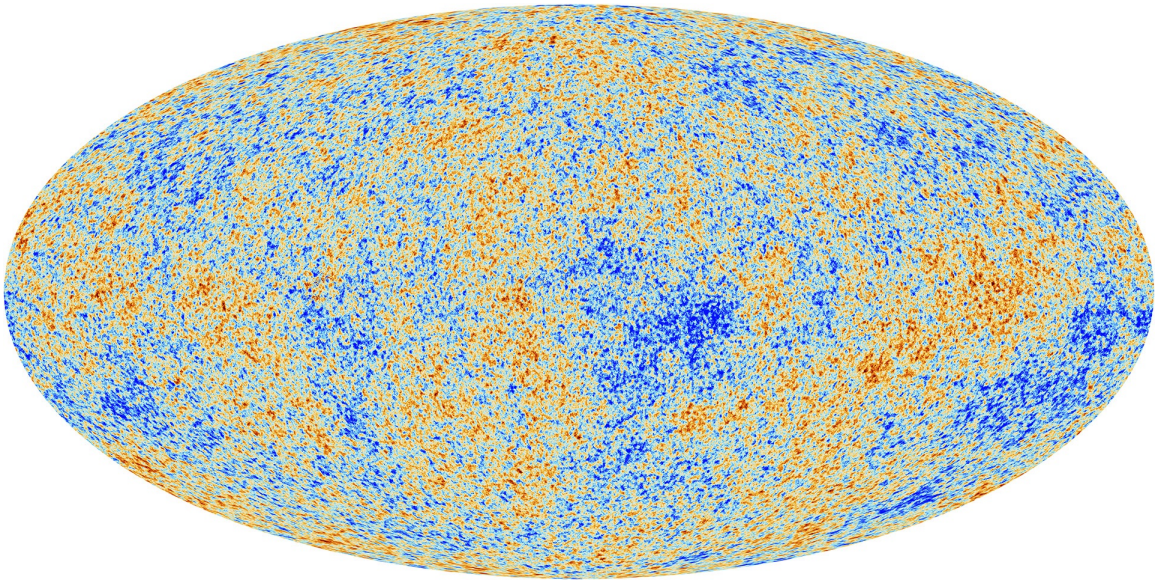

Figure 2.4: Cosmic Microwave Background: a map showing temperature variations, with red areas indicating slightly hotter regions and blue areas representing cooler regions, illustrating the minute fluctuations in the temperature of the early universe. Credit: ESA, Planck Collaboration [16], CC BY 4.0.

Cosmic Microwave Background observations confirm a nearly uniform temperature of 2.7255 ± 0.0004 K [4] with microKelvin-scale anisotropies, which can be partly attributed to dark matter. The Cosmic Microwave Background power spectrum, char-

acterized by distinct peaks at various multipole moments (ℓ), captures the scale of these anisotropies. The multipole moment is related to the inverse of the angular size on the sky, which means large multipole moments are related to smaller angular sizes. Figure 2.5 shows the power spectrum of the Cosmic Microwave Background, which has the magnitude of these temperature fluctuations plotted against the scale at which they occur. The peaks are due to baryon acoustic oscillations, which were a result of two forces in the early universe: gravity and radiation pressure. The push and pull between the radiation pressure and gravity created oscillations in the plasma. The first two peaks, at $\ell \approx 200$ and $\ell \approx 500$, correspond to larger angular scales dominated by baryonic matter interactions, while the third peak, at $\ell \approx 800$, relates to the gravitational influence dark matter had on the early universe. Planck satellite data indicates a dark matter density ($\Omega_c h^2 = 0.120 \pm 0.001$) 5 times greater than that of baryonic matter ($\Omega_b h^2 = 0.0224 \pm 0.0001$) [4]. The symbol h is the reduced Hubble constant. Consequently, dark matter accounts for approximately 27%, baryonic matter for about 5%, and dark energy for roughly 68% of the mass-energy composition of the universe. These proportions make up the ΛCDM cosmological model, integrating the cosmological constant (Λ) for dark energy and Cold Dark Matter (CDM). CDM refers to dark matter that is non-relativistic, allowing dark matter to freeze out of thermal equilibrium after the big bang. Other theoretical models exist postulating the existence of Hot dark matter and Warm dark matter, which are beyond the discussion of this thesis.

2.4 Dark Matter as a Particle

The existence of dark matter is well-supported by astronomical evidence as demonstrated in this chapter; however, its precise nature is still unknown. One hypothesis posits the presence of massive astrophysical compact halo objects (MACHOs) — such as black holes, neutron stars, brown dwarfs, rogue planets, white dwarfs, and faint red giants — within galactic halos. These objects are massive enough to exert gravi-

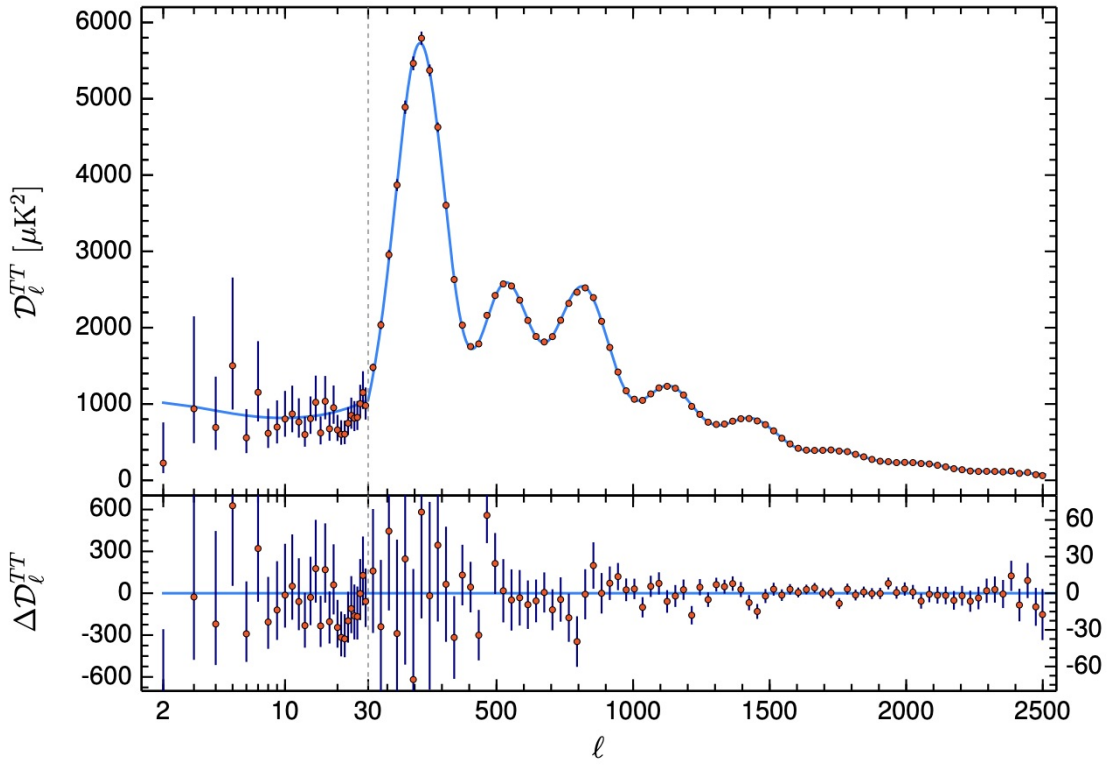

Figure 2.5: Cosmic Microwave Background temperature fluctuations as shown by Planck satellite data, with the vertical axis representing the power spectrum D_ℓ^{TT} and the horizontal axis indicating the multipole moment ℓ [4].

tational effects without emitting detectable light. They potentially contribute to the mass density of the galaxy. However, gravitational microlensing surveys have not identified a sufficient number of these MACHOs to account for the mass density attributed to dark matter [17]. Moreover, MOND (**MO**dified **N**ewtonian **D**ynamics), a theoretical framework that modifies Newtonian gravity, can adequately explain rotational dynamics in most spiral galaxies but fails to account for the shape of the power spectrum of the cosmic microwave background and the gravitational lensing observed in galaxy cluster collisions. An example is the Bullet Cluster, where regions of high mass density align with the non-interacting components of the collision rather than with the visible baryonic matter.

The hypothesis that dark matter consists of a non-standard model particle is consistent with the evidence provided in this chapter. Such a particle must possess mass

to exert gravitational influence and must be non-electromagnetically interacting, as inferred from the Cosmic Microwave Background power spectrum. Neutrinos, though fitting these criteria, are too energetic ('hot') to align with the ΛCDM model. Further, hypotheses like sterile neutrinos also fit the criteria of dark matter well, but sterile neutrinos are expected to decay into X-rays where astronomical searches have not obtained definite results [18]. The leading candidate for dark matter are Weakly Interacting Massive Particles (WIMPs), which are theorized to account for the unseen mass in astronomical observations. WIMPs are believed to be 'cold', have a mass in the GeV-TeV range, and can interact via the weak nuclear force. This posits three strategies for detecting dark matter (Figure 2.6): production in particle colliders such as the Large Hadron Collider (LHC), indirect detection through anomalous decay modes potentially observable in detectors like IceCube, and direct detection via ultra-low background detectors, a topic to be discussed in the following chapter.

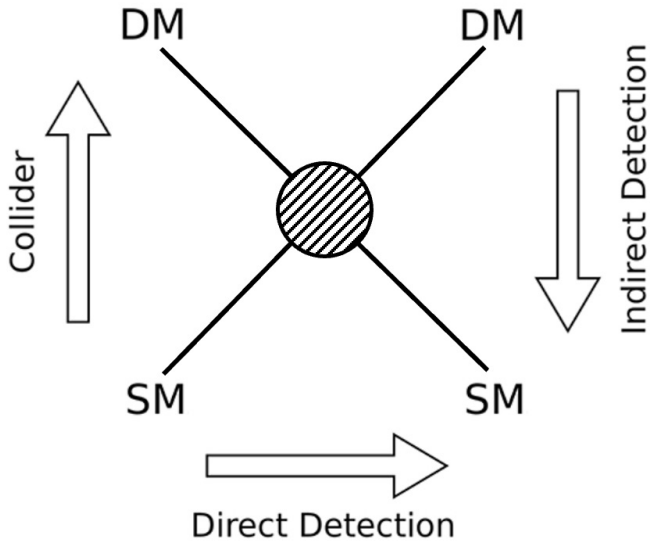

Figure 2.6: Feynman diagram illustrating potential interactions between dark matter particles and standard model particles, depicting processes relevant to collider searches, indirect detection searches, and direct detection experiments. Adapted from [19], CC BY 4.0.

Chapter 3

Searching for Dark Matter

3.1 Dark Matter Interactions

Numerous collaborations, each pursuing a unique approach to dark matter detection, are actively exploring the parameter space of dark matter and pushing the boundaries of engineering to develop increasingly sensitive detectors. The challenge of direct detection of dark matter lies in the weak force interaction, with WIMP-nucleon cross sections, a measure of the probability of an interaction with protons and neutrons, anticipated to be in the range of 10^{-40} to 10^{-50} cm^2 [20]. Exclusion curves, such as those in Figure 3.1, map the parameter space investigated by these dark matter searches, establishing upper limits on the WIMP-nucleon cross section and WIMP mass. Moreover, dark matter interactions are further categorized into spin-independent (SI) and spin-dependent (SD) interactions, which lead to different detector sensitivities.

Spin-independent interactions involve the coupling of a WIMP to the entire nucleus, leading to coherent elastic scattering where the cross section scales with the square of the number of nucleons [21]. Thus, detectors with larger nuclei are more sensitive to WIMP interactions. Beyond the parameter space excluded by dark matter experiments for SI-WIMP interactions, Figure 3.1 also outlines the neutrino fog highlighted by the yellow shaded region. As dark matter experiments approach the neutrino fog, neutrinos will become a background and resemble a WIMP signature. To differentiate these signals, researchers are developing methods such as directional detection to distinguish neutrinos from WIMPs [22].

Spin-dependent interactions are the coupling of WIMPs to the nuclear spin of the

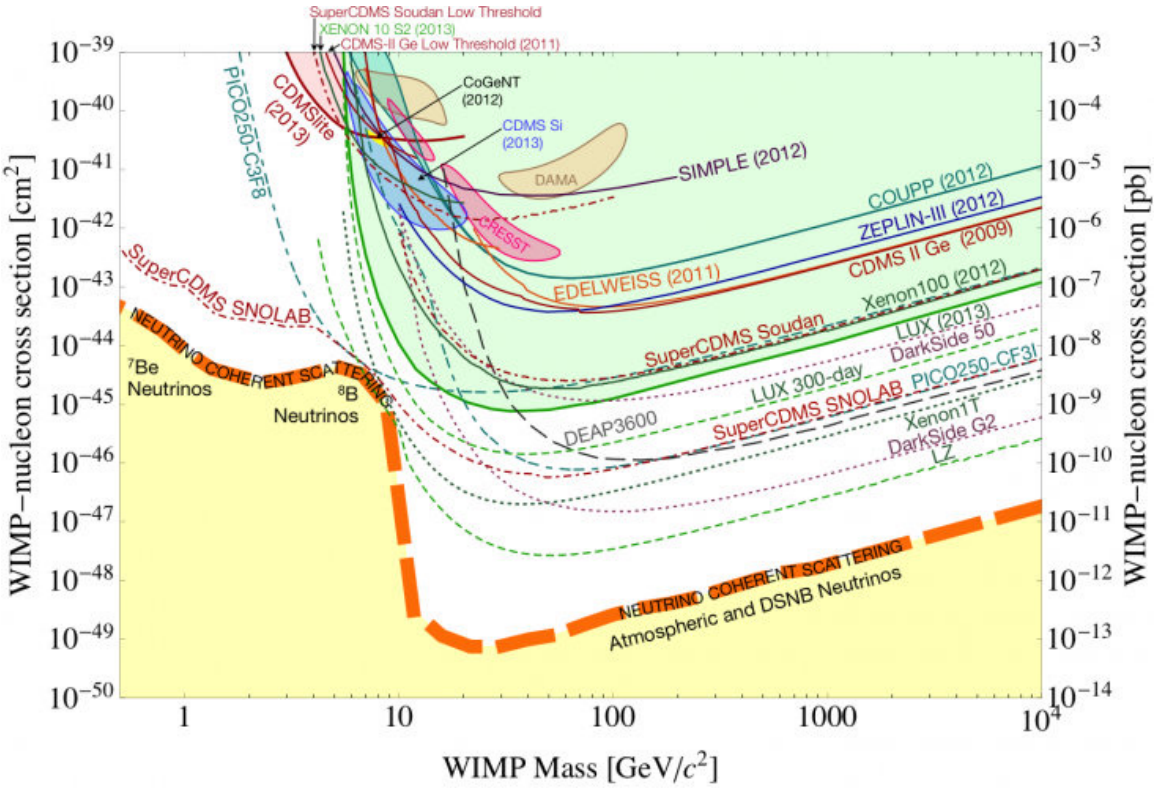

Figure 3.1: Spin-independent dark matter exclusion plot showing the cross section versus WIMP mass with overlaid results from various experiments [23]. The upper shaded regions and curves represent excluded parameter spaces and detector limits. The yellow shaded region highlights the neutrino background. In this region, dark matter and neutrinos are indistinguishable.

atomic nuclei. These interactions are weaker, especially for lighter WIMPs [21]. Targets possessing an unpaired nucleon, such as Fluorine-19 (j=1/2 [24]), are recognized as a good choice for dark matter experiments investigating the SD-WIMP parameter space. This preference is due to the strong spin-dependent coupling resulting from the large nuclear form factor of Fluorine-19.

The signature of a spin-independent or spin-dependent interaction is a nuclear recoil that is measurable by ionization, scintillation, or heat, depending on the design of the detector. Sensitivity to WIMP interactions is affected by cosmic rays and radioactivity-induced backgrounds. To mitigate these effects, placement of dark matter detectors is crucial. SNOLAB, a particle physics research facility located in an active nickel mine two kilometers underground near Sudbury, Ontario, provides a

deep-earth shield equivalent to six kilometers of water against cosmic rays [25]. It is a clean room environment, which further reduces ambient radioactivity, offering an ideal setting for the assembly and operation of dark matter detectors [25].

3.2 Techniques and Experiments in Dark Matter Searches

3.2.1 Solid State Cryogenic Detectors

Solid State Cryogenic Detectors, such as those used in Super Cryogenic Dark Matter Search (SuperCDMS), use semiconductors like silicon and germanium to detect particle interactions through produced electron-hole pairs and thermal signatures. By super-cooling these detectors, thermal noise can be reduced, enhancing the sensitivity to ionization signals and low-intensity phonons that could be the product of a WIMP-nucleon nuclear recoil. SuperCDMS, in particular, utilizes this technology to detect nuclear recoils with masses as low as $5\,\mathrm{GeV}/c^2$. Discrimination against beta and gamma backgrounds can be achieved by comparing the phonon signal to the amplitude of the electrical signal. This sensitivity is important to achieve an expected WIMP cross section of $1 \times 10^{-43}\,\mathrm{cm}^2$ [26]. SuperCDMS is set to operate in SNOLAB.

3.2.2 Liquid Noble Gas TPC Detectors

Time Projection Chambers (TPCs) are among the leading technologies in the search for spin independent dark matter. These detectors use a dual-phase noble gas target to capture the initial scintillation of light (S1) and subsequent scintillation (S2) from a coherent elastic scattering event. Silicon photomultipliers or PMTs detect S1 from the liquid phase, while ionized electrons, a product of the nuclear recoil, drift upward in a strong electric field to the gas phase, inducing S2 scintillations. Photomultipliers activated by S2 reconstruct the X/Y coordinates, and the S1-S2 time difference enables Z-coordinate determination, allowing for 3D reconstruction of the event [27]. DarkSide-20k, set to be constructed at the Gran Sasso National Laboratory

(LNGS) in Italy, will contain 20 tonnes of argon in a low-background acrylic vessel and will use 'underground' argon to mitigate Argon-39 background events [27]. Similarly, XENONnT at LNGS, which operates a xenon-based TPC, adheres to the same detection principles as DarkSide-20k. In 2023, XENONnT and the LZ experiment (another liquid Xenon TPC experiment) published results excluding cross sections above 2.58×10^{-47} cm^2 at $28\,\mathrm{GeV}/c^2$ and 9.2×10^{-48} cm^2 at $36\,\mathrm{GeV}/c^2$, respectively, with 90% confidence [28, 29].

3.2.3 Bubble Chamber Detectors

Bubble chamber detectors operate on the principle of superheated liquids, which are sensitive to energy deposits from particle interactions. When energy is deposited during a nuclear recoil event, it induces a phase transition in the meta-stable superheated liquid at the interaction site, forming a bubble. By controlling the temperature and pressure of the target liquid, the detector can be fine-tuned to a specific energy threshold, making it sensitive to nuclear recoils while remaining insensitive to electron recoils and gamma rays [30].

PICASSO (**P**roject **I**n **CA**nada to **S**earch for **S**upersymmetric **O**bjects) and COUPP (**C**hicagoland **O**bservatory for **U**nderground **P**article **P**hysics) were early adopters of bubble chamber technology for dark matter searches. The merging of the two collaborations formed PICO, a name derived by combining the first two letters of their acronyms. Recent PICO experiments have utilized freon, C_3F_8, as the superheated target liquid, chosen for its sensitivity to spin-dependent WIMP-proton coupling. Upon a nuclear recoil, the target fluid undergoes nucleation observed as a visible and audible bubble. This offers a method for direct detection of dark matter. Concurrently, the SBC (**S**cintillating **B**ubble **C**hamber) collaboration is investigating the use of liquid argon and xenon as a superheated target, enabling detection of scintillation signals alongside optical and acoustic data. Set to operate at SNOLAB, the SBC experiment is proposed to be sensitive to lower mass WIMPs [31].

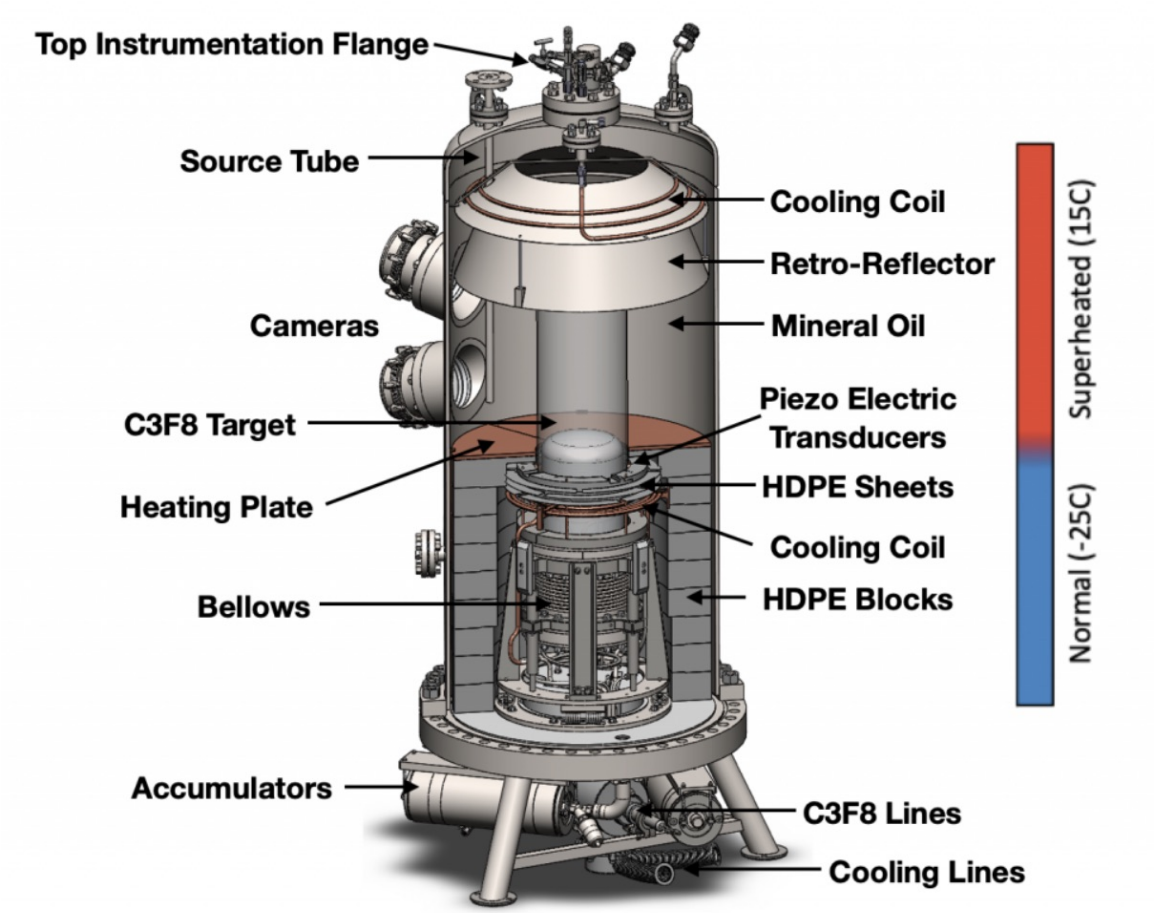

Figure 3.2: CAD model of the PICO-40L dark matter detector, highlighting key components of the pressure vessel and inner vessel including the C_3F_8 superheated target, piezoelectric transducers, cameras, bellows, cooling system, and heating plate which is crucial for maintaining operational temperatures.

PICO-40L

PICO-40L, the current experiment by the PICO collaboration located at SNOLAB, uses approximately 50 kg of C_3F_8 as the target liquid. Improving on the previous detector design of PICO-60, this iteration features a 'right-side-up' geometry, incorporating a secondary inner quartz vessel. This vessel serves a dual purpose: it is used as a piston to regulate the freon pressure and acts as a barrier between the hydraulic liquid and freon, eliminating the need for a water buffer. As depicted in Figure 3.2, the bellows region is kept cold to prevent spurious nucleations at the seals.

This inactive volume also helps in preventing settled particulates from entering the active volume, which is a known source of backgrounds [32]. PICO-40L is equipped with four cameras for optical data collection and multiple piezoelectric transducers for acoustic data collection. Temperature and pressure sensors in the detector are used to monitor the detector conditions and maintain the necessary parameters to keep the detector active. When a nucleation is detected by the camera systems, the high-pressure accumulator is triggered, increasing the pressure in the active volume, which resets the detector to a pure liquid state. Following a brief pause, the pressure is slowly lowered, returning the detector back to a meta-stable superheated state.

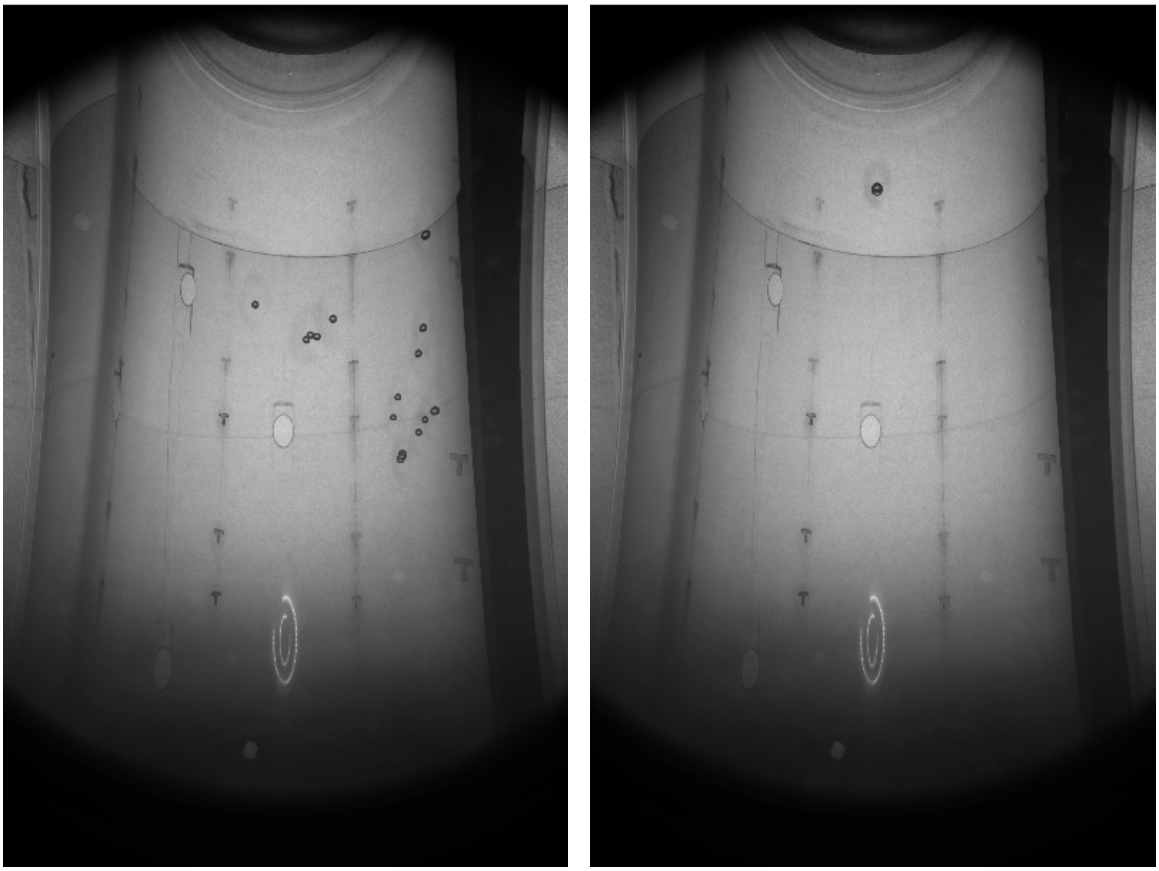

(a) (b)

Figure 3.3: Neutron calibration run in PICO-40L: The left image (a) captures a multi-bubble event. The right image (b) shows a single bubble event, which would be indistinguishable from a dark matter candidate.

In PICO detectors, the number of bubbles in an event and the acoustic parameter are key to identifying the source of nucleation. WIMP interactions are expected to produce single-bubble events due to the rarity of interaction, but these events are not unique to WIMPs; alpha particles can also produce single-bubble events. However, these can be distinguished through acoustic discrimination, as alpha particle recoils produce a louder signal. Neutrons are capable of producing both multi and single bubble events (Figure 3.3). Such single-bubble events from neutrons are indistinguishable from WIMP candidates. Therefore, neutrons can be used to calibrate the detector and to identify detector backgrounds. Before calibration, and during the assembly phase, effective measures are necessary to mitigate contamination that contributes to the detector background. This topic is further discussed in Chapter 6.

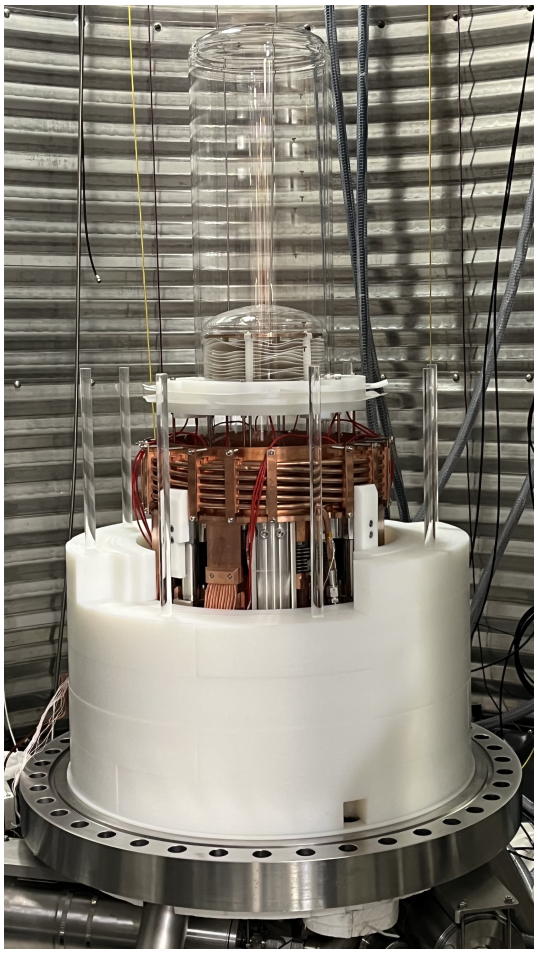

Figure 3.4: PICO-40L assembly during the fall of 2022.

Figure 3.5: Cross-sectional CAD illustration of PICO-500, the next-generation bubble chamber detector compared to PICO-40L.

PICO-500

Building on the experience from PICO-40L, the PICO collaboration is developing PICO-500, a tonne-scale bubble chamber, for operation in the Cube Hall at SNOLAB. While the stainless steel pressure vessel is designed to hold a 1000 L inner detector, the actual inner detector is constrained to a volume of 260 L (420 kg of C_3F_8) due to current quartz forming limitations [33]. PICO-500 will adopt the 'right-side-up' design, featuring two synthetic quartz vessels in the same manner as PICO-40L. A bellows system, using the inner jar as a piston, will regulate the pressure of the

C_3F_8 target. For data acquisition, PICO-500 will be equipped with four cameras and piezoelectric transducers, mirroring the setup of PICO-40L.

The projected spin-dependent WIMP-proton sensitivity of PICO-500, along with other PICO detectors, is illustrated in Figure 3.6. In the parameter space of WIMP-proton interactions, PICO detectors are highly competitive with PICO-500 projected to achieve world leading sensitivities.

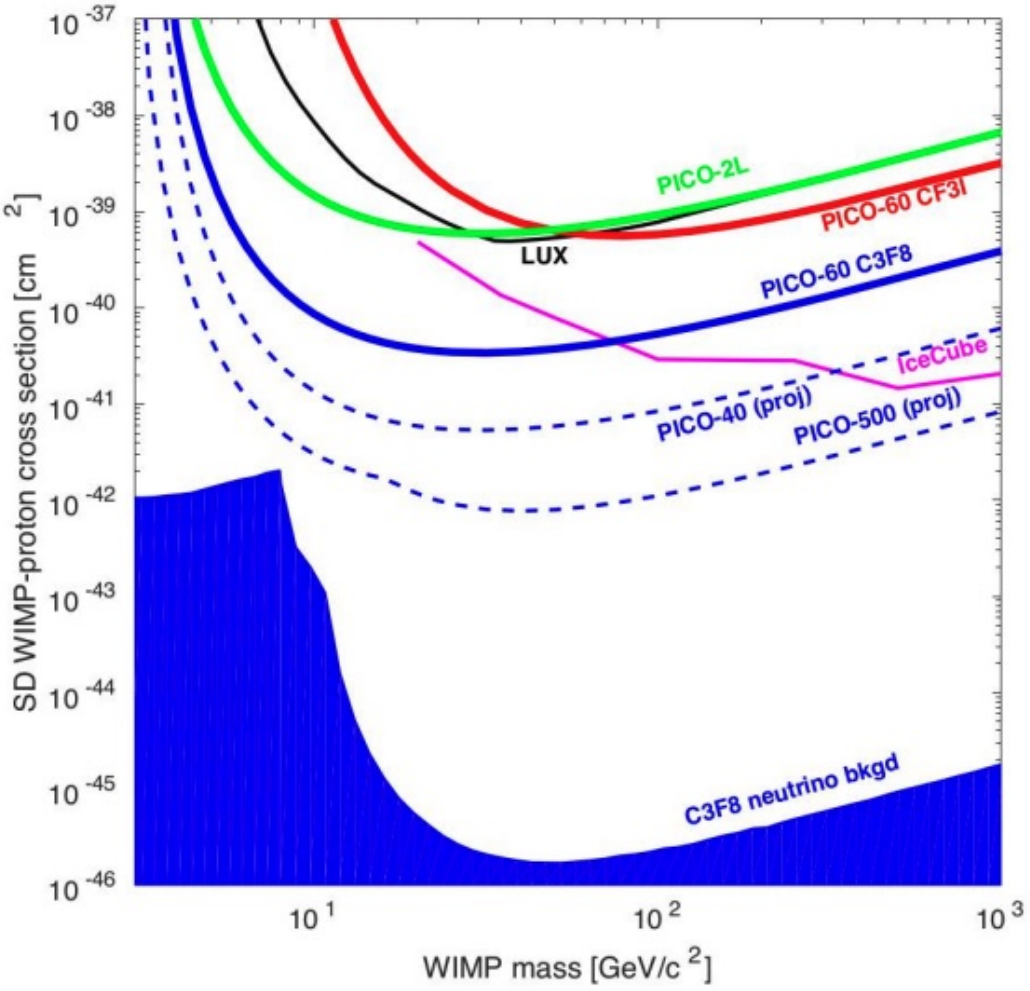

Figure 3.6: Spin-dependent dark matter exclusion plot depicting WIMP-proton cross-section versus WIMP mass, with exclusion curves from various PICO detectors [33]. The regions above the curves represent excluded parameter spaces, with the blue shaded area indicating the C_3F_8 neutrino fog.

Chapter 4

Radioactive Backgrounds

4.1 Radon

Radon is a radioactive element that possesses no stable isotopes and is an intermediate in the uranium and thorium decay chains. The discovery of radon is attributed to the observations of a radioactive gas emanating from radium by Friedrich Ernst Dorn (1900) and Ernest Rutherford (1901) [34]. With an atomic number of 86, radon is the heaviest of the six noble gases. Given that radon has a boiling point of $-61.7°C$ at atmospheric pressures, it is gaseous at room temperature [24]. Of particular interest is Radon-222, the most stable isotope of radon, with a half-life of 3.82 days [6] and the potential to accumulate in the environment. On average, the radon concentration in external environments ranges from $5 - 15$ Bq/m^3 [35] where Bq (Becquerel) is the unit of radioactivity defined as one nuclear disintegration per second. Due to the radioactive characteristics of radon and its inert nature, dedicated detection devices have been devised to aid in the implementation of mitigation strategies [36]. A discussion of a particular detection method using an electric drift field to collect charged radon daughters onto a PIN photodiode can be found in Section 4.2. In general, detecting radon is important because inhalation of radon gas is associated with health implications. Radon accounts for nearly half of all human exposure to radiation and is responsible for an increased likelihood of lung cancer [37], and, consequently, Canadian building codes incorporate radon accumulation prevention techniques [38].

However, the implications of radon extend beyond health concerns. In astroparticle research, the necessity for radio-pure materials in ultra-low background detectors emerges to increase detector sensitivity. Since radon has the potential to emanate from construction materials containing natural traces of uranium and thorium, radon daughters can electrostatically attach to other detector components, and dust particulates. Radon gas can also dissolve into liquids and permeate through barriers. Radon gas permeation can be mitigated by selecting impermeable materials were possible. When radon decays are within a detection volume, the continuation of the decay chain leads to background events. To minimize radon contamination in ultra-low background detector construction and operation, the decay chain of uranium and thorium must be understood.

4.1.1 Decay Chain of Uranium and Thorium

Uranium and thorium are observed to undergo extensive decay chains, ending in stable isotopes of lead, as shown in Figure 4.1. These chains are characterized by a sequence of radioactive decay, with each event resulting in the emission of an alpha, beta, or gamma particle. In the case of alpha decay, a helium nucleus is emitted from the parent nucleus. Such decays are monoenergetic, enabling the identification of alpha decaying isotopes based on measured energies. The ejection of an alpha particle results in the decrease of the atomic number by two due to the loss of two protons.

$$ {}^{A}_{Z}X \rightarrow {}^{A-4}_{Z-2}Y + {}^{4}_{2}\alpha \tag{4.1} $$

Where ${}^{A}_{Z}X$ is the parent nucleus, ${}^{A-4}_{Z-2}Y$ is the daughter nucleus, and ${}^{4}_{2}\alpha$ is the alpha particle (helium nucleus). A and Z denote the mass number (total number of nucleons) and the atomic number (total number of protons), respectively.

On the other hand, beta decay (specifically β^- decay) involves the transformation of a neutron into a proton, emitting an electron (often referred to as a β^- particle)

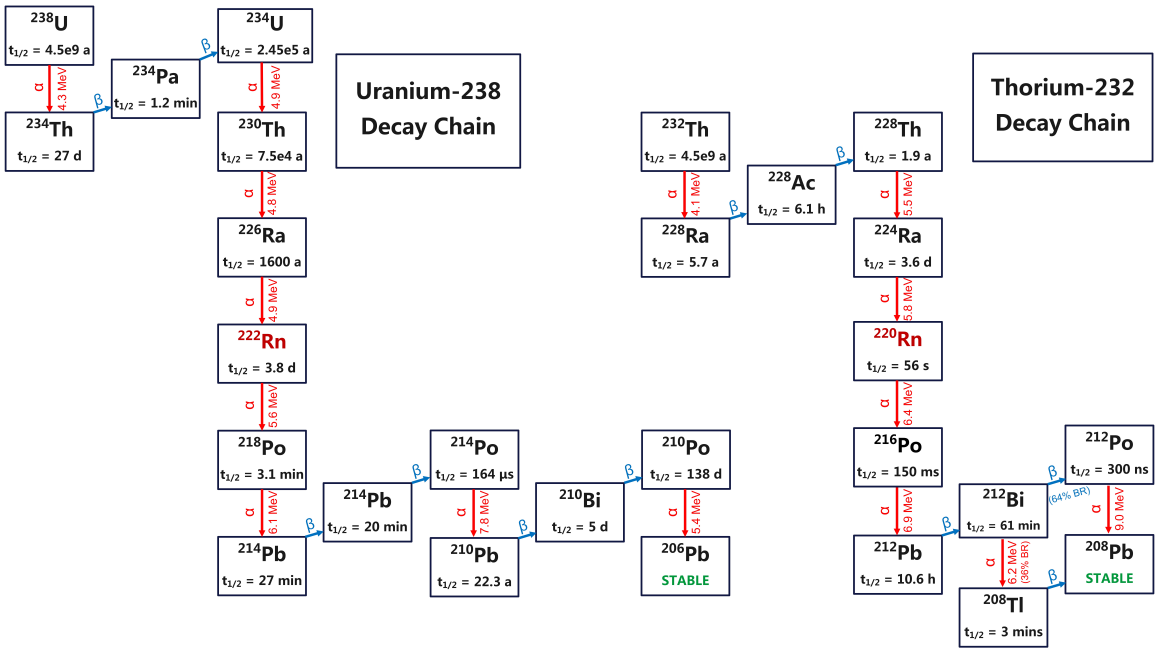

Figure 4.1: The decay series of Uranium-238 and Thorium-232 demonstrating the most probable decay path. Adapted from [39].

and an electron antineutrino in the process. As a consequence, the atomic number of the atom increases by one. The emitted neutrino can take away a varying amount of kinetic energy, resulting in the electron displaying a spectrum of kinetic energies due to the three-body decay involving the neutrino, electron, and nucleus.

$$ {}^{A}_{Z}X \rightarrow {}^{A}_{Z+1}Y + \beta^{-} + \bar{\nu}_{e} \tag{4.2} $$

Where ${}^{A}_{Z+1}Y$ is the daughter nucleus, β^{-} is the emitted electron, and $\bar{\nu}_{e}$ is the emitted electron antineutrino.

Gamma decay is the emission of a highly energetic photon and occurs when an excited nucleus releases excess energy to transition to a lower energy or ground state, without altering its proton or neutron count. This process can follow alpha or beta decay, or result from other excitations, including nuclear reactions.

$$ {}^{A}_{Z}X^{*} \rightarrow {}^{A}_{Z}X + \gamma \tag{4.3} $$

Where ${}^{A}_{Z}X^{*}$ is the nucleus in an excited state, ${}^{A}_{Z}X$ is the same nucleus in a lower

energy or ground state, and γ is the emitted gamma photon.

The thorium decay chain includes the isotope Radon-220, historically referred to as "thoron". Following the alpha decay of Radon-220, isotopes including Polonium-216, Bismuth-212 (alpha decays 35.94% [6]), and Polonium-212 are formed, each undergoing alpha decay with energies observed to range between 6 and 9 MeV [6]. Despite these high-energy emissions, the relatively short half-lives of these isotopes (Bismuth-212 has the longest half-life of 60.55 minutes [6]) result in their rapid decay. Consequently, these short-lived isotopes are not problematic for ultra-low background experiments if there is no source of Radon-220.

Uranium-238 is the most common uranium isotope, with a natural abundance at 99% and a long half-life of 4.5×10^9 years [24]. As a result, the decay chain of Uranium-238 is the most prominent among the decay sequences for naturally occurring uranium. Radium-226 and Radon-222 are among the significant radionuclides (radioactive isotopes) present in this sequence. The presence of uranium and radium in construction materials has been identified as a source of radon contamination. The most probable decay sequence originating from Radon-222 is described below:

$$
\begin{aligned}
&{}^{222}_{86}\mathrm{Rn} \rightarrow {}^{218}_{84}\mathrm{Po} + {}^{4}_{2}\alpha \\
&{}^{218}_{84}\mathrm{Po} \rightarrow {}^{214}_{82}\mathrm{Pb} + {}^{4}_{2}\alpha \\
&{}^{214}_{82}\mathrm{Pb} \rightarrow {}^{214}_{83}\mathrm{Bi} + \beta^- + \bar{\nu}_e \\
&{}^{214}_{83}\mathrm{Bi} \rightarrow {}^{214}_{84}\mathrm{Po} + \beta^- + \bar{\nu}_e \\
&{}^{214}_{84}\mathrm{Po} \rightarrow {}^{210}_{82}\mathrm{Pb} + {}^{4}_{2}\alpha \\
&{}^{210}_{82}\mathrm{Pb} \rightarrow {}^{210}_{83}\mathrm{Bi} + \beta^- + \bar{\nu}_e \\
&{}^{210}_{83}\mathrm{Bi} \rightarrow {}^{210}_{84}\mathrm{Po} + \beta^- + \bar{\nu}_e \\
&{}^{210}_{84}\mathrm{Po} \rightarrow {}^{206}_{82}\mathrm{Pb} + {}^{4}_{2}\alpha
\end{aligned}
\tag{4.4}
$$

Both Polonium-218 and Polonium-214, possessing decay energies of 6.11 MeV and 7.83 MeV [6], respectively, have relatively short half-lives in comparison to Radon-

222. This characteristic enables these isotopes to achieve secular equilibrium in a short duration. In a state of secular equilibrium, the activity of a short-lived daughter nuclide becomes equal to that of its longer-lived parent nuclide. Once Polonium-218 and Polonium-214 reach secular equilibrium with Radon-222, the decays detected serve as an effective method to determine the activity of Radon-222. Following the decay of Polonium-214, Lead-210 and subsequently Polonium-210 are produced. With Lead-210 having a half-life of 22.2 years and Polonium-210 of 138 days [6], the gradual accumulation of Polonium-210 and its alpha decay (5.40 MeV [6]) highlights the need for radon mitigation in ultra-low background experiments.

4.1.2 Importance of Radon and Progeny in Ultra-low Background Detectors

Ultra-low background detectors are precision instruments for experiments requiring minimal background radiation levels to measure rare events. This is not limited to dark matter search experiment detectors; ultra-low backgrounds are also crucial for neutrinoless double beta decay experiments and neutrino detectors where rare low energy neutrino interactions are the primary focus. In these scenarios, Radon-222 emerges as a significant concern due to its ubiquity. Radon-222 contamination, emanating from uranium and radium-bearing materials from the Earth's crust, is a major concern. The emanation process from materials is constant, prompting investigations into radon emanation from samples to determine the suitability in ultra-low background detectors. As shown in Figure 4.1, Radon-222 and several of its progeny (daughters) undergo alpha decay. Within ultra-low background detectors, these alpha decays introduce background signals. Short-lived progenies, including Polonium-218, Lead-214, Bismuth-214, and Polonium-214, can be detected. Among these decay products, isotopes of polonium, particularly the long-lived Polonium-210, are notable for the potential to disrupt sensitive measurements. This is due to the plate-out effect, a phenomenon where radon progeny adhere to surfaces (plate-out), as illustrated

in Figure 4.2. Charged radon progeny can also electrostatically attach to airborne dust particles. Polonium-218 was found to carry a positive electrical charge in 87% of the cases under standard conditions [40]. Consequently, decaying radioactive dust particles can mimic the signature of a WIMP-nuclear recoil event in PICO detectors, producing an indistinguishable acoustic signal [41].

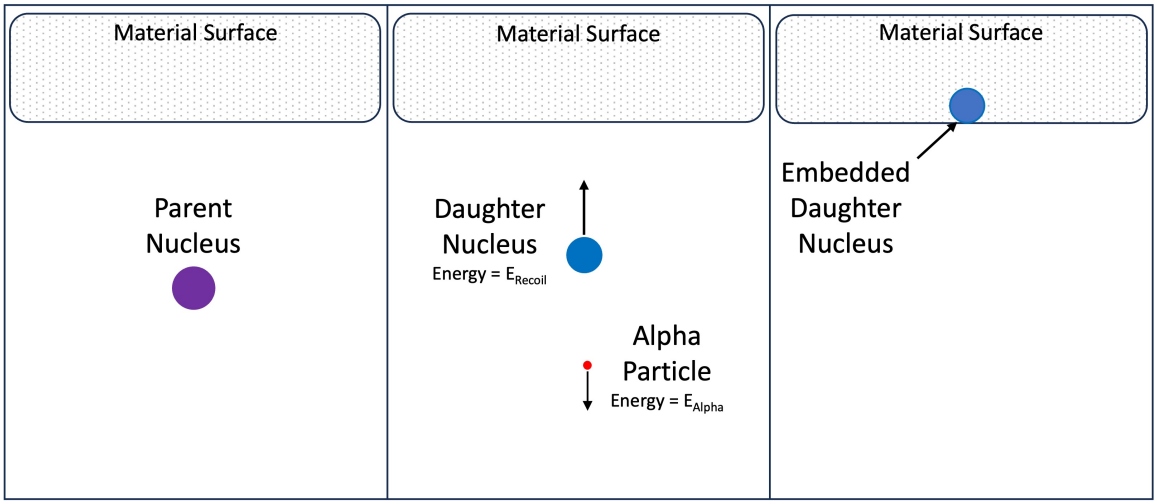

Figure 4.2: A process in which radon progeny can embed into materials. Graphic adapted from [42].

Strategies to mitigate radon in ultra-low background experiments are crucial for the sensitivity of the experiment. These mitigation strategies include the utilization of radon-reduced air or dry nitrogen gas to reduce exposure, the design of detectors using materials characterized by low radon emanation, and the application of both active and passive mitigation approaches. An illustration of mitigation strategies is documented in the design of the NEWS-G (**N**ew **E**xperiments **W**ith **S**pheres – **G**as) detector [43]. This dark matter search experiment utilizes a spherical proportional counter made out of a 135 cm diameter spherical vessel that was constructed by fusing two hemispheres made from 99.99% pure C10100 Oxygen-Free Electronic Copper [43]. To alleviate the background interference posed by Lead-210, a layer of pure copper, 500 µm in thickness, was electroplated onto the inner surfaces of these hemispheres. Notably, the experiment has incorporated radio-pure lead sourced from

ancient Roman artifacts. Over millennia, the radioactivity present in the lead due to isotopes such as lead-210 has decayed away, making it extremely low in background radiation. Within the NEWS-G detector, this Roman lead forms a 3 cm thick inner shell, effectively insulating against background radiation from the Lead-210 decays in the subsequent 22 cm thick modern lead outer shell [43]. This lead shield is designed to insulate the experimental apparatus from gamma radiation. Collectively, radon mitigation strategies like those applied in the NEWS-G detector are imperative for ultra-sensitive detection capabilities. Similarly, the SNO+ experiment and the Radon Clean Room at the University of Alberta (UofA) adopted a strategy of selecting materials with low radon emanation, measured using the UofA radon emanation chamber detector [42].

Nuclide	Half-life	Decay Type	Decay Energy	Parent Nuclide
^{226}Ra	1,600 years	α	4.87 MeV	^{230}Th
^{222}Rn	3.8235 days	α	5.59 MeV	^{226}Ra
^{218}Po	3.10 minutes	α	6.11 MeV	^{222}Rn
^{214}Pb	27.06 minutes	β^-	1.02 MeV	^{218}Po
^{214}Bi	19.9 minutes	β^-	3.26 MeV	^{214}Pb
^{214}Po	163.3 μs	α	7.83 MeV	^{214}Bi
^{210}Pb	22.2 years	β^-	0.0634 MeV	^{214}Po
^{210}Bi	5.012 days	β^-	1.16 MeV	^{210}Pb
^{210}Po	138.376 days	α	5.40 MeV	^{210}Bi
^{206}Pb	Stable	-	-	^{210}Po

Table 4.1: Common decay path of the Radon-222 decay series. Data sourced from the National Nuclear Data Center [6].

4.2 The Radon Emanation Chamber Detector

The UofA high-sensitivity radon emanation detector was first commissioned circa 2012. The emanation chamber detector incorporates a Hamamatsu S3204-09 silicon PIN photodiode [44], which is accessed through a delrin feed-through positioned at the centre of the lid. The diode has an active area of 18 mm by 18 mm [44]. In March 2023, the PIN photodiode was replaced due to the accumulation of Polonium-210 activity on the original diode. The chamber is a stainless steel cylindrical vessel with a diameter of 0.598 m and had a detection volume of 0.171 m^3 [42]. The initial design incorporated a face seal from the lid to the tank body using a butyl O-ring. A leak was detected at the weld joint of the flange to the tank body, which impacted the sensitivity of the detector. To address this issue, the lid was redesigned to radially seal against the inner diameter of the tank body and positioned below the weld joint. This updated lid design is comprised of four main components: an O-ring spacer, the primary lid, an O-ring compression ring, and a top support ring (Figure 4.3). Embedded within the tank lid are all necessary electronics, accessed via a feed-through as before, as well as ports for gas circulation. The purpose of the O-ring spacer is to account for the non-uniform shape of the tank body, ensuring the O-ring adequately contacts both the tank body and lid for effective compression and sealing. The compression ring, when bolted to the tank lid, exerts pressure on the O-ring, forcing it outward to contact the tank body. This design modification led to a decrease in height by 5.5 cm, yielding a detection volume of 0.157 m^3 (an 8.19% reduction with respect to the original tank). Helium leak check tests performed on the emanation chamber did not find any detectable leaks with the new seal design.

A high voltage of $-2.0\,\text{kV}$ is applied to the PIN photodiode, establishing an electric drift field between the grounded vessel and the diode to direct positively charged radon progeny toward it. Two batteries, connected in series, supply the diode with a reverse bias voltage of 12 V. Radon progeny accumulate on the surface of the

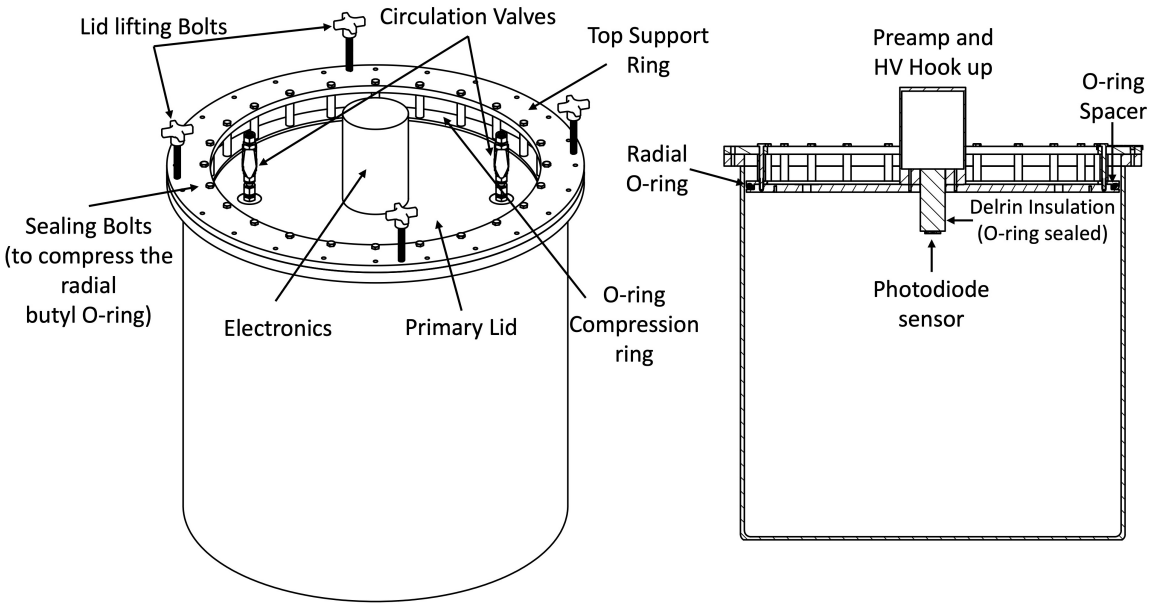

Figure 4.3: A schematic of the re-commissioned radon emanation chamber. The main hardware components are depicted in the left schematic, while a cross-section highlighting electronic components, the O-ring, and the O-ring spacer is shown in the right schematic.

photodiode, enabling the subsequent measurement of alpha decay as the alpha particle traverses the depletion region. The radon daughters Polonium-218 and Polonium-214 are particularly significant. A spectrometric measurement conducted with the emanation chamber reveals an energy spectrum and, given that Polonium-218 and Polonium-214 reach secular equilibrium with Radon-222 in a short duration, the radon activity of any source material can be inferred from these two decay channels.

The data acquisition for the emanation system is managed through LabVIEW, interfacing with a custom 8-channel MCA (multi-channel analyzer) featuring a 0-2 V range, 50 MS/s rate, and 12-bit resolution [42]. Additionally, twelve auxiliary channels record voltage, pressure, and temperature in a range of 0-5 V and 0-10 V at 10 kS/s with 10-bit resolution and are referred to as the Slow-ADC. Data are transferred from the MCA to the computer via USB. A custom C++ library is used to write the data into a `ROOT` file, which is then analyzed in Python using the `Uproot` library.

4.2.1 The Radon Emanation Equation

The emanation of radon gas from the surface of a material containing traces of uranium or radium can be expressed by the following differential equation:

$$\frac{dN_{Rn}}{dt} = -\lambda_{Rn} N_{Rn} + E_{Rn} \quad [42] \tag{4.5}$$

Where N_{Rn} denotes the number of radon atoms, λ_{Rn} is the radon decay constant, and E_{Rn} is the radon emanation rate from a source. The negative sign in front of $\lambda_{Rn} N_{Rn}$ represents a decrease (decay) in radon atoms over time, whereas the emanation rate indicates a continuous source of radon atoms.

Upon integrating both sides of the differential equation with respect to t, the following general solution is obtained:

$$N_{Rn}(t) = \frac{E_{Rn}}{\lambda_{Rn}} + \left(N_{Rn,0} - \frac{E_{Rn}}{\lambda_{Rn}} \right) e^{-\lambda_{Rn} t} \tag{4.6}$$

Where $\frac{E_{Rn}}{\lambda_{Rn}}$ is the equilibrium number of radon atoms in the system and $N_{Rn,0}$ is the number of radon atoms in the system at $t = 0$. As t grows large, the number of atoms approaches equilibrium $\frac{E_{Rn}}{\lambda_{Rn}}$. In the scenario where the initial condition of the system begins with no radon atoms (i.e., $N_{Rn,0} = 0$), the equation becomes:

$$N_{Rn}(t) = \frac{E_{Rn}}{\lambda_{Rn}} \left(1 - e^{-\lambda_{Rn} t} \right) \tag{4.7}$$

A more useful quantity is the activity of radon, and for any given time t it is denoted by:

$$A_{Rn}(t) = \lambda_{Rn} N_{Rn}(t) \tag{4.8}$$

Multiplying λ_{Rn} to both sides of the equation 4.7 then yields the activity of radon in a radon emanation system at any time t:

$$A_{Rn}(t) = E_{Rn} \left(1 - e^{-\lambda_{Rn} t} \right) \tag{4.9}$$

The decay counts of radon progeny detected in the radon emanation chamber can be converted into radon activity, provided the count efficiency factor of the detector is known. Given that equation 4.9 models radon emanation sources, it can be applied both to data from radon emanating samples and to background measurements of the detector.

4.3 Recommissioning the Radon Emanation Chamber Detector

Following the upgrades to the emanation chamber, a reassessment of the detector parameters was performed. The emanation chamber is a component of the emanation system consisting of a vacuum holding tank for sample placement, 3/8" tubing for connecting the two chambers, and a diaphragm pump for gas circulation. A detailed Piping and Instrumentation Diagram (P&ID) of this setup is shown in Figure 4.4. The following subsections detail the methodologies and results of peak modelling, ADC-energy calibration, detector efficiency, and the detector background emanation rate. Additionally, the maximum count rate of the DAQ system was assessed with a pulse generator to investigate observed software limitations.

4.3.1 Radon Spectrum and Peak Modelling

Event data from detector runs, which use analog signals converted into digital data through ADC (Analog-to-Digital Converter) channels, allow for the construction of a radon spectrum. This raw data spectrum is divided into bins corresponding to 4096 ADC channels, reflecting the energy levels of detected events. Figure 4.5 illustrates an uncalibrated energy spectrum obtained from the radon calibration run, exclusively featuring the peaks of Polonium-218 and Polonium-214. These isotopes, in secular equilibrium with Radon-222, are crucial for the accurate analysis of radon emanation rates and permeation rates (Chapter 5). Polonium-210 (not visible in Figure 4.5), appearing at ADC channels below Polonium-218, also emerges from the Radon-222

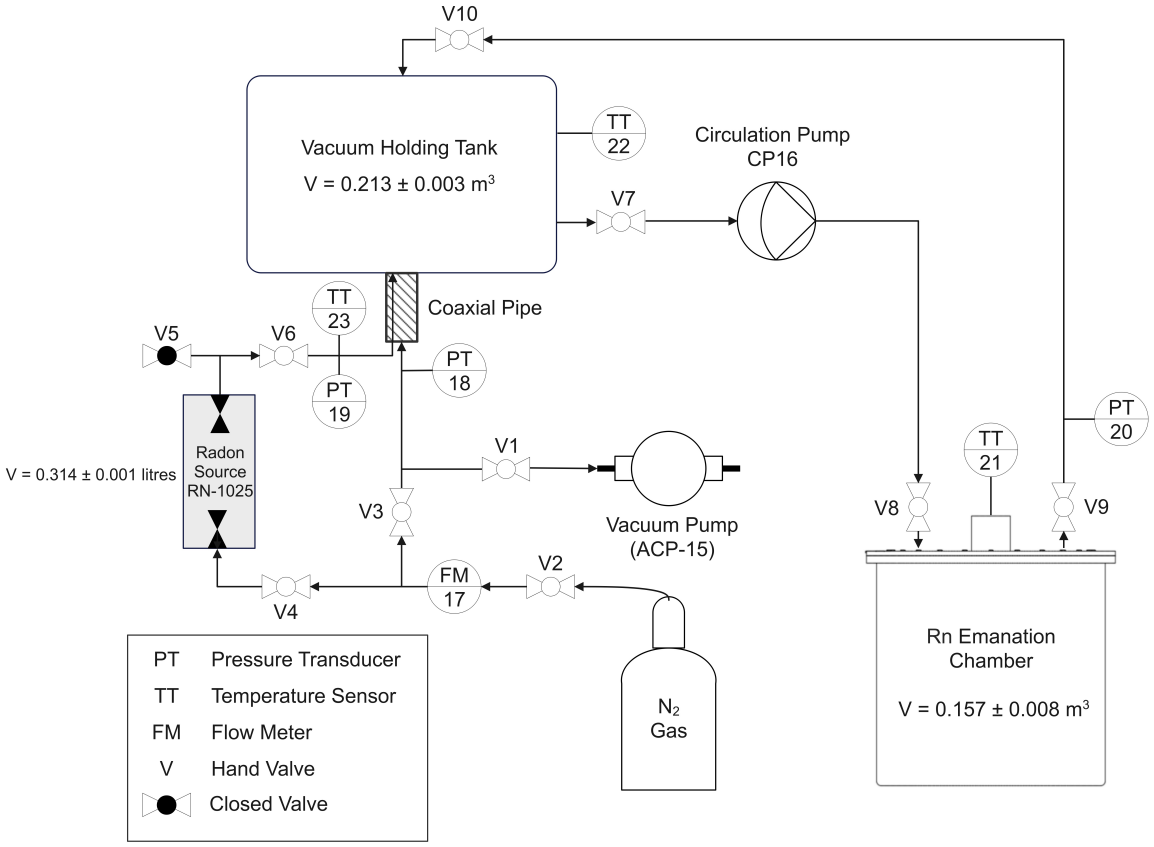

Figure 4.4: Piping and Instrumentation Diagram of the radon emanation system.

decay chain. Its long half-life prevents secular equilibrium with Radon-222, rendering it unsuitable for direct radon activity measurements. However, its presence on the diode surface serves as an indicator of historic radon exposure and provides a useful additional point for the ADC-energy calibration. Since the diode was replaced in March 2023 and has only been minimally exposed to radon, the count rate for long-lived Polonium-210 has been low. In a background run of the emanation system, the corrected count rate in the Polonium-210 Region of Interest (ROI) was calculated to be 109 ± 10 counts/day.

The photodiode used in the emanation chamber detector is a windowless diode designed to detect optical light [44]. To optimize the diode to detect alpha particles, the diode is placed in reverse bias so that all free charges are removed and a full depletion region is formed. This process results in a signal directly proportional to

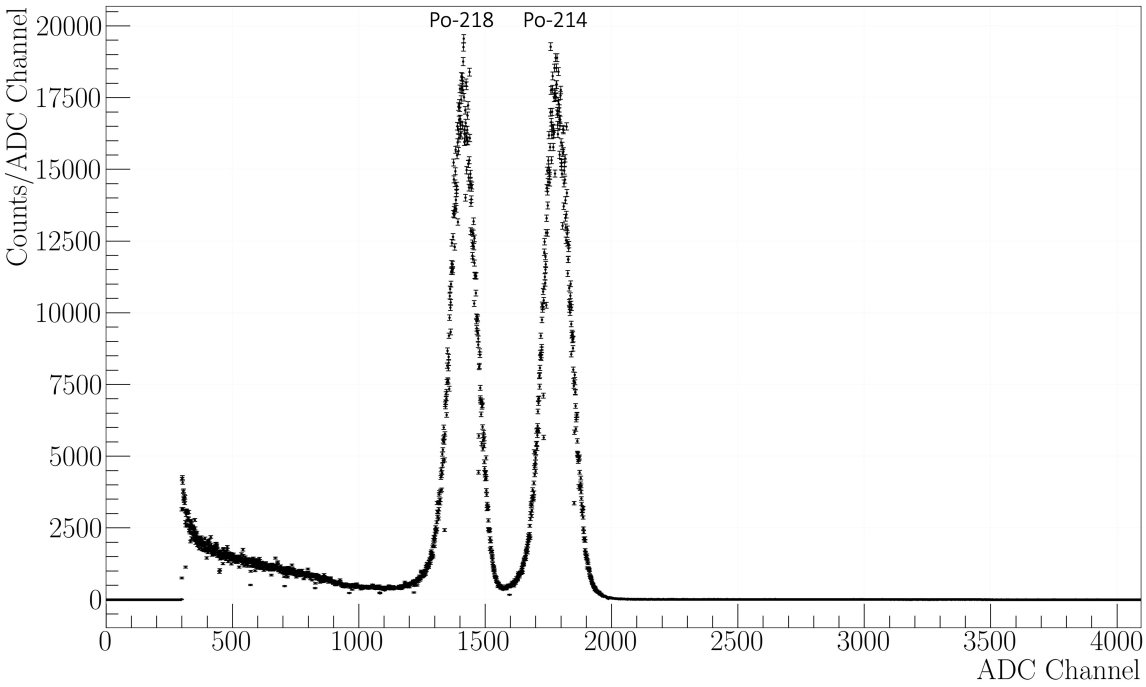

Figure 4.5: Spectra from the radon calibration run 3123-3227.

the kinetic energy of the alpha particle. However, a thin, inactive layer on the surface of the diode, known as the dead layer, attenuates the energy of the alpha particles, a process described by the Landau distribution [45, 46]. This attenuation, influenced by the path length of the particle and angle of incidence, introduces characteristic skewness to the low-energy tail of the alpha peaks, typically modelled by convolving an exponential tail with a Gaussian distribution [47]. Sophisticated peak fitting models have been explored previously for the UofA radon emanation detector [42]. However, due to electronic changes that reduced the energy resolution of the detector by approximately a factor of 5, adopting a simplified peak fitting model using a Gaussian distribution has become necessary.

$$f(x) = A \exp\left(-\frac{(x-\mu)^2}{2\sigma^2}\right) \tag{4.10}$$

where A represents the peak amplitude, μ denotes the peak position, and σ is the standard deviation, characterizing the width of the peak.

This model effectively identifies peak positions and defines the ROIs. An inte-

gration boundary of 2.5 standard deviations is applied to distinguish between the Polonium-218 and Polonium-214 peaks within their respective ROIs without boundary overlap.

A summary of the polonium peak positions and integration bounds can be found in Table 4.2. Figures 4.6, 4.7, and 4.8 show the fitted Polonium-218, Polonium-214, and Polonium-210 peaks, respectively.

Isotope	Peak Position [ADC]	Lower Bound [ADC]	Upper Bound [ADC]
Po-210	1264	1155	1373
Po-218	1413	1282	1542
Po-214	1783	1648	1917

Table 4.2: ADC channel peaks and 2.5 standard deviation ROI limits for polonium isotopes in the radon emanation detector.

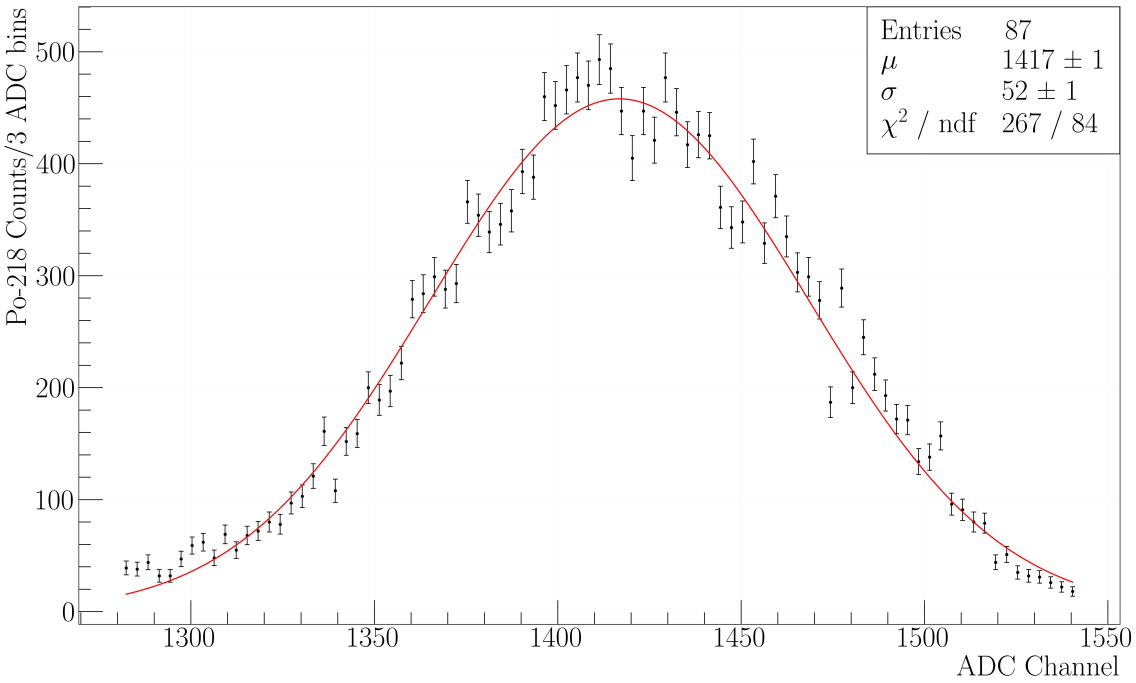

Figure 4.6: Polonium-218 peak in the ROI. Subset of the calibration data.

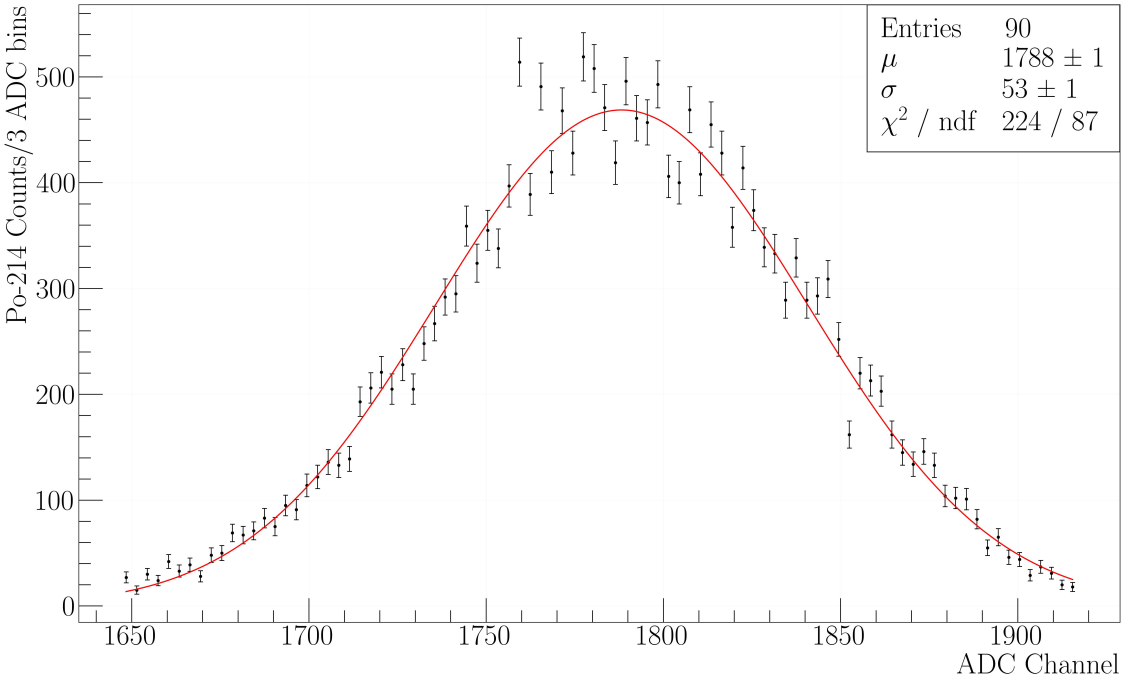

Figure 4.7: Polonium-214 peak in the ROI. Subset of the calibration data.

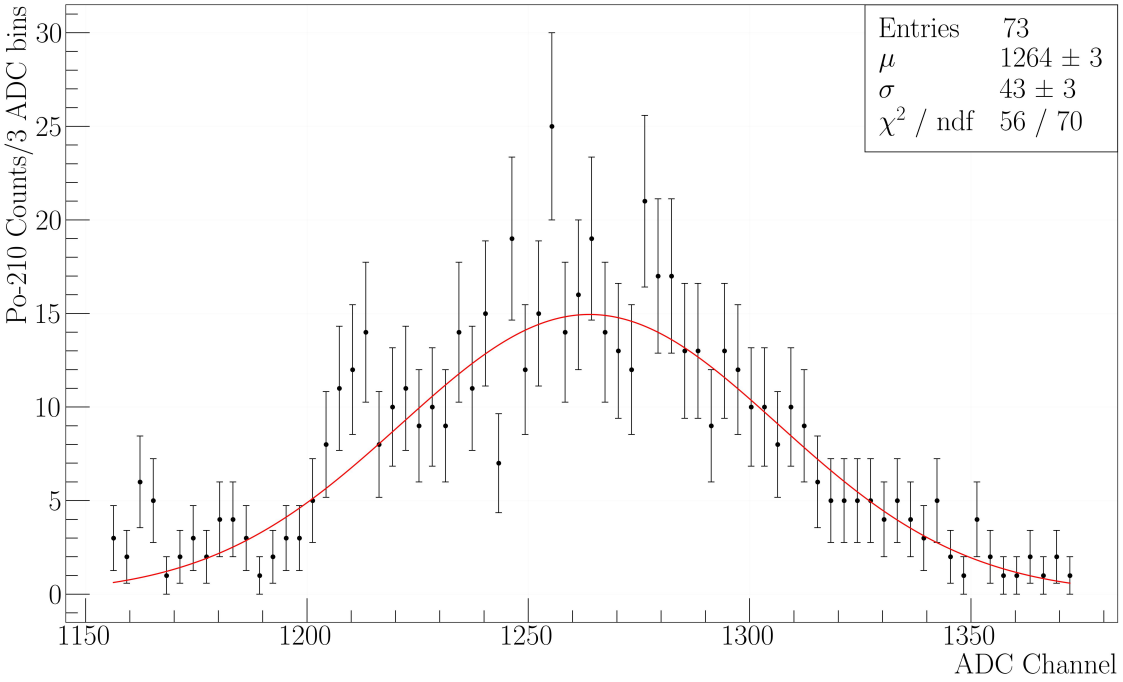

Figure 4.8: Polonium-210 peak in the ROI. From the full emanation system background run.

4.3.2 ADC-Energy Calibration

Since the amount of ionization produced by an alpha particle in the depletion region of the photodiode is directly proportional to its kinetic energy, it is possible to calibrate the ADC channels if the ADC peak and the alpha particle energy are known. A 3-point fit, utilizing the peak positions of Polonium-210, Polonium-218, and Polonium-214, as found in Section 4.3.1, and decay energies sourced from NuDat [6], enables this calibration. The process transforms ADC channels using a linear energy scale (Equation 4.11). This calibration allows for the identification of isotopes based on observed peak energies alone.

$$\text{ADC} = \text{E[MeV]} \cdot \text{Scale} + \text{Offset} \tag{4.11}$$

A table showing the peak positions and integration bounds in units of MeV can be found in Table 4.3. Figure 4.9 shows the ADC-Energy calibration fit, which was used to determine the values in Table 4.3.

Isotope	Peak Position [MeV]	Lower Bound [MeV]	Upper Bound [MeV]
Po-210	5.4	4.9	5.9
Po-218	6.1	5.5	6.7
Po-214	7.8	7.2	8.5

Table 4.3: Polonium peak positions and the 2.5 standard deviation limits expressed in energy [MeV].

4.3.3 Detector Efficiency

To calibrate the emanation chamber detector, a radon source (Pylon RN-1025 [48]) containing Radium-226, with an activity of 0.93 kBq, was used. The volume of the source was measured to be 0.314 ± 0.001 litres. The activity of Radon-222 at any time in the source can be calculated using Equation 4.12. As an example, it takes 26 days for Radon-222 after a full depletion to reach 99% of the Radium-226 activity.

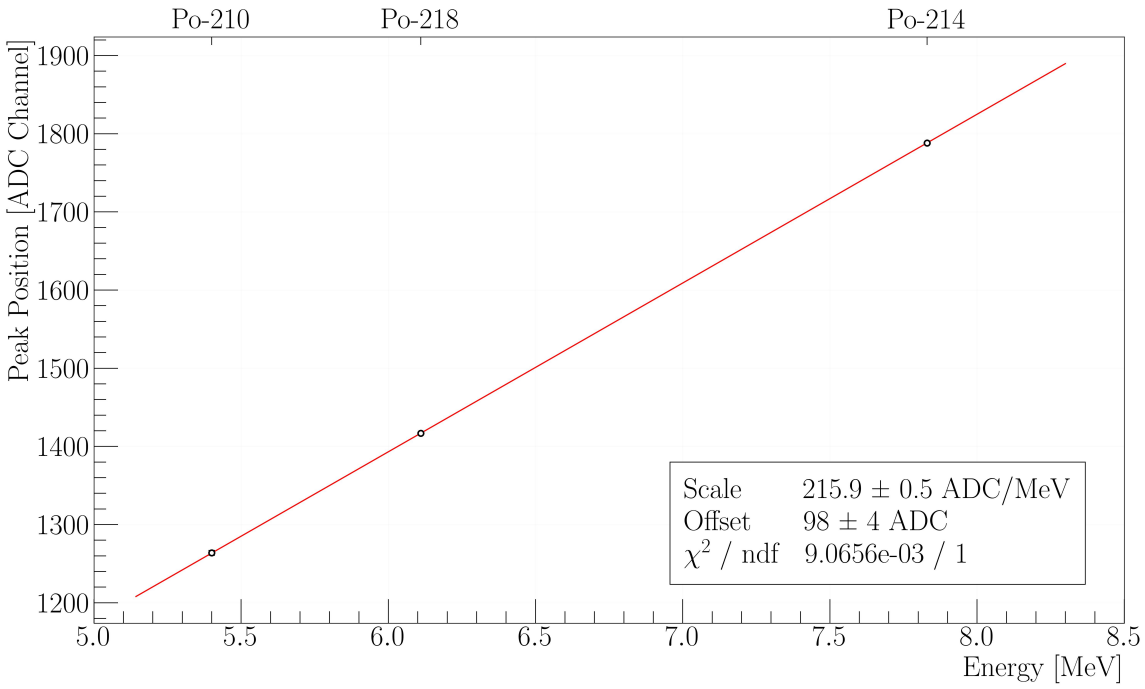

Figure 4.9: Energy calibration using the Polonium-210, Polonium-214 and Polonium-218 peak positions. The Polonium-210 peak position was obtained from the background run 3252-3279 while the Polonium-214 and Polonium-218 peak positions were obtained in the calibration run 3123-3227. Error bars are too small to be discernible at the scale shown.

$$A_{Rn}(t) = A_{Ra}\left(1 - e^{-\lambda_{Rn} t_{elapsed}}\right) \tag{4.12}$$

Where $A_{Rn}(t)$ is the activity of Radon-222 at time t in the source, A_{Ra} is the source activity of Radium-226, λ_{Rn} is the Radon-222 decay constant in minutes ($1.259 \times 10^{-4}\,\mathrm{min}^{-1}$) [42], and $t_{elapsed}$ is the elapsed time since the last purge of the source.

The detection efficiency depends on the geometric design of the emanation system, the characteristics of the electric drift field, the geometry of the diode, and the decay time of the isotope. Determining this efficiency accurately requires empirical methods. It is anticipated that the efficiency in the Polonium-214 and Polonium-218 decay channels grow in over time due to initial radon mixing within the system, progeny accumulation on the diode, and the time required to achieve secular equilibrium, eventually stabilizing at a constant value. Polonium-214 is expected to show a higher

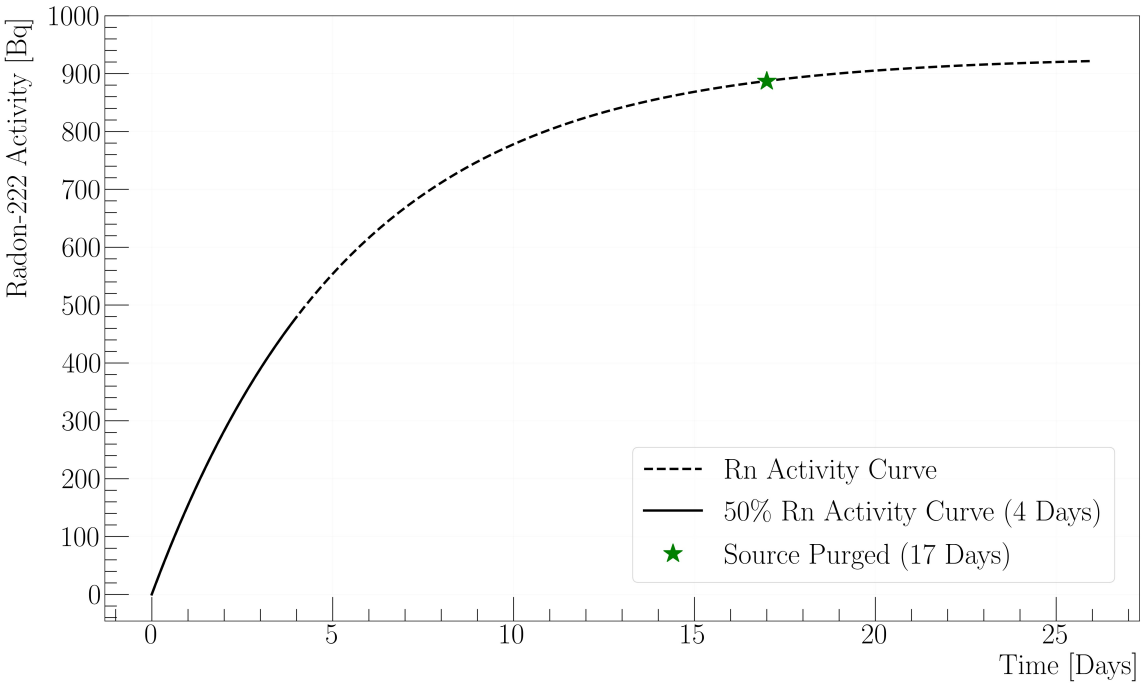

Figure 4.10: Time dependent Radon-222 activity in the Pylon RN-1025 source, highlighting the time taken to reach 50% activity and the moment of purging for calibration (17 Days, 887 Bq). The dashed line represents the theoretical equilibrium curve for radon activity levels above 50%, while the solid line indicates the growth of activity below 50%. The source reaches 50% activity within 4 days after a full depletion of the source.

detection efficiency than Polonium-218, as the longer total decay time from Radon-222 increases the likelihood of electrostatic attraction and detection at the photodiode. Additionally, it has been demonstrated that the efficiency of the system is influenced by the operating pressure due to ion mobility, with the standard operating pressure defined to be 850 mBar. This limitation is primarily due to the operational constraints of the diaphragm circulation pump [42].

The efficiency is also influenced by the electric field strength within the drift field. Previous research has identified a potential difference of 2.0 kV in the emanation chamber as a nearly optimal setting [42]. Therefore, for all measurements presented in this thesis, a standard high voltage setting of -2.0 kV was applied to the diode.

Since it is known how much radon is purged into the emanation system by Equation 4.12, the expected time dependent radon activity can be calculated by Equation 4.13,

which is the radioactive decay law of Radon-222.

$$\mathrm{A(t)} = \mathrm{A_0 e^{-\lambda_{R_n} t}} \tag{4.13}$$

Where A(t) is the activity of Radon-222 at time t, $\mathrm{A_0}$ represents the activity of radon at the time the source was purged, and t is the elapsed time after the source has been purged.

The detection efficiency is determined by comparing the activity detected during the calibration run to the theoretical activity. This comparison involves taking the ratio of the measured activity (in counts per second) to the theoretical radon activity over time.

$$\epsilon(\mathrm{t}) = \frac{\mathrm{A_{Measured}(t)}}{\mathrm{A_{theoretical}(t)}} = \frac{\mathrm{cps(t)}}{\mathrm{A_0} e^{-\lambda_{\mathrm{Rn}} \mathrm{t}}} \tag{4.14}$$

Where $\epsilon(t)$ is the efficiency of the emanation system at time t, $\mathrm{A_{Measured}}(t)$ is the counts per second in the radon progeny decay channel at time t, and $\mathrm{A_{theoretical}}(t)$ is the expected radon activity at time t.

The count rate, (cps), is determined by integrating counts over a given time interval within the energy ranges listed in Table 4.3. The efficiency factor is then used to correct the observed count rates, R, by:

$$\mathrm{R_{Corrected}} = \frac{\mathrm{R_{Measured}}}{\epsilon_{\mathrm{Efficiency}}} \tag{4.15}$$

Run Preparation

Preparation for a calibration run involves evacuating the emanation system to a few hundredths of a mBar and then filling it with nitrogen gas to 850 mBar. This process is repeated three times to ensure the removal of ambient radon. In the final stage, the pressure of the system is increased to 400 mBar before closing valve V3 (Figure 4.4). Before this run preparation, the source was left to recharge for 17 days, resulting in

a radon activity of 887 Bq at the time of purging. Nitrogen gas, at a flow rate of 10 litres per minute (the maximum flow rate of the source [48]), was used to flow through the radon source by opening valves V4 and V6, raising the pressure from 400 mBar to the standard operating pressure of 850 mBar. The complete alpha spectrum from the 8-day calibration run (in energy scale) is shown in Figure 4.11.

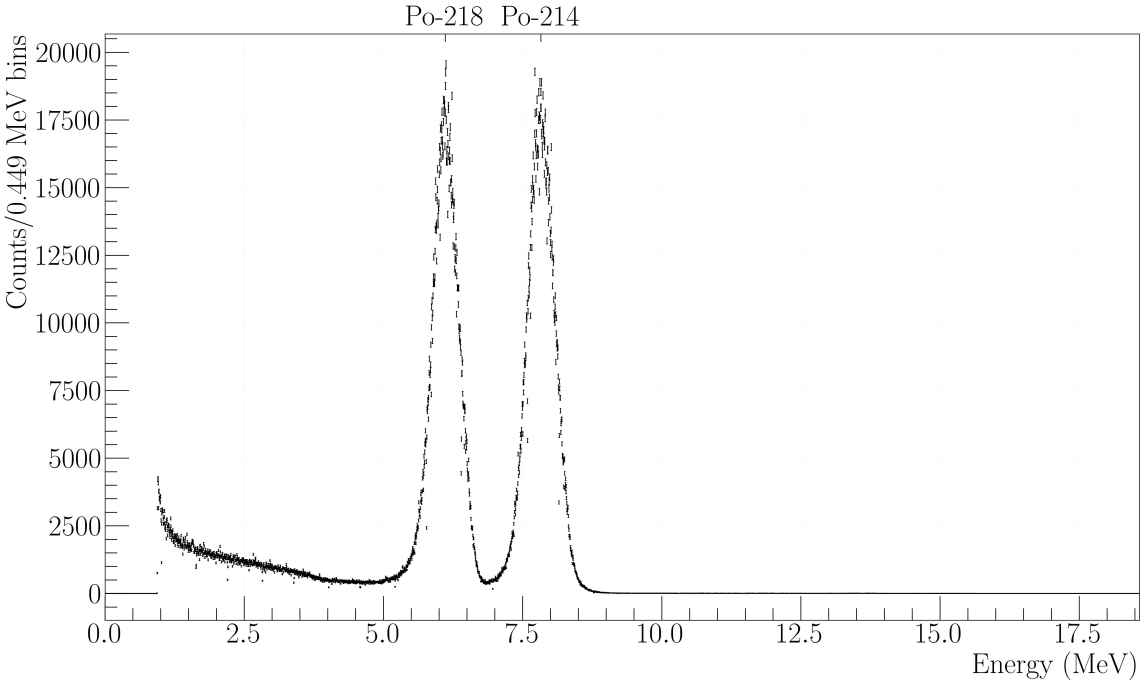

Figure 4.11: Energy-calibrated spectra from the radon calibration run 3123-3227. Radon activity was 426 Bq at the start of data collection, which spanned over 9 days.

Results

At the beginning of the calibration run, persistent LabVIEW crashes affected data collection, prompting both software and hardware inspections of the emanation detector electronics. A break in the high voltage circuit was identified and rectified four days after purging the source into the system and during the first software crash. The data from the first four days of the calibration run were deemed unusable due to the lack of an electric drift field. As a result, the radon activity for the calibration run was extrapolated to be 426 Bq, based on the elapsed time from the purging

of the radon source to the first dataset after repairing the high voltage circuit. Although the efficiencies in the Polonium-214 and Polonium-218 decay channels are anticipated to follow an exponential approach towards a steady state, represented by $\varepsilon(t) = \varepsilon_0 \left(1 - e^{-t/\tau}\right)$, where ε_0 and τ are fitting parameters, the absence of an electric drift field during the initial four days hinders a reliable determination of the time constant τ from this calibration dataset.

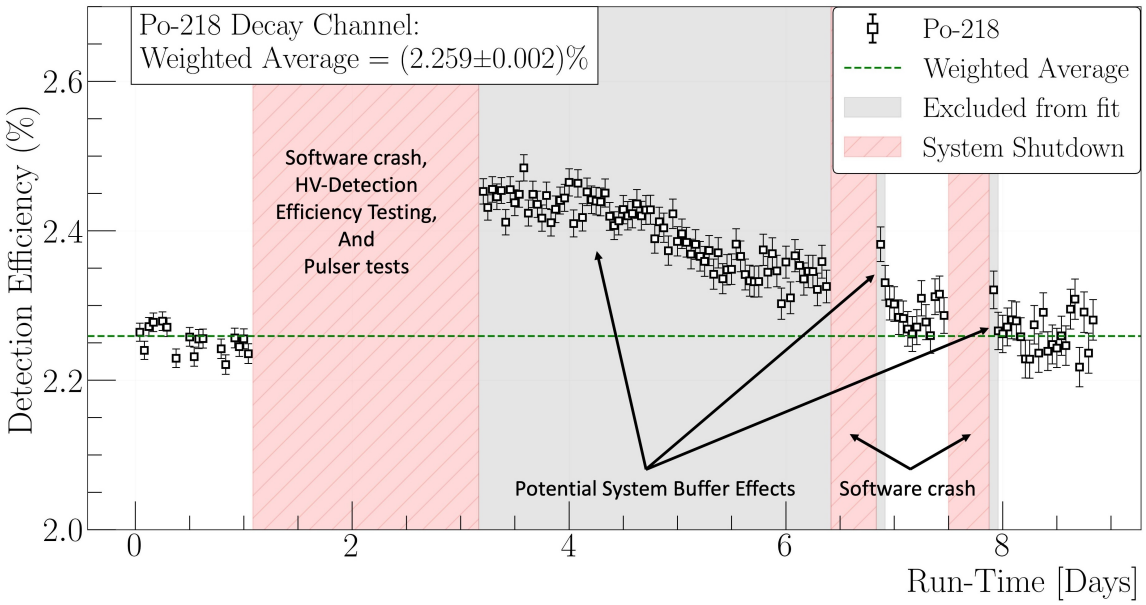

Figure 4.12: Detection efficiency for the Polonium-218 decay channel, over a runtime of approximately 9 days, highlighting regions excluded from the fit and periods of software crashes.

The LabVIEW Radon DAQ program encountered three additional errors suggestive of a memory leak, all of which led to system shutdowns. Figure 4.12 highlights the system downtime and the data regions excluded from the fitting process for ε_0, the steady-state efficiency, determined using a weighted average fit. During the system downtime resulting from the first LabVIEW crash, investigations into the emanation system included assessing the dependency of detection efficiency on applied high voltage and conducting experiments with a pulse generator to identify the count rate threshold causing the crashes, as detailed in Section 4.3.5. These efforts aimed to troubleshoot and understand the underlying issues causing the program to error and

crash. In response to the software issues, and to minimize the risk of significant data loss from further crashes, the data-saving frequency of the LabVIEW program was modified during the second system shutdown. Instead of every 24 hours, data were saved every 6 hours. This adjustment was a crucial mitigation step to continue data collection amidst ongoing software reliability issues.

Software failures disrupted dataset continuity throughout this measurement. It was observed that the act of shutting down and re-initiating data collection, notable at the 3-day mark, revealed an unexpected time-dependent efficiency. Initially, this efficiency was higher than the weighted average but subsequently decreased steadily, a phenomenon that remains not fully understood. It is hypothesized that this observation may be related to the temporary accumulation of counts in the readout system's buffer, leading to an apparent higher efficiency rate before the system returns to a state of equilibrium. Similar patterns of increased initial count rates were observed following restarts after two subsequent LabVIEW crashes. To mitigate the impact of these transient, time-dependent efficiencies on the overall analysis, data collected immediately after the first LabVIEW crash and within two hours of restarts from subsequent crashes were excluded from the weighted average calculation. This approach was taken to ensure the analysis focused on the steady-state efficiency.

Due to time constraints, this measurement could not be re-evaluated, leaving the time constant τ undefined for both decay channels. However, the steady-state efficiency was determined by applying a weighted average fit to the dataset that intermittently ran over a 9-day period. Figure 4.13 presents the consolidated datasets, using vertical lines as separation markers between each dataset, along with the efficiency fits for the Polonium-214 and Polonium-218 decay channels. The variation in the size of the error bars reflects the decreasing count rate over time due to radon decay. The weighted average efficiency values were found to be (2.343±0.003)% for the Polonium-214 decay channel and (2.259±0.002)% for the Polonium-218 decay channel, which, in contrast, is significantly lower than the first commissioning of the radon emana-

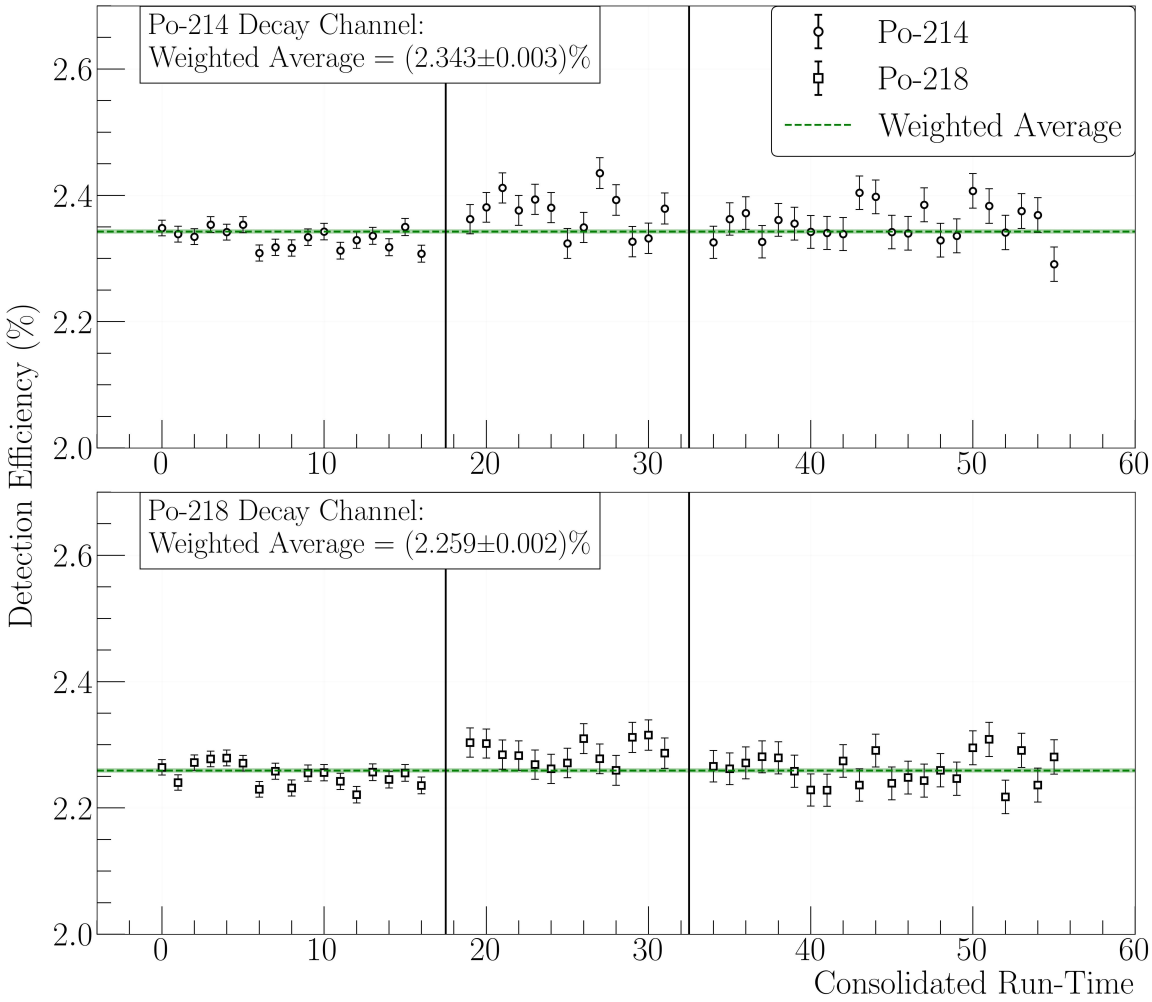

Figure 4.13: Detection efficiency across the Polonium-214 and Polonium-218 decay channels throughout a consolidated run-time. The green line and band represent the steady-state efficiency and 1σ error, respectively, derived using a weighted average fit. The black vertical lines denote separation markers between disconnected datasets.

tion detector using a similar setup with published values of (5.536±0.002)% for the Polonium-214 decay channel and (4.782±0.002)% for the Polonium-218 decay channel [42].

Efficiency Dependence on the High Voltage

With the observance of lower than expected efficiencies, the relationship between detection efficiency and high voltage was examined following the radon calibration run. Utilizing the remaining 82 Bq of radon activity within the emanation system,

extrapolated using Equation 4.13, the detection efficiency of the system was evaluated across a range of high voltages from 0 to -3.5 kV, in -0.5 kV increments, over 4-hour periods due to time limitations. Although a linear relationship was assumed in the fitting of the data presented in Figure 4.14, this may be a consequence of the brief duration of each measurement. Moreover, observations indicated that voltages beyond -2 kV led to broader peak widths and shifted peak positions with negligible efficiency improvement. Consequently, the standard operational voltage of -2.0 kV was maintained for all subsequent runs.

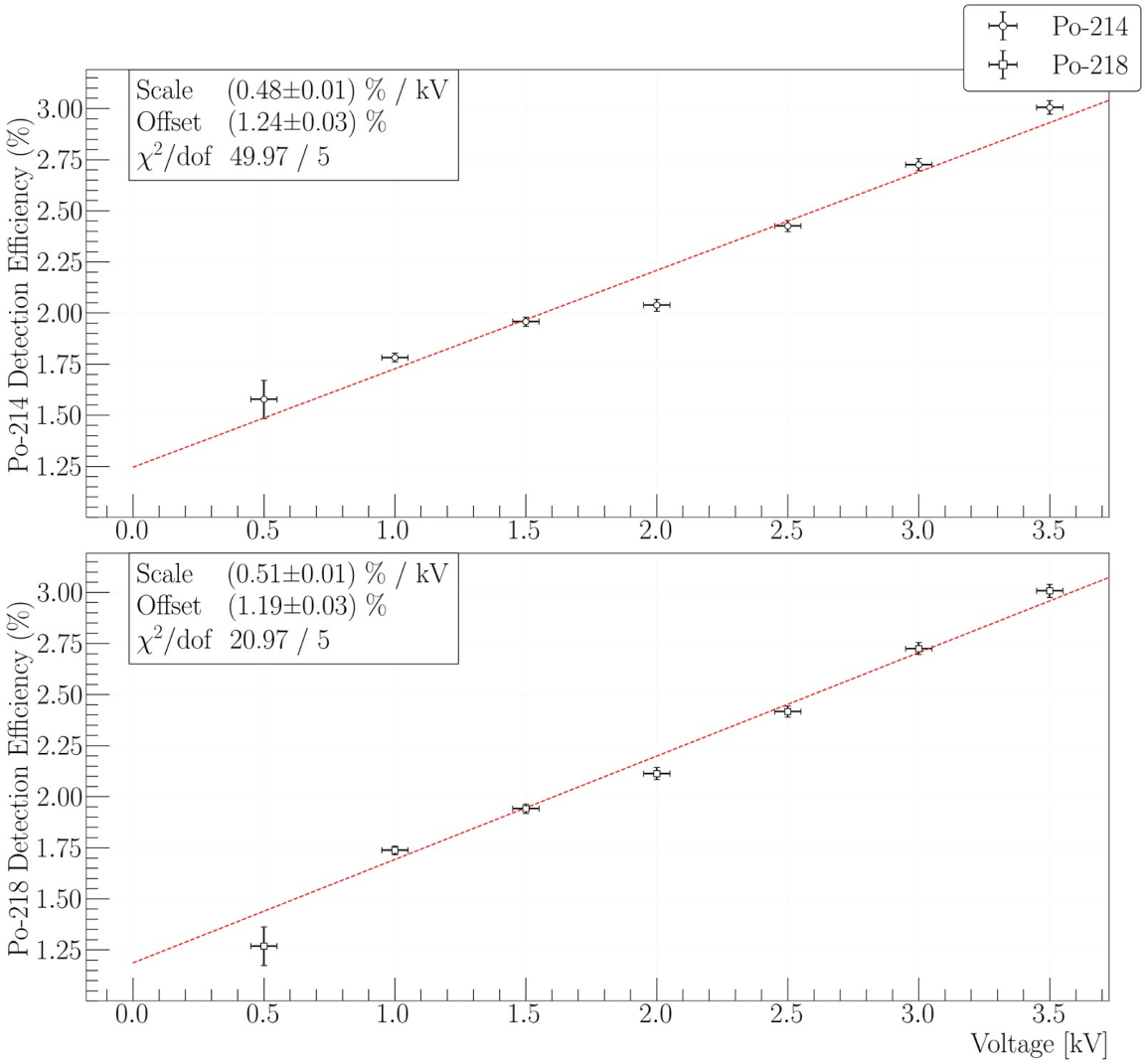

Figure 4.14: Detection efficiency as a function of applied high voltage for Polonium-214 and Polonium-218 decay channels. A linear fit model was applied to the data.

4.3.4 Detector Background

Accurate measurements of radon rates from samples require the quantification and mitigation of ambient radon from the emanation system. Low ambient radon levels require the removal of all dust, particulates, and leaks. To mitigate the dust and particulates, the emanation chamber was cleaned with Alconox, an industrial detergent, and ultra-pure water using the PICO-500 cleaning cart and a Revojet 360° spray nozzle inside the chamber. The vacuum holding tank was thoroughly wiped down with acetone and 70%IPA/30%DI water-saturated polypropylene wipes to manually remove surface contamination. Double gloved procedures were used during the cleaning process and anytime the vacuum holding was accessed. Since the emanation system operates below atmospheric pressure, the system is susceptible to ambient radon entry through potential leaks. A helium leak check identified a small leak at the main door gasket of the vacuum holding tank, which was replaced, eliminating radon ingress as confirmed by subsequent helium leak tests. Moreover, constant average pressure readings over long term radon measurements verified no ambient air leakage into the system. Therefore, any detected radon progeny during the background measurement is attributed to intrinsic sources, including the gas permeation chamber (Chapter 5), which was installed inside the vacuum holding tank for preparation of the permeation tests. The background rate of the emanation system is necessary to correct the radon rate measurements in order to isolate the sample radon rate. This procedure is required for any radon permeation or radon emanation sample:

$$\mathrm{R_{Corrected}} = \mathrm{R_{Sample}} - \mathrm{E_{Background}} \tag{4.16}$$

Figure 4.15 shows the detector background rate for the Polonium-214 and Polonium-218 decay channels, corrected for efficiency and fitted using Equation 4.9, which represents the radon emanation rate.

The detector sensitivity is statistically assessed by setting a detection threshold at

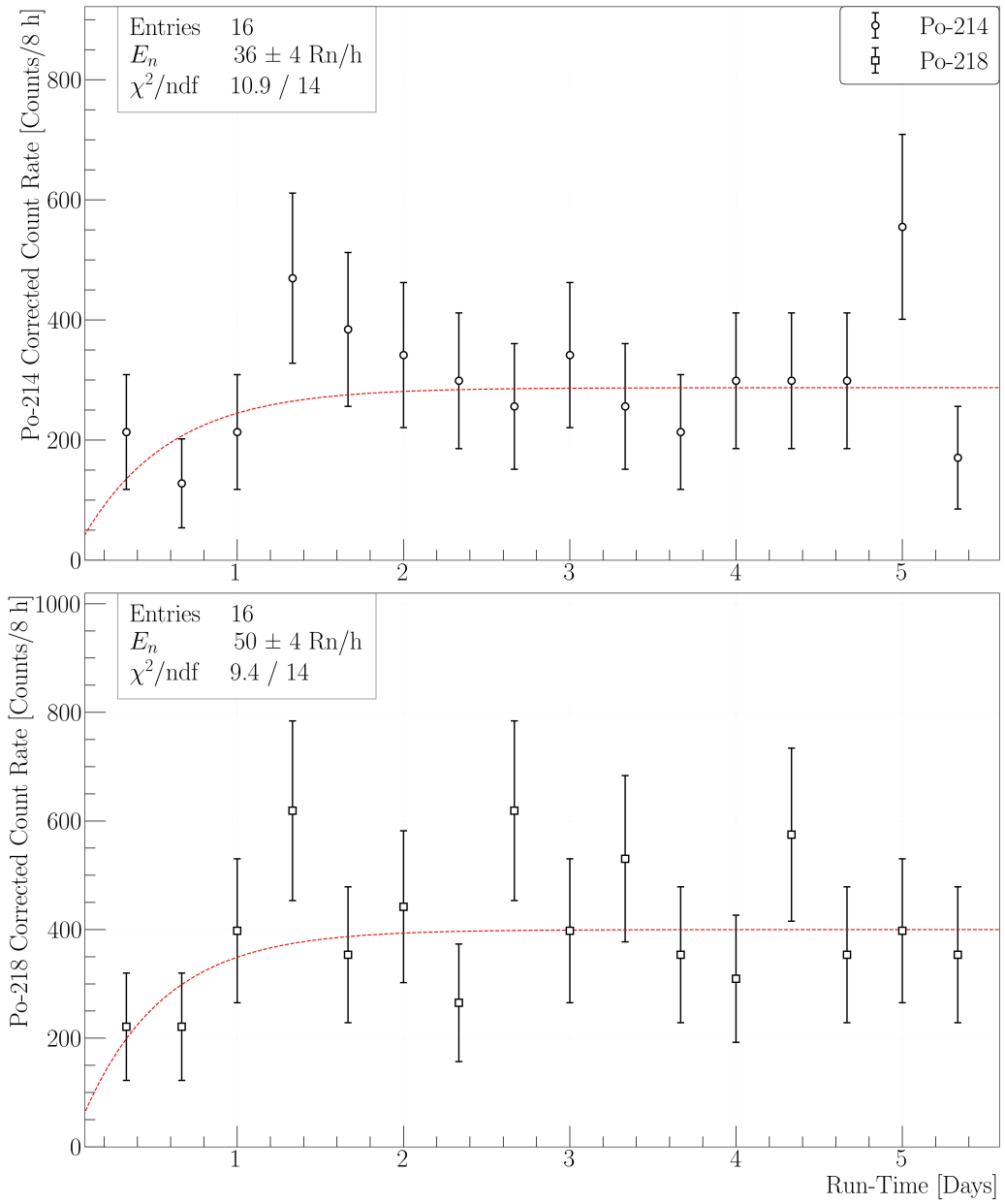

Figure 4.15: Emanation system background in the Polonium-214 and Polonium-218 decay channels.

one standard deviation above the background rate. This approach ensures that any activity exceeding this limit is reliably attributed to the sample and not to background variations. The background radon emanation rate for the system was found to be 37±4 Rn/h within the Polonium-214 ROI and 50±4 Rn/h within the Polonium-218 ROI. Consequently, the sensitivity of the detector is 4±2 Rn/h.

4.3.5 Maximum Count Rate of the Radon DAQ

Software crashes occurred during a radon calibration run with a radon activity of 887 Bq, suggesting that the DAQ system became overloaded at high count rates. This led to an investigation of the maximum count rate capability of the system using a pulse generator.

A pulse generator was connected to the preamplifier to simulate event frequencies from 10 Hz to 5000 Hz. The output frequency, measured by an oscilloscope, was compared to the count rate recorded over 10-minute intervals (Figure 4.16). The system consistently crashed at 130 Hz during data saves. Intermittent crashes starting at 80 Hz prompted a review of the effects of saving Slow-ADC data to a CSV file at a 1 Hz frequency. Each pulse frequency setting underwent two tests: one with Slow-ADC CSV file generation enabled and one with it disabled. A notable deviation from the expected count rate occurred at 70 Hz when Slow-ADC CSV file generation was enabled.

The tests determined that the maximum count rate of the detector capacity was approximately 167 Hz with the Slow-ADC disabled and 147 Hz with it enabled. This was found by manually adjusting the pulse generator until the system crashed. The count rate before saturation onset was identified as 140 Hz without the Slow-ADC and 120 Hz with it, beyond which the system began to saturate gradually. These results highlight limitations in the data acquisition and system processing capacity.

The exact cause of the DAQ crashes remains unclear. Previous full-source calibration runs were completed without data loss or corruption issues. However, intermittent DAQ crashes were observed at event rates as low as 15 Hz and again during a radon background run well below 1 Hz, which crashed after 5 days. The intermittent DAQ crashes and LabVIEW error messages suggest a potential memory leak. To mitigate data loss and file corruption risks, the LabVIEW program data-saving interval was adjusted to 6 hours from the previous 24-hour period, and the system

was manually restarted every 4 days.

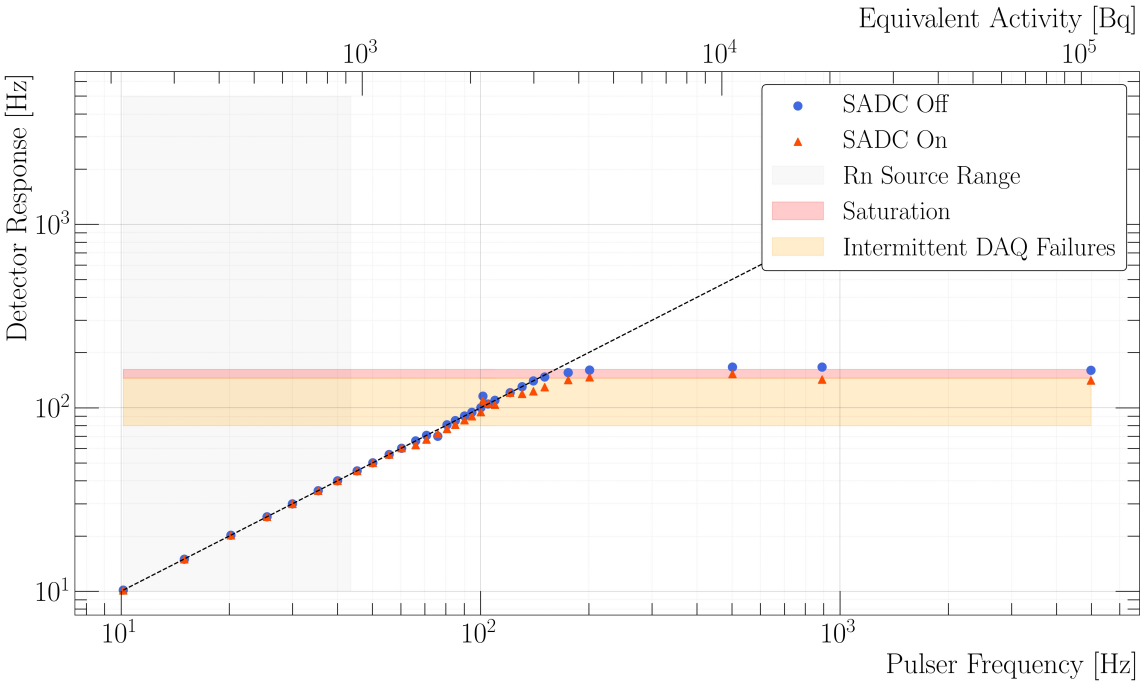

Figure 4.16: Detector response to controlled pulse inputs for both Slow-ADC file generation on and off.

Chapter 5

Radon Permeability of the PICO-500 Inner Vessel Seal

This chapter focuses on quantifying the permeability of radon through the Parker PTFE spring-energized seal, which is an important parameter that will influence the background rate in the PICO-500 detector. Section 5.1 introduces the foundations of gas permeation theory. Section 5.2 provides an experimental setup overview and geometrical analysis of a compressed Parker PTFE seal using numerical methods based on the CAD model. The chapter is then divided into two main sections, each detailing a different method of measuring permeation. In Section 5.3, lower mass noble gases are used as proxies to extrapolate the permeation coefficient of radon. This section applies a linear model correlating the logarithm of the permeation coefficients K_p with the square of the atomic diameters ($\log(K_p) \propto d^2$). Section 5.4 describes a direct method for determining the permeation rate of radon, utilizing the radon emanation chamber detailed in Section 4.2. The permeation coefficient is then calculated from the the permeation rate and experimentally determined parameters. The chapter concludes with Section 5.5, which compares and summarizes the results obtained from both methods, and Section 5.6, estimating the radon activity in the detection volume for the PICO-500 dark matter search experiment.

5.1 Gas Permeation Theory

Thomas Graham, a 19th-century Scottish physical chemist, is widely recognized as a pioneer in the fields of gas mobility and diffusion [49]. His early publications included observations of volume loss in a CO_2-inflated wet pig bladder [50], which, along with

subsequent studies, resulted in the formulation of Graham's Law of Effusion. This law, which compares gas effusion rates through a pinhole based on their molar mass, became instrumental in the early 20th century for developing methods of isotopic separation, a process crucial to the construction of the atomic bomb [51].

Thomas Graham's research laid the groundwork for studies in gas diffusion and gas permeation both through porous and non-porous materials. Graham, in 1866, observed gases were capable of permeating through non-porous rubber films and noted that this phenomenon was a two-stage process in which the gas dissolves into the material and diffuses across it [52]. The mechanism of gas permeation is commonly accepted by the solution-diffusion model. This model integrates aspects of Fick's laws of mass diffusion, which are analogous to Fourier's Law of Heat Conduction, and sorption models like Henry's Law [53].

In the solution-diffusion model, gas molecules first dissolve into a membrane barrier material on the higher pressure side. The molecules then undergo a 'random walk' diffusion through the membrane, driven by a concentration gradient, before finally desorbing on the low-pressure side. This phenomenon is illustrated in Figure 5.1. While permeation refers to the overall process, diffusion specifically describes the mass transport within the membrane. In cases where there is no chemical interaction between the gas and the membrane, diffusion typically becomes the rate-limiting step [53]. As per Fick's First Law, at a steady state, the gas flux within the membrane is directly proportional to the concentration gradient [49].

$$J = -D\frac{dC}{dx} \tag{5.1}$$

Where J is the flux of gas through the membrane, D is the diffusion coefficient, and $\frac{dC}{dx}$ denotes the concentration gradient with respect to position, x, within the membrane. The negative sign indicates that flux proceeds from regions of higher to lower concentration. The diffusion coefficient is specific to the interaction between the gas and the membrane material.

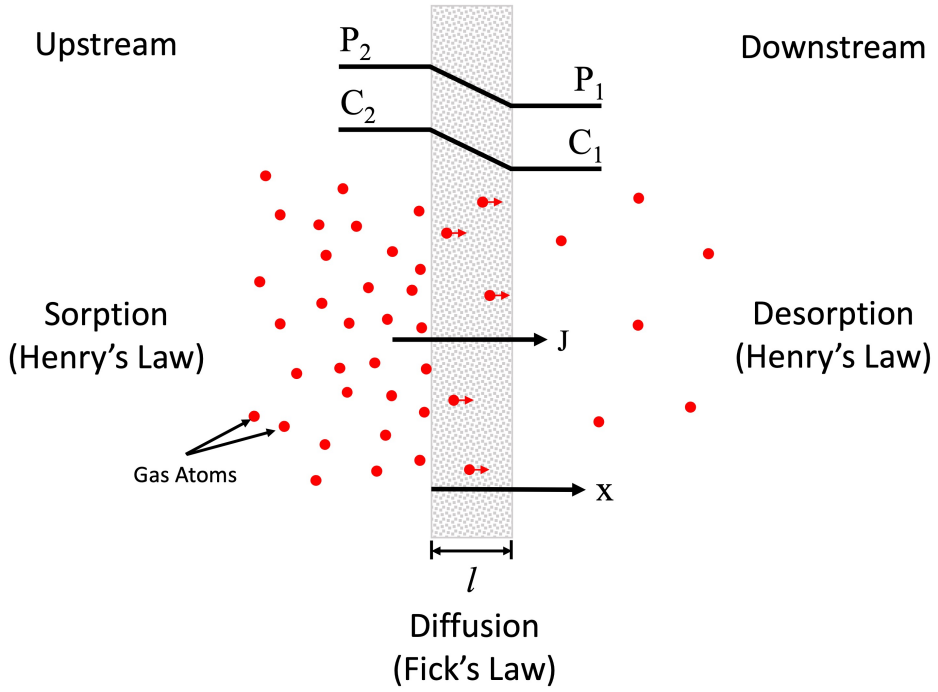

Figure 5.1: A diagram illustrating the solution-diffusion model of gas permeation: red dots represent gas atoms diffusing through a non-porous membrane from a region of higher pressure to lower pressure.

Fick's Second Law is applicable for non-steady-state diffusion processes. The second law provides a detailed description of how the concentration of a diffusing substance evolves over time [49].

$$\frac{\partial C}{\partial t} = D\frac{\partial^2 C}{\partial x^2} \tag{5.2}$$

Where $\frac{\partial C}{\partial t}$ denotes the rate of change of concentration C with respect to time t, and the second order spatial derivative $\frac{\partial^2 C}{\partial x^2}$ represents the curvature of the concentration profile within the membrane.

The permeation rate through a membrane can be determined when the system reaches a steady-state regime, requiring constant surface concentrations. This state can be achieved by exposing the membrane to a permeant gas under constant or sustained high differential pressure. Under steady-state conditions, the concentrations

of the permeant at all points on each side of the membrane remain constant. This approach effectively determines permeation rates, provided that the diffusion coefficient of the permeant within the membrane system remains constant throughout the experiment.

Assuming a diffusion coefficient independent of concentration and a system in the steady-state limit, Fick's Second Law simplifies to:

$$\frac{d^2C}{dx^2} = 0 \tag{5.3}$$

Integrating Equation 5.3 twice, and applying concentration boundary conditions at $x = 0$ and $x = l$, a linear equation of the concentration profile as a function of x is derived.

$$C(x) = C_1 + \frac{x}{l}(C_2 - C_1) \tag{5.4}$$

Substituting this profile into Fick's First Law yields:

$$J = -D\frac{dC}{dx} = \frac{D(C_1 - C_2)}{l} \tag{5.5}$$

Henry's Law states that the concentration of a gas dissolved in a liquid is directly proportional to the gas pressure above the liquid at a constant temperature. This principle also applies to gas-polymer systems, explaining the sorption and desorption mechanism within the solution-diffusion model [53]. The mathematical expression of Henry's Law is:

$$\Delta C = K_s \cdot \Delta P \tag{5.6}$$

In the context of gas solution into a polymer membrane, ΔC is the concentration gradient within in the membrane, K_s is the Henry's Law constant (or solubility coefficient) specific to the gas-polymer membrane system, and ΔP is the differential pressure of the gas across the membrane, as illustrated in Figure 5.1.

It has also been shown that at equilibrium and constant temperature, the product of the diffusion coefficient and solubility coefficient are equal to the permeation coefficient [53].

$$K_p = K_s \cdot D \tag{5.7}$$

In literature, P and S typically represent the permeation and solubility coefficients, respectively. However, to avoid confusion with pressure and surface area, K_p for the permeation coefficient and K_s for the solubility coefficient will be used instead.

The flux through the membrane can be written in terms of the permeation coefficient. Substituting Equations 5.6 and 5.7 into Equation 5.5 yields:

$$J = D \cdot K_s \cdot \left(\frac{\Delta P}{l}\right) = K_p \left(\frac{\Delta P}{l}\right) \tag{5.8}$$

Rearranging Equation 5.8 to solve for K_p and in terms of the volumetric flow rate of the permeating gas:

$$K_p = \frac{Jl}{\Delta P} = \frac{Ql}{S\Delta P} \tag{5.9}$$

Where Q is the volumetric flow rate through the membrane barrier, l is the thickness of the barrier, S is the active surface area for permeation, and ΔP is the differential pressure across the barrier. The standard unit of the permeation coefficient is $\mathrm{K_p} = [1\,\mathrm{Barrer}] = 10^{-10}\left[\frac{\mathrm{cm^3(STP)\,cm}}{\mathrm{s\,cm^2\,cm\text{-}Hg}}\right]$. Figure 5.2 shows the permeation coefficients for various permeants through a TFE/BDD87 membrane over a range of differential pressures [54].[1]

The permeation coefficient standardizes permeation rates (Q) by considering factors such as membrane thickness, active surface area and pressure differential. This standardization facilitates the comparison of permeability across different materials

[1]Reprinted with permission from T.C. Merkel et al, "Gas Sorption, Diffusion, and Permeation in Poly(2,2-bis(trifluoromethyl)-4,5-difluoro-1,3-dioxole-co-tetrafluoroethylene)", Macromolecules 32, 8435 (1999), Copyright (1999) American Chemical Society.

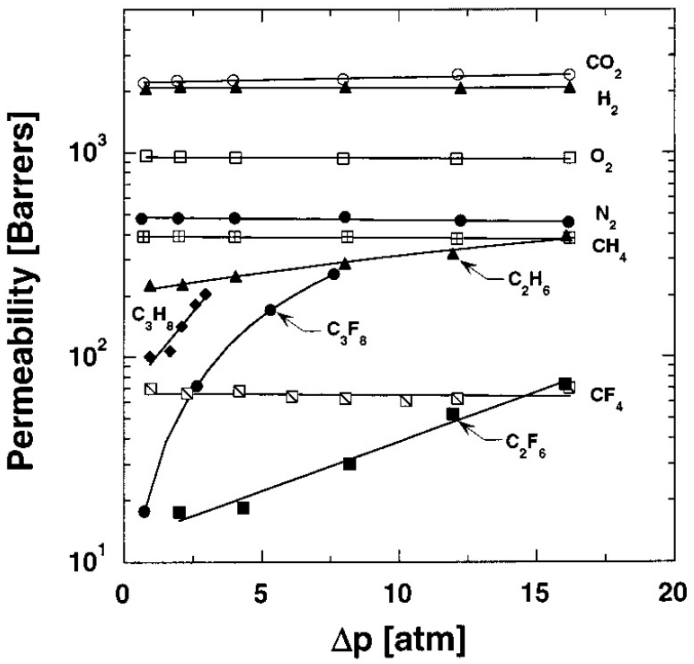

Figure 5.2: Permeability coefficients in TFE/BDD87 at 35°C as a function of differential pressure [54].

or permeants under varied conditions. Larger permeation coefficients relates to higher permeability. As with the diffusion coefficient, the permeation coefficient (and solubility coefficient) is specific to the interaction between the gas and the membrane material.

In gas-polymer systems, the permeation coefficient is derived from both a kinetic factor (K_s) and a thermodynamic factor (D). This leads to a temperature dependence of the permeation coefficient described by the Arrhenius equation [49]:

$$K_p(T) = K_p^0 \exp\left(-\frac{E_\mathrm{p}}{RT}\right) \tag{5.10}$$

Where K_p^0 is a pre-exponential constant, E_p is the activation energy for permeation, R is the universal gas constant, and T is the absolute temperature. Figure 5.3 shows the application of the Arrhenius equation to the permeation coefficients of various noble gases over a range of temperatures, as detailed in [55].[2]

[2]Reprinted from "Permeability of noble gases through Kapton, butyl, nylon, and 'Silver Shield'", S.J. Schowalter, C.B. Connolly, and J.M. Doyle, 267-271, Copyright (2010), with permission from Elsevier

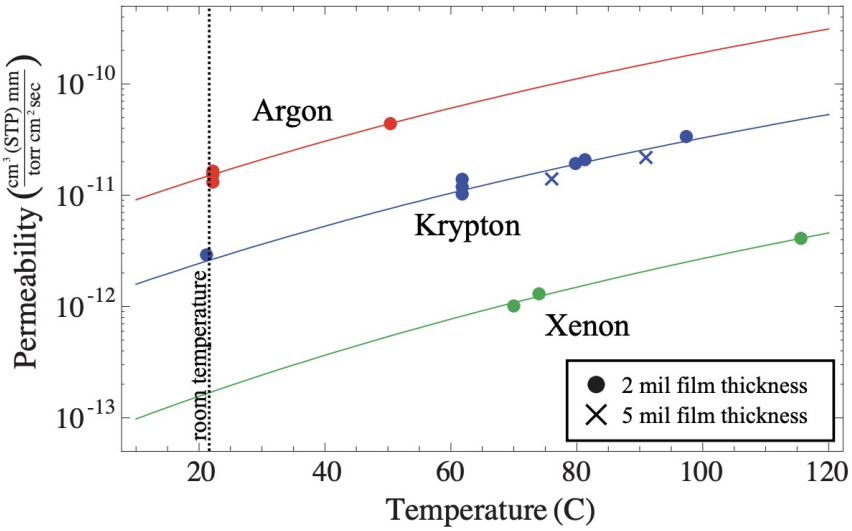

Figure 5.3: Temperature dependence of the permeation coefficients for Argon, Krypton, and Xenon through Kapton films of 2 mm and 5 mm thicknesses [55].

5.2 Experimental Setup

The experiment utilizes the radon emanation system described in Chapter 4, with slight modifications. A 3/8" coaxial line is fed through the primary 1" KF-25 vacuum connection of the vacuum holding tank, connecting to a custom-designed Gas Permeation Chamber (GPC) shown in Figure 5.4. This line features an Omega PX119-030AI pressure transducer [56] for internal GPC pressure monitoring and a ball valve for system isolation post-filling. An INFICON PCG550 pressure sensor [57] is used to obtain pressure readings of the vacuum holding tank. Two IST TSic 501F temperature sensors [58] are installed for gas temperature monitoring: one near the pressure transducer on the fill line, and one on the outside of the aluminum body of the GPC. Additionally, two more IST TSic 501F temperature sensors are placed on the exterior of the vacuum holding tank to further track ambient temperature changes.

For sealing reliability, Swagelok tube compression and VCR fittings are used throughout the fill line, with the exception of the 4-20 mA Omega pressure transducer, which features a 1/4" NPT connection. Epoxy was used to ensure a leak-tight seal at this

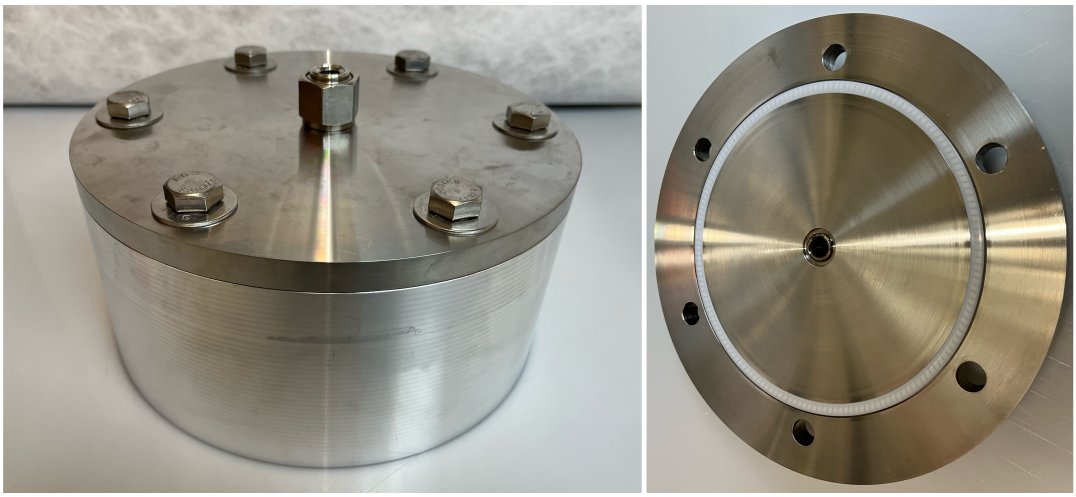

Figure 5.4: Left: The Gas Permeation Chamber fully assembled. Right: The PTFE spring-energized seal, cleaned and installed in the flange.

connection. The system underwent extensive helium leak testing, both with and without the GPC installed, using a VCR cap on the fill line. The GPC assembly (comprising of the chamber, PTFE seal, and stainless steel flange) was independently leak-tested prior to system integration. Post-installation, the system was rechecked for leaks using a helium leak detector, which is necessary to distinguish between leak rates and permeation rates. No leaks were detected within the range of the helium leak detector. Figure 5.5 shows the experimental setup for measuring permeating gases through the Parker PTFE seal.

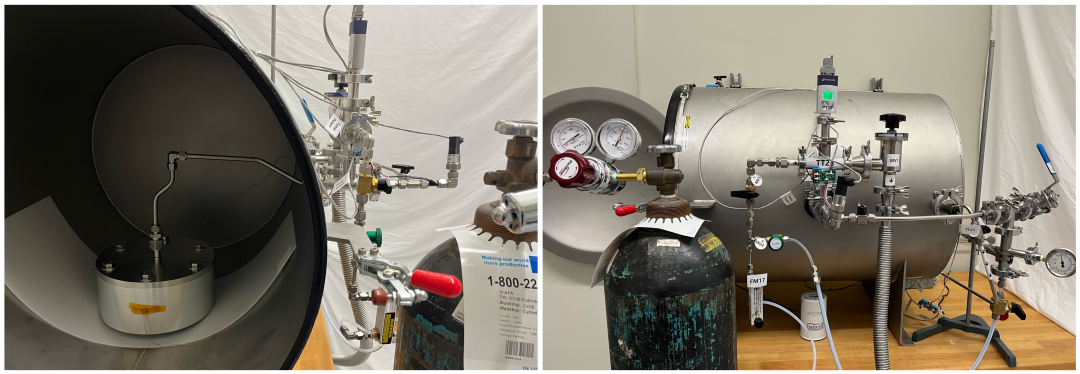

Figure 5.5: Experimental setup used to measure the permeation rates of lower mass noble gases and radon. The setup includes a vacuum holding tank, a permeation chamber, pressure transducers, and temperature sensors. A radon detector (not pictured) is used for the radon permeation rate measurement.

5.2.1 The Gas Permeation Chamber

The apparatus designed to contain the permeating gases consists of an aluminum main body, mated with a custom 9.5" stainless steel flange. A VCR fitting is welded at the centre of the flange to allow connection to the gas fill line. The central cavity of the aluminum body has been bored out to a volume of (1.218±0.001) litres. The diameter and bore height were measured with vernier calipers, with a measurement uncertainty of ±0.05 mm. To ensure adequate compression of the Parker PTFE seal, a feeler gauge was used to achieve a uniform gap of 0.05 mm between the aluminum body and the stainless steel flange. In anticipation of potential material deformation or relaxation that could compromise seal integrity, the system was subjected to a 24-hour stabilization period and a helium leak check prior to the integration of the GPC into the vacuum holding tank system. The placement of the GPC within the vacuum holding tank is shown in Figure 5.5 and a labelled CAD schematic is shown in Figure 5.6.

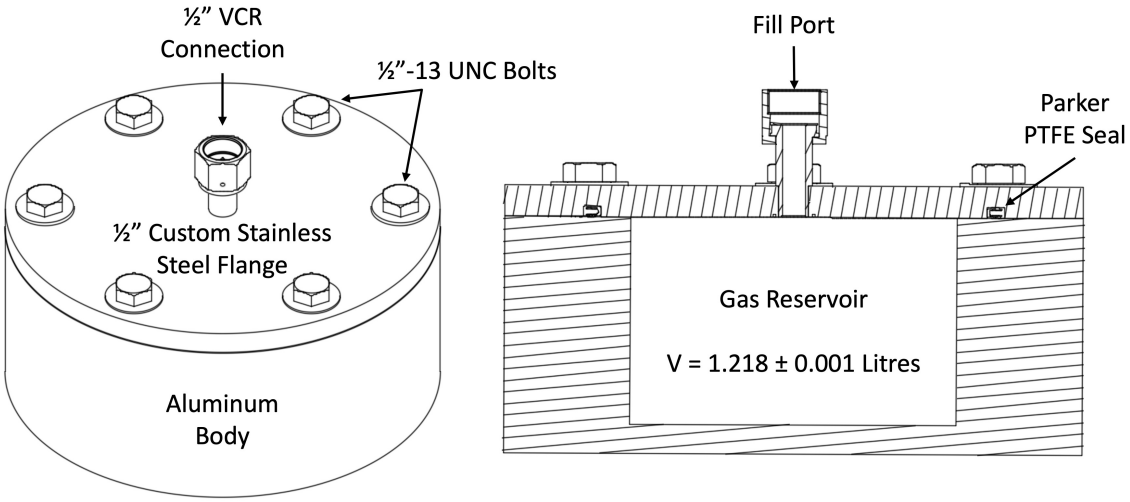

Figure 5.6: Labelled schematic of the Gas Permeation Chamber.

5.2.2 Geometrical Analysis of the Parker PTFE Seal

The Parker PTFE seal used in the GPC is a scaled-down version of ones that will be used in the PICO-500 inner vessel. The GPC seal has an inner diameter of 159.66 mm and an outer diameter of 165.6 mm, while the PICO-500 seals have an inner diameter of 477.00 mm and an outer diameter of 482.94 mm. This makes the PICO-500 seals approximately 2.98 times larger in diameter than the GPC seals. Apart from the difference in diameter, both seals use the same material, design, and thickness. The geometry of a compressed seal was determined by a finite element analysis using Autodesk Fusion 360. Figure 5.7 demonstrates the simulation in three steps were the seal is compressed from a gap a 1.07 mm to 0.05 mm.

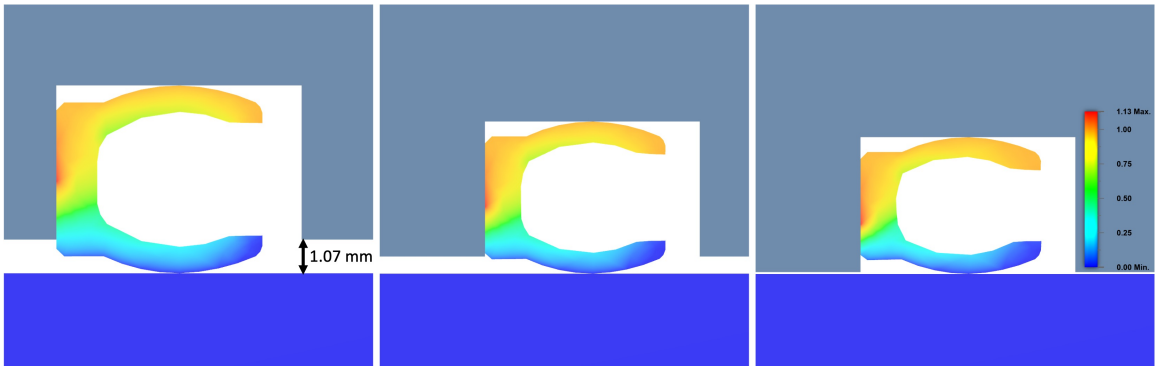

Figure 5.7: Autodesk Fusion 360 simulation of the Parker PTFE seal compression to a 0.05 mm gap during flange displacement, used to estimate the active permeation area and effective thickness of the seal.

Active Permeation Surface Area

The active surface area of a compressed PTFE seal for permeation to occur was determined using the CAD modelling program, Autodesk Fusion 360. The surface area can be calculated by selecting the 'measure' tool and applying it to each face in the active region of the 3D model as highlighted in Figure 5.8. Upon calculating the surface area of each face, these values were summed to determine the total active surface area and are individually provided in Table 5.1. The total active surface area was calculated to be 52.62 ± 2.79 cm^2. Applying the same procedure to a

PICO-500 scale model of a compressed PTFE seal produced an active surface area of 155.69 ± 8.32 cm^2.

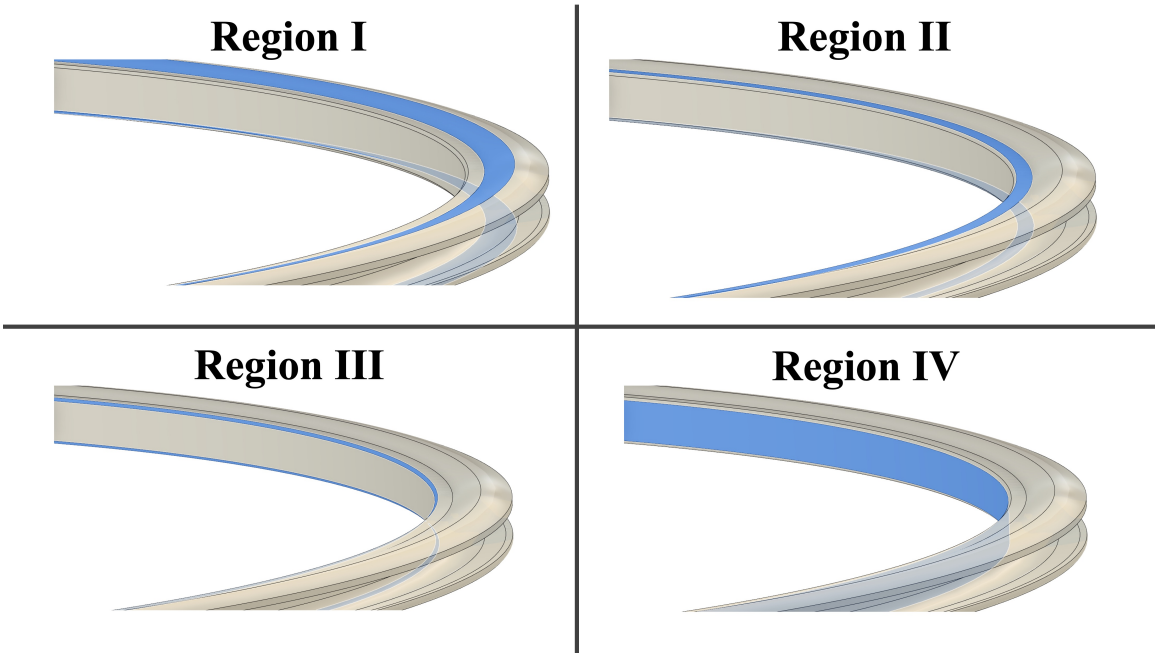

Figure 5.8: Active surface area regions for permeation to occur highlighted using the compressed PTFE seal CAD model. Regions are defined by different planar and curved segments. The total active surface area is the sum of all four regions and was found to be 52.62 cm^2 for the GPC seal.

Region	GPC Seal Surface Area [cm^2]	GPC Seal Surface Area [cm^2] (Compressed)	PICO-500 Seal Surface Area [cm^2]	PICO-500 Seal Surface Area [cm^2] (Compressed)
I	22.87	22.26	66.99	65.22
II	11.61	11.6	34.46	34.42
III	3.21	3.18	9.59	9.50
IV	20.51	15.58	61.29	46.55
Total Active Surface Area	58.20	52.62	172.33	155.69

Table 5.1: Surface areas of regions I through IV for the GPC and PICO-500 seals, along with the total combined surface area of a single PTFE seal, were determined. These results were obtained from CAD models of the Parker PTFE seal, analyzed in both uncompressed and compressed states. Definitions of the regions can be found in Figure 5.8.

Effective Seal Thickness

To determine the effective thickness of the Parker PTFE seal, a DXF file, derived from the CAD model of a 2D representation of a compressed PTFE seal, was used. This file was imported into a Python script, designed to generate lines from starting points along the high-pressure side (active permeation boundary) to the nearest termination point on the low-pressure side (non-active boundary). The sealing contact point was determined to be a distance of 3.572 mm beyond the inner diameter of the seal, based on the apex position within the CAD program, marking the division between the two boundaries.

The actual contact area, rather than a singular point, exhibited a thickness measured at 1.3 mm based on the ring indentation observed on an acrylic testing chamber from the seal. Consequently, a condition was added to the script to exclude paths that started near the contact point and traversed horizontally.

The script also included a correction to account for the increased surface area at larger radii of the seal. Given the diversity of permeation paths, the effective thickness was approximated by averaging both the arithmetic and harmonic means. This method, formulated below, offers a conservative estimate, aiming to account for an unweighted relationship between path lengths and a weighted average derived from the harmonic mean. This approach broadly addresses the dependencies between seal thickness and permeation rates.

$$l = \frac{\langle l \rangle_{\text{Arithmetic}} + \langle l \rangle_{\text{Harmonic}}}{2} \tag{5.11}$$

$$\text{Error Estimate} = |\langle l \rangle_{\text{Arithmetic}} - \langle l \rangle_{\text{Harmonic}}| \tag{5.12}$$

with the harmonic mean defined as:

$$\langle l \rangle_{\text{Harmonic}} = \frac{N}{\sum \frac{1}{X_i}} \tag{5.13}$$

Here, l represents the effective seal thickness, N the number of paths simulated, and X_i the ith path lengh simulated. From Equations 5.11 and 5.12 the effective thickness was calculated to be 0.9 ± 0.1 mm. The variance in thickness is attributed to the geometric complexity rather than a statistical variability. Figure 5.9 illustrates the distribution of all path lengths across the seal.

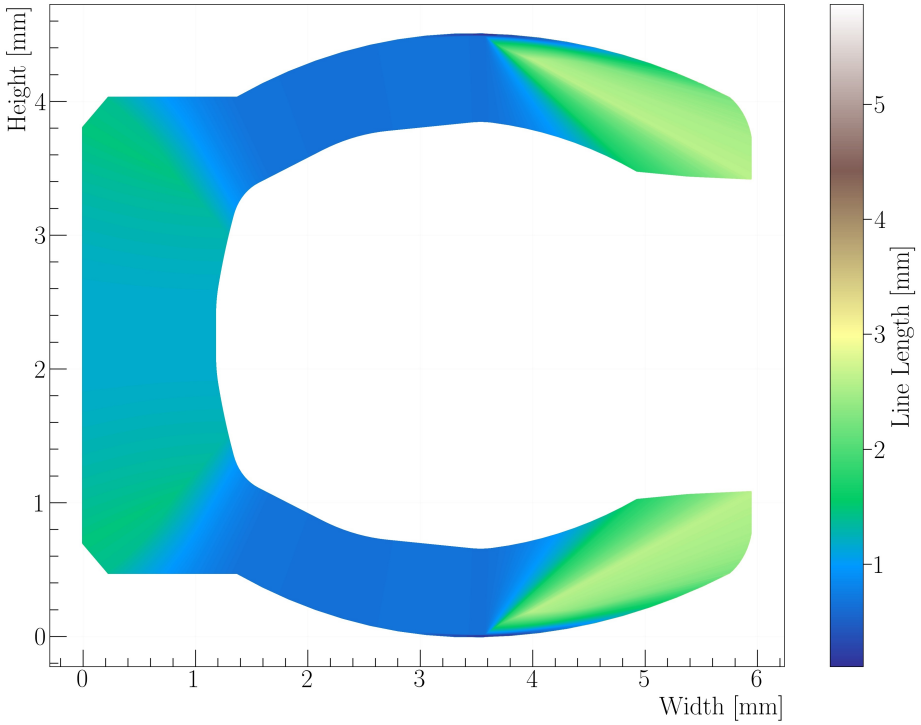

Figure 5.9: Trajectory lines traversing the 2D profile of the compressed PTFE seal. Shown are diverse path lengths from the active permeation boundary to the non-active permeation boundary. The effective thickness of the seal was calculated to be (0.9±0.1) mm.

5.3 Radon Permeability Estimate via Noble Gas Proxies

Empirical research has shown that the logarithm of noble gas permeation coefficients, along with diffusion and solubility coefficients, tends to exhibit a linear relationship with the square of the kinetic atomic diameter [49], which is a description of the effective size of colliding atoms. Figure 5.10 demonstrates the dependence of the log

of the permeation coefficient to the atomic diameter squared of noble gases through a variety of sealing materials [55].[3] While this trend is not exclusive to noble gases, their inert nature and spherical symmetry make it a particularly common observation.

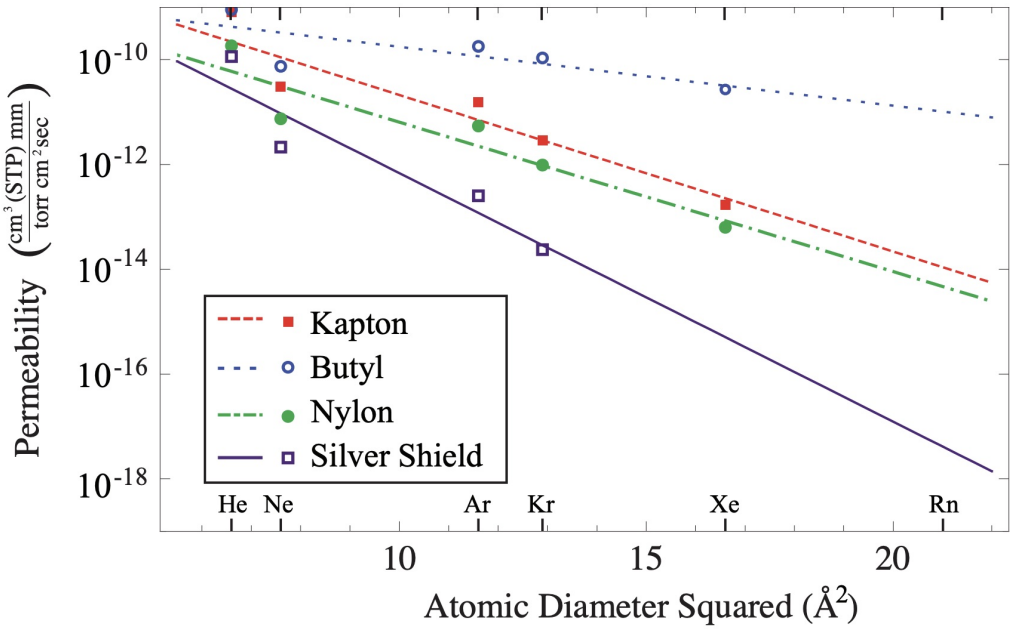

Figure 5.10: Permeability of noble gases through different sealing materials as a function of the square of atomic diameter [55].

5.3.1 Noble Gas Permeation Model

The dynamics of a gas in a closed constant-volume system are defined by the pressure and temperature of the gas. The ideal gas law provides a straightforward model for these dynamics, describing the gas as a collection of small, non-interacting particles that undergo elastic collisions with the chamber walls, thereby generating pressure within the chamber. The temperature of the gas correlates with the kinetic energy of the particles and can be influenced by ambient temperature fluctuations if the system is not thermally isolated. Gas pressure and temperature are directly related and influence each other.

[3]Reprinted from "Permeability of noble gases through Kapton, butyl, nylon, and 'Silver Shield'", S.J. Schowalter, C.B. Connolly, and J.M. Doyle, 267-271, Copyright (2010), with permission from Elsevier

The ideal gas law accurately describes the behavior of real, non-interacting gases, particularly at pressures where the volume occupied by gas molecules is significantly smaller than that of the chamber. The ideal gas law is given by [59]:

$$PV = nRT \tag{5.14}$$

Where P is the pressure of the gas, V is the volume of the chamber, n is the number of moles, R is the universal gas constant, and T is the absolute temperature of the gas. The universal gas constant is defined as R = 8.3145 $J \cdot mol^{-1} \cdot K^{-1}$ [59].

In the dynamics of an ideal gas permeating through a barrier, the number of moles on the upstream pressure side decreases over time, affecting the pressure and temperature of the system. Upon reaching steady-state permeation, the molar flow rate remains constant. Denoted as $\dot{n}$, this rate can be determined by the pressure loss rate ($\frac{dP}{dt}$) obtained by differentiating the ideal gas law. A higher-order effect can arise when ambient temperature fluctuations influence the gas pressure. A complete description of the molar flow rate that includes changes in temperature over time ($\frac{dT}{dt}$), is as follows:

$$\frac{dn}{dt} = \dot{n} = \frac{dP}{dt}\frac{V}{RT} - \frac{PV}{RT^2}\frac{dT}{dt} \tag{5.15}$$

Using the ideal gas molar volume conversion, the molar flow rate can be converted directly into the volumetric flow rate at standard temperature and pressure (STP), defined as $P_{\mathrm{STP}} = 101,325$ Pa and $T_{\mathrm{STP}} = 273.15$ K. This ensures consistency in measurements across different experimental conditions and setups. The STP corrected volumetric flow rate is calculated as follows:

$$Q_{STP} = \left(R\frac{T_{\mathrm{STP}}}{P_{\mathrm{STP}}}\right) \cdot \dot{n} = (22,414\frac{\mathrm{cm}^3}{\mathrm{mol}}) \cdot \dot{n} \tag{5.16}$$

If pressure and temperature data of an ideal permeating gas are recorded over time, the permeation coefficient can be calculated using this corrected volumetric flow rate,

along with the experimental parameters such as the thickness of the barrier (l), the surface area for permeation (S), and the differential pressure across the barrier (ΔP):

$$K_p = \frac{Q_{\mathrm{STP}} l}{S \Delta P} \tag{5.17}$$

5.3.2 Procedure

To estimate the radon permeability through the Parker PTFE seal, the permeation coefficients for the five lower mass noble gases were determined. This experimental approach is a modified version of the ISO 15105-1 standard procedure for measuring permeability, which involves maintaining a constant upstream pressure while monitoring the rise in downstream pressure over time [60]. This pressure rise is directly related to the volumetric flow rate of the gas through the membrane barrier. However, due to the significant volume difference between the vacuum holding tank (213 litres) and the GPC (1.2 litres), the pressure increase in the downstream volume is too small to detect with the available sensor resolution and duration of the experiment.

The experiment was adapted to measure the drop in the upstream pressure only. The adapted procedure is outlined below where all valve numbers referenced are shown in the Piping and Instrumentation Diagram (Figure 5.11):

- Isolate the vacuum holding tank from the radon emanation chamber and maintain a constant vacuum on the system using an ACP-15 vacuum pump.
- Evacuate the permeation chamber and fill lines with a second ACP-15 pump. A tee connection enables parallel connections to the gas cylinder and vacuum pump, ensuring complete system evacuation to prevent contamination.
- Start the Radon DAQ LabVIEW program for Slow-ADC data collection and pressure monitoring during the filling process.
- Isolate the permeation chamber (V6) and isolate the vacuum pump from the fill line to maintain a vacuum in the system before turning the pump off.

- Open the gas cylinder to pressurize the lines, and then gradually open the isolation valve (V6) of the permeation chamber to control the pressure increase and fill.

- Close all valves after filling.

The purity of the upstream gas is critical for the accurate results in this method as pressure drops in the upstream pressure are the sum of partial pressure drops if more than one gas is present. The upstream pressure drop is then used to determine the volumetric gas flow rate as opposed to the downstream pressure rise as outlined in the ISO 15105-1 standard procedure. Additionally, it is recommenced that a gas regulator is to be set prior to filling the permeation chamber to prevent exceeding a threshold pressure value. In this particular setup, the pressure transducer had a maximum readout of 28 psia (1930 mBar). By keeping the vacuum holding tank pressure in vacuum conditions, this effectively makes the GPC pressure the differential pressure value in the experiment. The vacuum holding tank was held at a constant pressure of 0.03 mBar.

Over a period of 3.5 days, pressures were recorded along with temperature readings. Since the pressure differential is large the entire run, the permeation rate stays approximately constant for the duration of the measurement. After each measurement, the gas was evacuated using a vacuum pump and the system was continually pumped down for 1-2 hours to ensure maximum gas dissolution and removal from the permeation chamber.

5.3.3 Data Collection

The pressure and temperature data were collected using an updated version of the UofA Radon DAQ (V3.0) LabVIEW program. One significant addition is the capability to save Slow-ADC data into a CSV file at a frequency of 1 Hz. A Python library, specifically developed for this project, offers various functions for data analy-

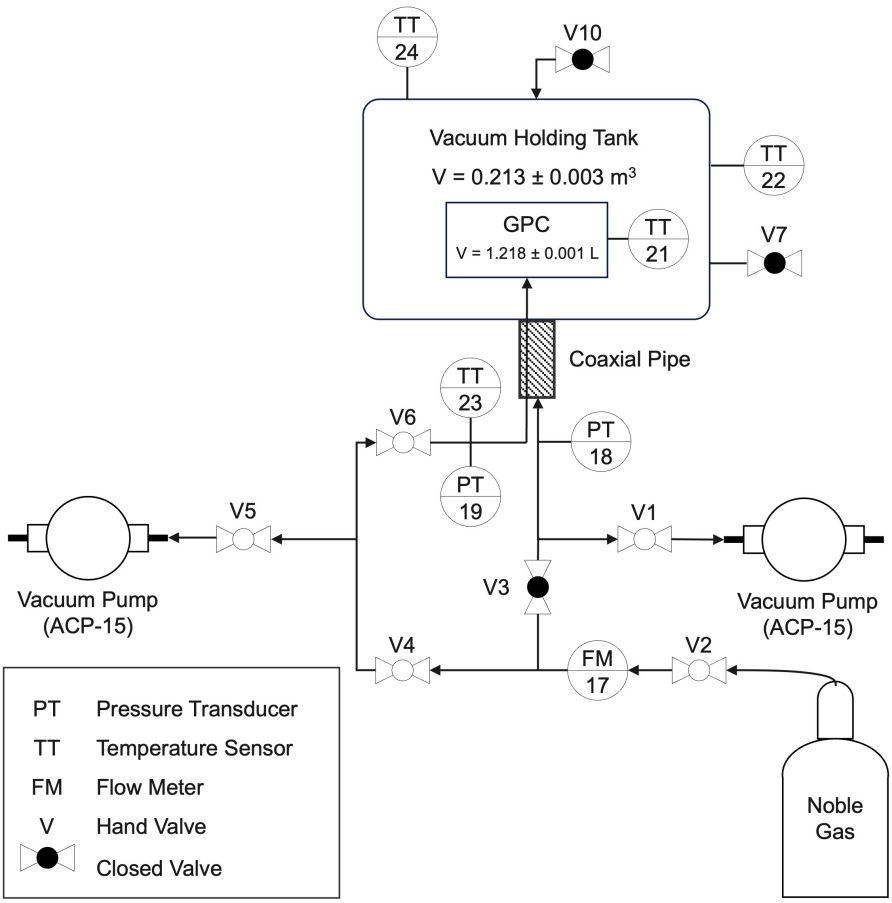

Figure 5.11: Piping and Instrumentation Diagram for the noble gas permeation setup.

sis. These functions include extracting data from CSV files, applying simple moving averages, and modelling the data to determine the permeation coefficient.

The moving average function, which requires a user-specified window size, was necessary to enhance the precision of measurements. This function was applied to all Slow-ADC data. Due to the limitations of the 10-bit ADC, pressure measurements had a resolution of ± 2 mBar, and temperature measurements had a resolution of ± 0.07°C.

All the datasets analyzed in this section use a window size of 10 minutes, which gives N=600 data points for every interval. This value was manually chosen to balance averaging out bit noise in the data, while maintaining ambient temperature influences for improved data modelling.

5.3.4 Results and Discussion

The combined datasets showing the pressures and temperatures throughout the duration of the measurement are presented in Figures 5.12 and 5.13, respectively. To understand the behavior of the gas system, two pressure transducers (PT18 for the vacuum holding tank and PT19 for the GPC fill line - Figure 5.11) were used along with indirect measurements of gas temperature obtained from the strategically placed temperature sensors. It was found that averaging the temperature readings from sensors TT23 (located on the fill line) and TT21 (located on the GPC body) with weights of 0.8 and 0.2, respectively, yielded consistent results among the datasets, except for Helium, which was externally heated. In this case, only temperature sensor TT21 accurately reflected the gas temperature, as the heating process eliminated ambient temperature influences.

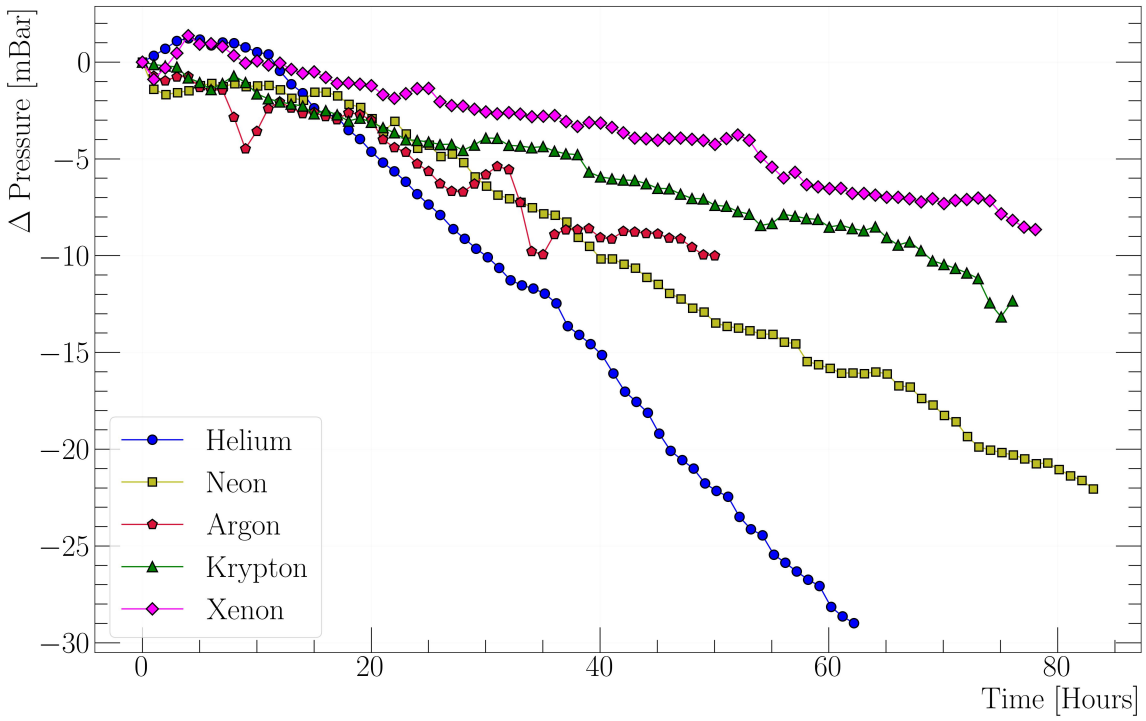

Figure 5.12: Pressure changes of the five tested noble gases—He, Ne, Ar, Kr, and Xe—permeating through the Parker PTFE seal over the measurement run-time. Lighter gases show higher pressure loss rates as expected.

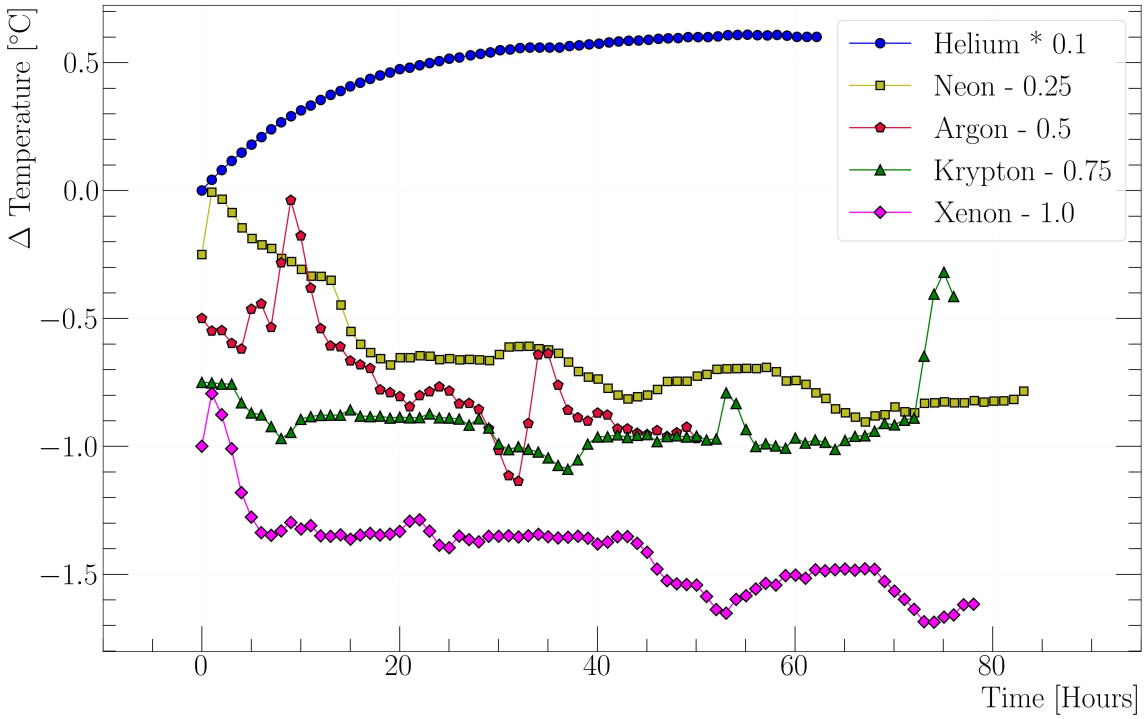

Figure 5.13: Temperature fluctuations during permeation testing of the five noble gases—He, Ne, Ar, Kr, and Xe—permeating through the Parker PTFE seal over the measurement run-time. These variations primarily reflect the lab's ambient conditions. Helium underwent external heating to mitigate ambient temperature effects.

To accurately determine the pressure loss rate, a data cut was applied to all datasets, excluding the first 20 hours of each measurement, with exceptions. This exclusion accounts for the adiabatic compression experienced by the gas during the filling process of the initially evacuated GPC. Typically, it took 10 to 15 hours for the gas to reach thermal equilibrium with the surroundings, although the equilibrium time varied among datasets. In the case of the second run helium dataset (the first was removed from analysis), the initial 35 hours were excluded due to the time needed to achieve thermal equilibrium while heating the system. Additionally, the argon data were analyzed from the 50-hour to the 87-hour mark, focusing on a region of temperature stability, as cyclic lab temperature fluctuations during the measurement affected data quality.

The observation of the argon dataset influenced the decision to heat the second

helium measurement run to maintain a controlled constant temperature during gas permeation. The first helium run was removed from the analysis due to a faulty connection on the temperature sensor TT21, and a second argon dataset was excluded due to significant ambient temperature fluctuations. The high-quality data from the second helium run suggests a new procedural step: adding an external heat source to mitigate ambient temperature fluctuations for all future permeation measurements using this method.

Figure 5.14 illustrates the fitting process used to determine the pressure loss rate for neon over the 80-hour run-time. A least-squares fit was applied, returning a result of $9.21 \pm 0.09 \times 10^{-5}$ mBar/s with a reduced chi-squared of 0.26. The poor chi-squared is a reflection of the large uncertainties in the pressure due to the quantization error from the Slow-ADC. The change in temperature, dT/dt, was determined by taking a numerical derivative of the temperature at each time step to properly calculate the volumetric flow rate using Equation 5.17.

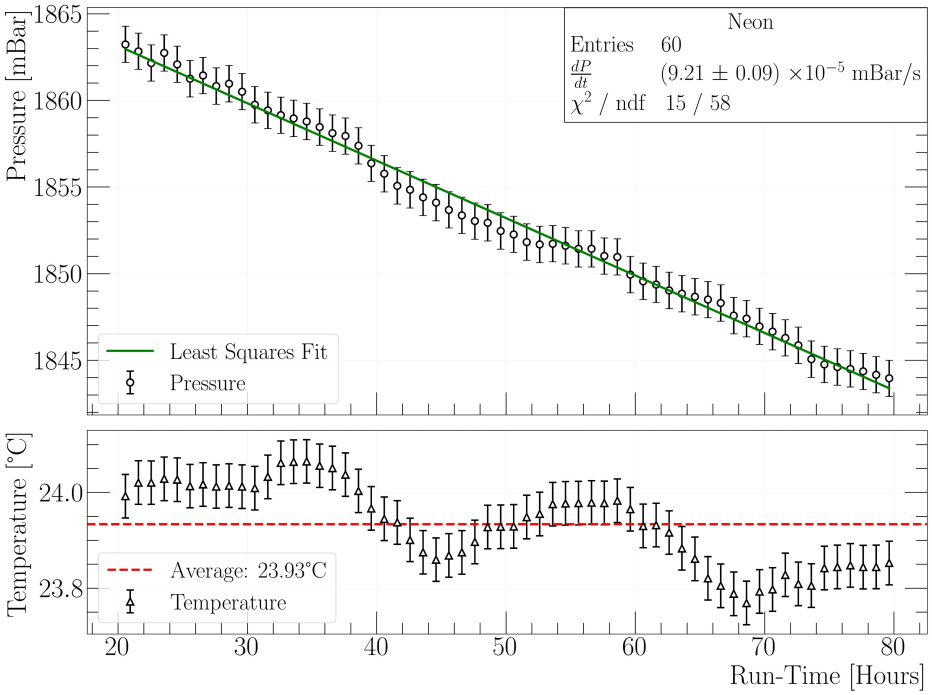

Figure 5.14: Pressure and temperature changes of neon gas permeating through the Parker PTFE seal over the 80 hour run-time. The top panel shows pressure data. The bottom panel displays the weighted gas temperature measurements.

A summary table of the experiment conditions and fit parameters can be found in Table 5.2. The calculated permeation coefficients for each noble gas along with the extrapolated radon permeation coefficient of the Parker PTFE seal can be found in Table 5.3.

Gas	P_{initial} (mBar)	$\overline{T}_{Weighted}$ (°C)	dP/dt ($\times 10^{-5}$mBar/s)	χ^2_{red} (dP/dt)	$\overline{dT}/dt$ ($\times 10^{-6}$K/s)	$\overline{Q}$ ($\times 10^{-5}$ $\frac{\text{cm}^3\text{(STP)}}{\text{s}}$)
He*	1647	31.4	-14.7 ± 0.32	0.05	-5.54	19.2 ± 0.4
Ne	1866	23.9	-9.21 ± 0.85	0.27	-0.64	9.7 ± 0.1
Ar	1915	23.8	-7.33 ± 0.18	0.52	-2.76	6.2 ± 0.4
Kr	1824	23.8	-4.00 ± 0.09	0.05	-0.10	4.4 ± 0.2
Xe	1770	23.8	-4.34 ± 0.09	0.13	-1.27	4.0 ± 0.2

Table 5.2: Summary table of experimental conditions, fit parameters, and goodness of fit measures from the noble gas experiments. Temperature sensor TT23 and TT21 were weighted by 0.8 and 0.2, respectively.
*Denotes the gas was heated with an external constant heat source. Only TT21 was used for this analysis.

Gas	Kinetic Diameter (Å)	K_p ($\times 10^{-10}$ $\frac{\text{cm}^3\text{(STP)}\cdot\text{cm}}{\text{s}\cdot\text{cm}^2\cdot\text{cm-Hg}}$)
He*	2.6	26.13 ± 3.44
Ne	2.75	12.44 ± 1.71
Ar	3.4	14.22 ± 3.06
Kr	3.6	8.92 ± 1.72
Xe	3.96	7.90 ± 1.30
Rn	4.57	$5.10^{+0.92}_{-1.10}$ (Extrapolated)

Table 5.3: Summary table of the kinetic atomic diameters and calculated permeation coefficients for each noble gas. The kinetic atomic diameters for the noble gases are sourced from [54, 61]. The radon kinetic atomic diameter was sourced from [62].

Using the logarithm of the five experimentally determined permeation coefficients plotted against the square of their kinetic diameters, the radon permeation coefficient was extrapolated to be $K_p = 5.10^{+0.92}_{-1.10} \times 10^{-10}\ \frac{\mathrm{cm^3(STP)\,cm}}{\mathrm{s\,cm^2\,cm\text{-}Hg}}$, as depicted in Figure 5.15. The permeation coefficient is known to be temperature dependent, suggesting that the calculated permeation coefficient of helium is not in line with the trend of the other four gases as it is on a different isotherm. However, this temperature dependency was not considered during the extrapolation of the radon permeation coefficient. It is assumed that the value calculated for helium is not significantly different from what it would be if derived under the same isotherm as the other gases. The uncertainty in the extrapolated radon permeation coefficient was assessed by determining the maximum best-fit using the values of helium and argon in one limit, and the minimum best-fit of neon and krypton in the second limit. The overall best-fit was determined by fitting the least squares fit of all the data points.

The calculation of K_p values at each time step allows for obtaining the overall time-averaged K_p by integrating these values across the duration of the experiment, symbolized by t_f:

$$\overline{K_p} = \frac{1}{t_f} \int_0^{t_f} K_p(t) dt \tag{5.18}$$

The uncertainty in the permeation coefficient at any point in time, δK_p, arises from the uncertainties in flow rate Q, seal thickness l, active surface area S, and differential pressure ΔP, calculated as follows:

$$\delta K_p = K_p \sqrt{\left(\frac{\delta Q}{Q}\right)^2 + \left(\frac{\delta l}{l}\right)^2 + \left(\frac{\delta S}{S}\right)^2 + \left(\frac{\delta \Delta P}{\Delta P}\right)^2} \tag{5.19}$$

To determine the error for the time-averaged permeation coefficient, $\overline{\delta K_p}$, the square root of the average of the squared individual errors over all N measurements is computed:

$$\overline{\delta K_p} = \sqrt{\frac{1}{N}\sum_{i=1}^{N}\left(\delta K_{p,i}\right)^2} \tag{5.20}$$

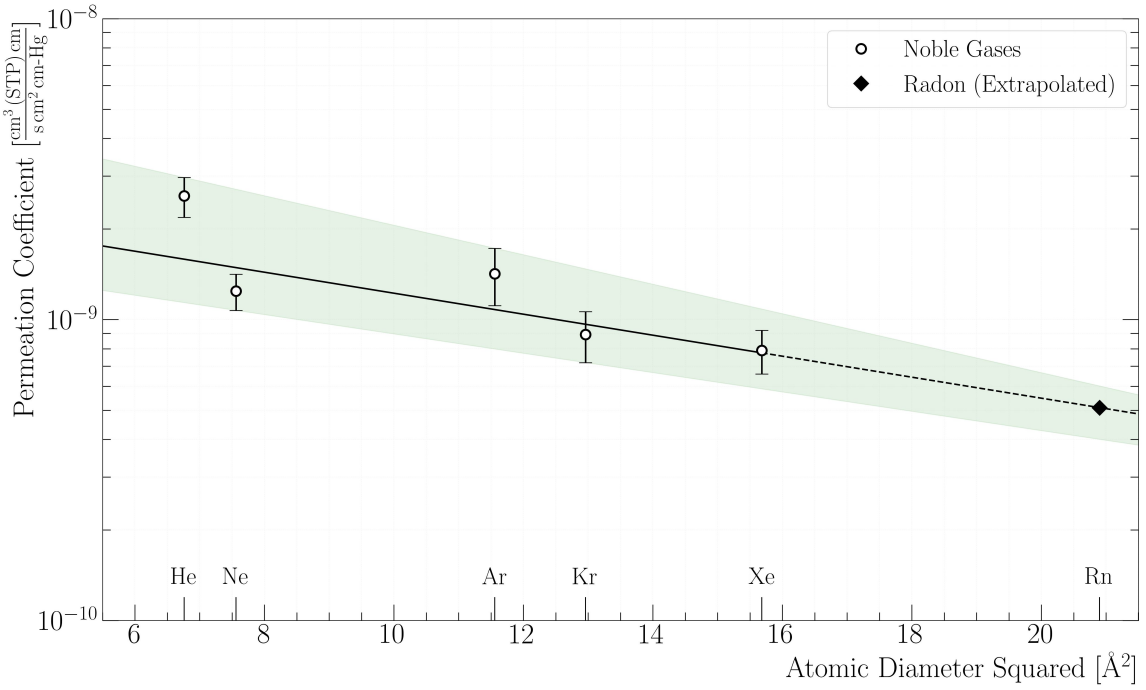

Figure 5.15: Semi-log plot of the permeation coefficient against the atomic diameter squared for the five lower mass noble gases, extrapolated to radon. The green band represents the fit uncertainty, with the upper limit derived from the maximum best fit of helium and argon, and the lower limit derived from the minimum best fit of neon and krypton.

5.4 Direct Radon Permeability Measurement

5.4.1 Radon Permeation Model

The transport and decay dynamics of radon permeating from a gas permeation chamber and into an outer detection volume are governed by two coupled ordinary differential equations:

$$\begin{aligned}\frac{dA_{\mathrm{GPC}}}{dt} &= -r_{\mathrm{perm}}(A_{\mathrm{GPC}} - A_{\mathrm{Detector}}) - \lambda_{\mathrm{Rn}}A_{\mathrm{GPC}} \\ \frac{dA_{\mathrm{Detector}}}{dt} &= +r_{\mathrm{perm}}(A_{\mathrm{GPC}} - A_{\mathrm{Detector}}) - \lambda_{\mathrm{Rn}}A_{\mathrm{Detector}}\end{aligned} \tag{5.21}$$

Where A_{GPC} is the radon activity within the GPC, A_{Detector} is the radon activity within the detection volume, λ_{Rn} is the decay constant of Radon-222, and r_{perm} is the permeation rate constant.

By performing a numerical integration of this model using radon activity data collected by a radon detector, it is possible to extract the permeation rate constant, r_{perm}, as a single fitting parameter.

By applying appropriate initial conditions for a radon permeation measurement, and assuming that the radon activity in the Gas Permeation Chamber is much greater than that in the detection volume ($A_{\mathrm{GPC}} \gg A_{\mathrm{Detector}}$) at any time t during a measurement, the equations in 5.21 can be simplified as follows:

$$\left.\begin{aligned} \frac{dA_{\mathrm{GPC}}}{dt} &= -r_{\mathrm{perm}}A_{\mathrm{GPC}} - \lambda_{\mathrm{Rn}}A_{\mathrm{GPC}} \\ \frac{dA_{\mathrm{Detector}}}{dt} &= +r_{\mathrm{perm}}A_{\mathrm{GPC}} - \lambda_{\mathrm{Rn}}A_{\mathrm{Detector}} \end{aligned}\right\} \quad \begin{aligned} A_{\mathrm{GPC}}(t=0) &= A_0 \\ A_{\mathrm{Detector}}(t=0) &= 0 \end{aligned} \tag{5.22}$$

With this simple coupled differential equation and this set of initial conditions where A_0 is the initial radon activity, the analytic solution then takes the form:

$$\begin{aligned} A_{\mathrm{GPC}}(t) &= A_0 e^{-(\lambda_{\mathrm{Rn}}+r_{\mathrm{perm}})t}, \\ A_{\mathrm{Detector}}(t) &= A_0\left[1 - e^{-r_{\mathrm{perm}}t}\right]e^{-\lambda_{\mathrm{Rn}}t} \end{aligned} \tag{5.23}$$

In the first equation, the addition of the permeation rate constant (r_{perm}) to the decay constant (λ_{Rn}) acts as an effective decay constant, accelerating the loss of activity inside the chamber as expected. The second equation describes radon activity within the detector, comprising of two exponential terms: $1 - e^{-r_{\mathrm{perm}}t}$, which models the accumulation of radon over time as it permeates into the detection volume; and $e^{-\lambda_{\mathrm{Rn}}t}$, the exponential decay term. The overall effect is an increase in radon activity due to permeation in the detection volume, modulated by the ongoing decay of radon. Together, these equations provide a comprehensive model for determining the evolution of radon gas within both the GPC and the detection volume at any given time.

Once the permeation rate constant is determined by numerical integration techniques, Equation 5.23 can be combined with the ideal gas law (Equation 5.14) to calculate the radon gas differential pressure $\Delta P(t)$ across the seal at any time t during the measurement:

$$\Delta P(t) = \frac{R\overline{T}}{\lambda_{\mathrm{Rn}} N_A} \left[\frac{A_{\mathrm{GPC}}(t)}{V_{\mathrm{GPC}}} - \frac{A_{\mathrm{Detector}}(t)}{V_{\mathrm{Detector}}} \right] \tag{5.24}$$

Where $\overline{T}$ is the average absolute temperature of the system, N_A is Avogadro's constant, V_{GPC} is the inner volume of the GPC, and V_{Detector} is the volume of the detection system (Vacuum holding tank and the radon emanation chamber).

The fit parameter r_{perm} quantifies the fraction of radon activity expected to permeate through the seal per unit time. The product $r_{\mathrm{perm}} \cdot A(t)_{\mathrm{Total}}$ then represents the total rate of radon activity permeating across the seal, $\dot{A}_{\mathrm{perm}}$. Evaluating the permeating activity allows for conversion into a volumetric flow rate through the seal:

$$Q_{\mathrm{STP}} = \left(R \frac{T_{\mathrm{STP}}}{P_{\mathrm{STP}}} \right) \cdot \frac{\dot{A}_{\mathrm{perm}}}{\lambda_{\mathrm{Rn}} N_A} = (22,414 \frac{\mathrm{cm}^3}{\mathrm{mol}}) \cdot \frac{\dot{A}_{\mathrm{perm}}}{\lambda_{\mathrm{Rn}} N_A} \tag{5.25}$$

Where the ratio $\frac{\dot{A}_{\mathrm{perm}}}{\lambda_{\mathrm{Rn}}}$ represents the number of permeating radon atoms per unit time.

Calculating ΔP and Q enables the determination of the permeation coefficient in units compatible with the noble gas measurements, facilitating direct methodological comparison. Substituting Equation 5.24 and Equation 5.25 into the permeation coefficient Equation 5.9 yields:

$$K_p(t) = \frac{l}{S} \frac{\dot{A}_{\mathrm{perm}}}{\overline{T}} \left(\frac{T_{\mathrm{STP}}}{P_{\mathrm{STP}}} \right) \left[\frac{A_{\mathrm{GPC}}(t)}{V_{\mathrm{GPC}}} - \frac{A_{\mathrm{Detector}}(t)}{V_{\mathrm{Detector}}} \right]^{-1} \tag{5.26}$$

5.4.2 Procedure

The measurement of radon permeability through the Parker PTFE seal utilizes the setup described in Section 5.3, with the addition of the radon emanation chamber described in Sections 4.2 to 4.4. The configuration changes are detailed in the Piping and Instrumentation Diagram shown in Figure 5.16. Temperature monitoring during the experiment is conducted with the sensor located on the coaxial fill line (TT23). This sensor provides the average temperature of the system throughout the duration of the experiment.

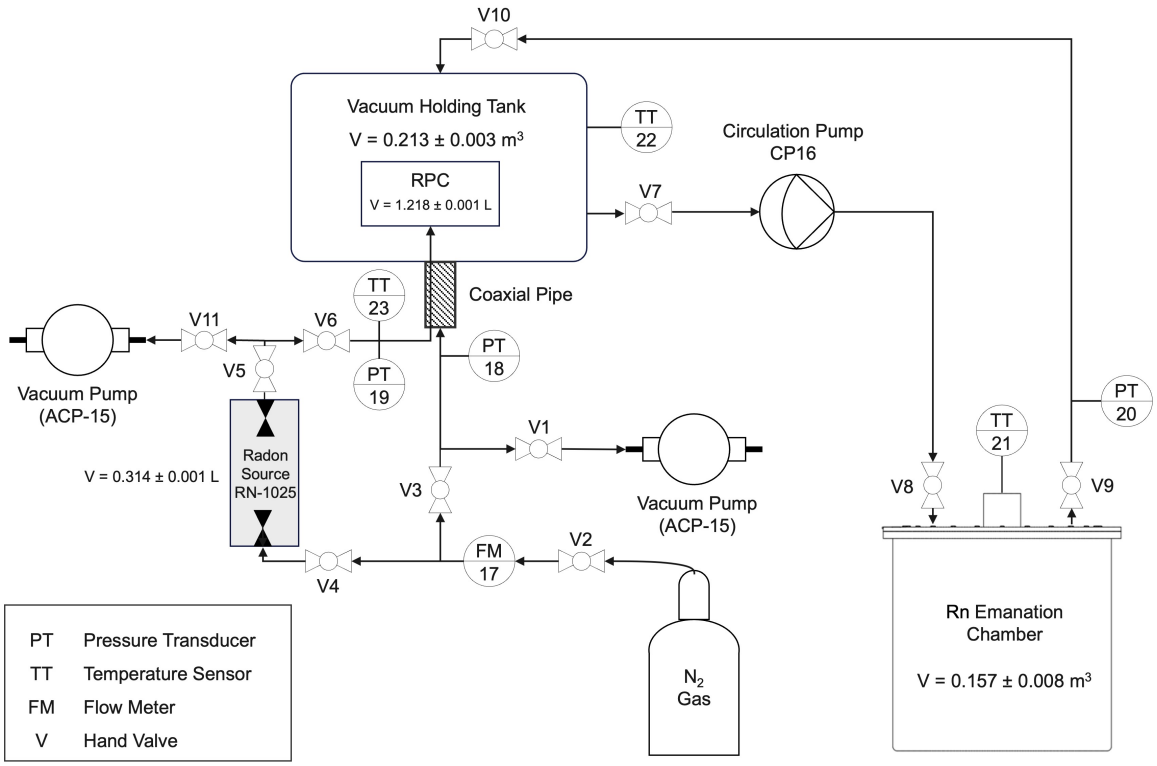

Figure 5.16: Piping and Instrumentation Diagram of the radon permeation measurement.

Prior to the permeation measurement, the system was subjected to a background run equal to one half-life of Radon-222 to allow any residual radon in the system to decay to intrinsic background levels adhering to the procedure outlined in Section 4.3.3. Subsequently, the system was prepared for a radon permeation measurement

following the steps detailed below:

- Evacuate and then fill the GPC with nitrogen gas to 850 mBar.
- Isolate the GPC (by closing valve V6) and the gas cylinder, then evacuate both the fill line and the GPC.
- Repeat this purging process 2-3 more times to effectively remove any ambient radon.
- After the last purge, the GPC is left under vacuum and isolated by closing V6.
- Start a new run on the Radon DAQ labVIEW program to monitor the radon fill. Ensure the high voltage supply is set to the operational value.
- Connect the radon source to the GPC fill line as shown in Figure 5.16.
- Open valves V5, V6, and the radon source output valve (gradually) to equalize the radon concentration between the radon source and GPC volume.
- Flow nitrogen gas through the radon source at a rate not exceeding 10 litres per minute, as recommended by the manufacturer [48], to transport the remaining radon from the source to the GPC. Lower flow rates are preferred.
- Fill the GPC up to the maximum readout of PT19 (28 psia) to maximize radon transfer into the GPC.
- Isolate the GPC and close all valves in reverse order: V6, V5, radon source output and input valves, and V4.
- Restart a new run in the Radon DAQ LabVIEW program to begin the data collection.

A critical value to determine, following these procedures, is the radon activity in the GPC after purging the source. The source was allowed to recharge for 21 days prior

to this measurement, yielding a total activity of 909 Bq, as calculated using Equation 4.12. Upon opening the source outlet valve, equilibrium between the radon source and the GPC was assumed, resulting in the dilution of the total radon concentration to 593 Bq per litre across the combined volume. Subsequent purging with nitrogen gas transported the remaining 186 Bq of activity into the GPC. After filling the GPC and initiating data collection with LabVIEW, a final purge of the radon source into an evacuated 10-litre tank, monitored using a RadonEYE detector, was performed. Initial readings revealed a residual activity of 6 Bq, confirming the source depletion and validating the initial activity estimate within the GPC to be within less than one percent of the expected activity, thus confirming the overall procedural methodology.

5.4.3 Data Collection

Data collection is conducted using the RadonDAQ (V3.0) LabVIEW program, which utilizes the custom 8-channel MCA (multi-channel analyzer) for processing event and Slow-ADC data, as detailed in Section 4.2. A Python script was developed to convert `ROOT` files into CSV files using the `Uproot` library.

Readings from the Slow-ADC, including pressure, temperature, and high voltage, were analyzed in Python. Python functions detailed in Section 5.3 were adapted and generalized to handle both types of measurements.

5.4.4 Results and Discussion

The experimental data collected from the radon detector system were analyzed to determine the radon permeation rate constant through the Parker PTFE seal. The permeation rate constant was determined through numerical integration of the experimental data using the model described by Equation 5.22. The best fit was obtained using a non-linear least squares method, with the resulting permeation rate constant found to be $r_{\text{perm}} = (206 \pm 1) \times 10^{-10}\,\text{s}^{-1}$ in the Polonium-214 decay channel and $r_{\text{perm}} = (209 \pm 1) \times 10^{-10}\,\text{s}^{-1}$ in the Polonium-218 decay channel. Figure 5.17 shows

the corrected activity count rates (Bq) binned every 4 hours throughout the 25-day measurement. The resulting reduced chi-squared values of 1.33 for Polonium-214 and 1.70 for Polonium-218 channel confirm that the model fits the data well enough for both decay channels.

Using the permeation rate constant parameters obtained from fitting the data of both decay channels, the radon permeation coefficient, K_p, of the Parker PTFE seal was calculated using Equation 5.26. The radon activity model of the system (black), GPC (red), and the detection volume (green) are shown in Figure 5.18 for the experiment run-time and were used to calculate the volumetric flow rate and differential pressure across the seal. The average temperature during the experiment was determined to be 296 K, and the volume of the detection system was calculated as 0.370 m^3. Given that K_p values are derived at every time step, the overall time-averaged K_p was determined by integrating these values over the entire duration of the experiment, as presented in the noble gas measurements Section 5.3.4 (Equations 5.19-5.21).

The Radon-222 time-averaged permeation coefficients, calculated using the Polonium-214 and Polonium-218 decay channels, were found to be $(5.33\pm0.69)\times10^{-10}$ $\frac{\mathrm{cm^3(STP)\,cm}}{\mathrm{s\,cm^2\,cm\text{-}Hg}}$ and $(5.40 \pm 0.70) \times 10^{-10}$ $\frac{\mathrm{cm^3(STP)\,cm}}{\mathrm{s\,cm^2\,cm\text{-}Hg}}$, respectively. The weighted time-average Radon-222 permeation coefficient is then $(5.37 \pm 0.49) \times 10^{-10}$ $\frac{\mathrm{cm^3(STP)\,cm}}{\mathrm{s\,cm^2\,cm\text{-}Hg}}$.

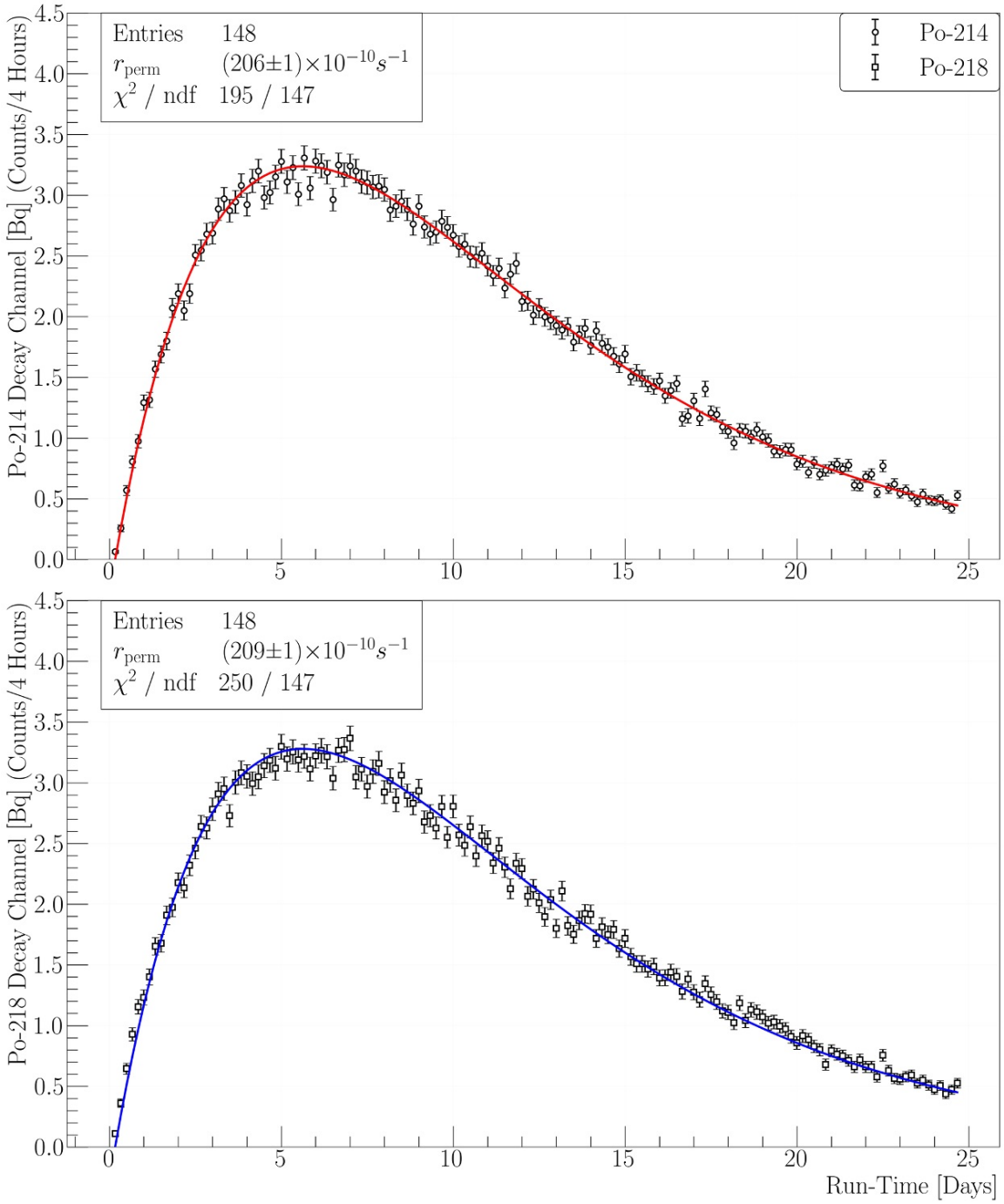

Figure 5.17: Measured radon activity over time for the Polonium-214 (top panel) and Polonium-218 (bottom panel) decay channels as radon permeates through the Parker PTFE seal. Error bars represent Poissonian uncertainties. The red curve (top panel) and blue curve (bottom panel) depict the best fit to the experimental data.

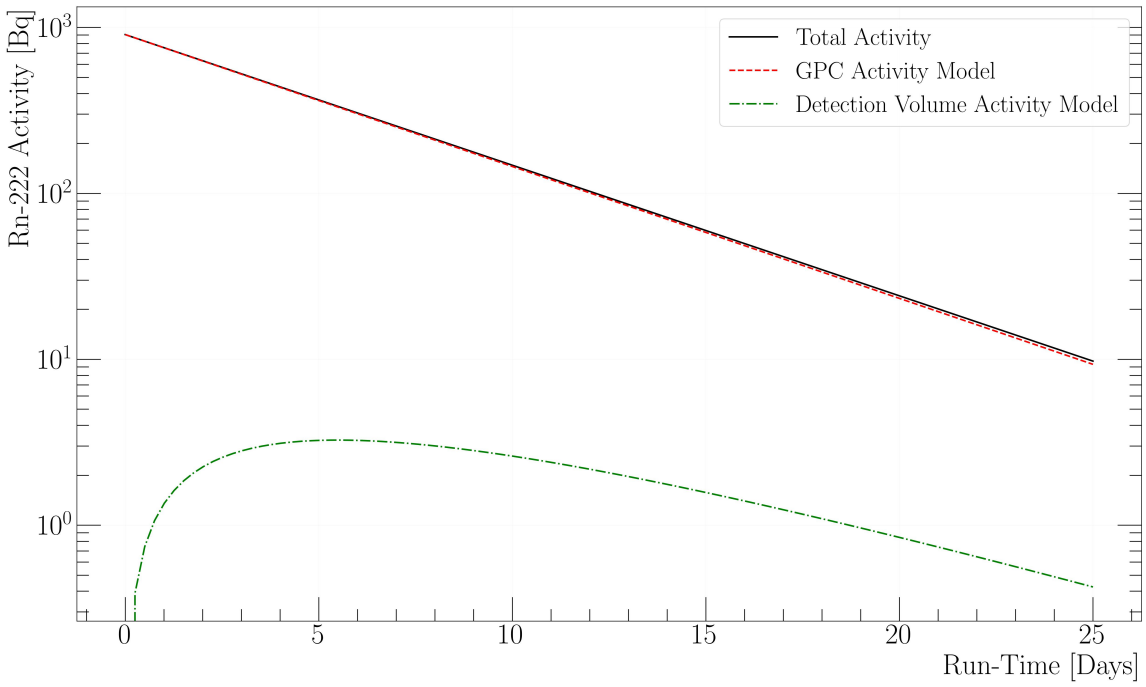

Figure 5.18: Modelled radon activity over time of the total activity, GPC, and the detection volume using the calculated permeation rate constant from the Polonium-214 decay channel and Equation 5.23.

5.5 Summary of Results

A complete summary table of the permeation coefficients calculated in Sections 5.3 and 5.4 can be found in Table 5.4 below. The results obtained from both methods are consistent, falling within the error margins of each measurement.

This study presents two independent determinations of the radon permeation coefficient K_p through a Parker PTFE seal, a parameter not previously reported in the literature. The absence of similar studies on radon permeation through modern, virgin PTFE materials highlights the importance of these two experiments. Consistent results from these measurements strengthen the reliability of the K_p value, which is essential for estimating the radon background resulting from permeation into the PICO-500 active volume. To provide a comprehensive view, Figure 5.19 includes the radon permeation coefficient alongside the coefficients for the lighter mass noble gases, expanding upon the previous Figure 5.15.

Gas	Atomic Diameter (Å)	K_p ($\times 10^{-10} \frac{\text{cm}^3\text{(STP)}\cdot\text{cm}}{\text{s}\cdot\text{cm}^2\cdot\text{cm-Hg}}$)
He*	2.6	26.13 ± 3.44
Ne	2.75	12.44 ± 1.71
Ar	3.4	14.22 ± 3.06
Kr	3.6	8.92 ± 1.72
Xe	3.96	7.90 ± 1.30
Rn	4.57	$5.10^{+0.92}_{-1.10}$ (Extrapolated)
		5.37 ± 0.49 (Measured)

Table 5.4: Complete summary table of the kinetic atomic diameters and the calculated permeation coefficients for all measured noble gases. Kinetic atomic diameters of the noble gases are sourced from [54, 61]. The radon kinetic atomic diameter was sourced from [62].

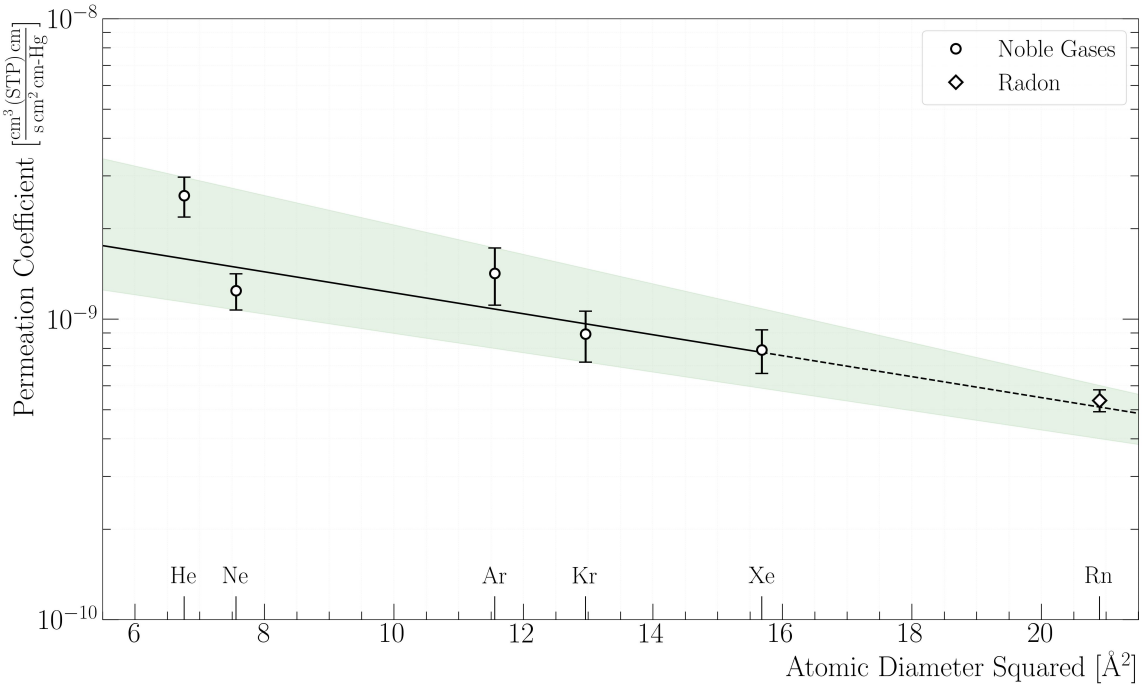

Figure 5.19: Semi-log plot showing the permeation coefficient against the atomic diameter squared for six noble gases, with the best fit line based on the five lower mass gases. The green band represents the fit uncertainty, with the upper limit derived from the maximum best fit of helium and argon, and the lower limit derived from the minimum best fit of neon and krypton.

The noble gas extrapolation method yielded a radon permeation coefficient of $K_p = 5.10^{+0.92}_{-1.10} \times 10^{-10} \frac{\text{cm}^3(\text{STP})\,\text{cm}}{\text{s}\,\text{cm}^2\,\text{cm-Hg}}$, while the direct method resulted in a weighted average radon permeation coefficient of $K_p = 5.37 \pm 0.49 \times 10^{-10} \frac{\text{cm}^3(\text{STP})\,\text{cm}}{\text{s}\,\text{cm}^2\,\text{cm-Hg}}$. Combining both values by taking another weighted average, a radon permeation coefficient of $K_p = 5.32 \pm 0.41 \times 10^{-10} \frac{\text{cm}^3(\text{STP})\,\text{cm}}{\text{s}\,\text{cm}^2\,\text{cm-Hg}}$ was derived by assuming an averaged error of the upper and lower bounds of the first measurement.

5.6 Estimated PICO-500 Background Rate due to Radon Permeation

Minimizing radioactive backgrounds is essential for PICO-500, which is designed to measure ultra-rare events. With the radon permeation coefficient experimentally determined, this value can be applied to estimate the radon activity in the PICO-500 active volume due to permeation. This calculation utilizes the radon permeation coefficient found in Section 5.4 and considers the contribution of the four Parker PTFE seals isolating the active volume of the inner vessel from the pressure vessel.

5.6.1 Calculating the PICO-500 Radon Permeation Rate Constant

The Crystal Plus CP70F mineral oil, selected as the hydraulic fluid for the PICO-500 pressure vessel, was assessed to have an upper bound radon specific activity of 0.4 mBq/kg, determined through gamma emission analysis of Radium-226 in a 450.2 g sample performed at SNOLAB [63]. Based on this upper limit, the total radon emanation rate is estimated to be 3.27 Bq, considering the 18,000 lbs of mineral oil to be used to fill the PICO-500 pressure vessel [64].

The set of coupled differential equations describing the change in radon atoms within the pressure vessel and the active volume of the inner vessel, considering a constant source of radon activity, decay, and permeation, is as follows:

$$\frac{dN_{PV}}{dt} = -r_{\text{perm}} N_{PV} - \lambda N_{PV} + E \tag{5.27}$$

$$\frac{dN_{IV}}{dt} = r_{\text{perm}} N_{PV} - \lambda N_{IV} \tag{5.28}$$

Where N_{PV} is the number of radon atoms in the pressure vessel, N_{IV} is the number of radon atoms in the active volume of the inner vessel, λ is the Radon-222 decay constant, E is the total radon emanation rate of the mineral oil, and r_{perm} is the radon permeation rate constant. Equation 5.27 is solved assuming zero radon activity as an initial condition, yielding the following expression for $N_{PV}(t)$:

$$N_{PV}(t) = \frac{E\left(1 - e^{-(\lambda + r_{\text{perm}})t}\right)}{(\lambda + r_{\text{perm}})} \tag{5.29}$$

To determine the steady-state limit of the radon activity in the pressure vessel, Equation 5.29 is taken to the limit $t \to \infty$, and both sides are multiplied by λ to obtain the radon activity. The result is an expression in terms of rate constants as follows:

$$A_{PV,\text{ Steady State}} = \frac{E \cdot \lambda}{(\lambda + r_{\text{perm}})} \tag{5.30}$$

Equation 5.28 can be solved by substituting the steady-state limit of N_{PV} obtained from Equation 5.29 into Equation 5.28:

$$N_{IV}(t) = \frac{E \cdot r_{\text{perm}}\left(1 - e^{-\lambda t}\right)}{\lambda(\lambda + r_{\text{perm}})} \tag{5.31}$$

Taking the limit as $t \to \infty$ of Equation 5.31 and multiplying both sides by λ to obtain the radon activity yields another expression in terms of rate constants:

$$A_{IV,\text{ Steady State}} = \frac{E \cdot r_{\text{perm}}}{(\lambda + r_{\text{perm}})} \tag{5.32}$$

In the steady-state limit, when the system reaches dynamic equilibrium, the radon activity in the inner vessel due to permeation can be determined using Equation

5.32, provided that the permeation rate constant r_{perm} is known. Since the r_{perm} is a experimental parameter it must be determined numerically in the context of the system being investigated. Equation 5.26 can be explicitly expressed as a function of r_{perm} within the context of PICO-500 in the steady-state limit:

$$K_p(r_{perm}) = \frac{l}{S}\frac{r_{perm}\cdot E}{T}\left(\frac{T_{STP}}{P_{STP}}\right)\left[\frac{E\cdot\lambda}{(\lambda+r_{perm})}\frac{1}{V_{PV}} - \frac{E\cdot r_{perm}}{(\lambda+r_{perm}}\right)\frac{1}{V_{IV}}\Bigg]^{-1} \tag{5.33}$$

Four physical parameters differ between the UofA experimental setup and PICO-500: the temperature of the radon gas T (-40°C), the radon origin volume V_{PV} (8830 litres [64]), the radon permeation volume V_{IV} (500 litres [64]), and the active permeation surface area S of the seal (155.62 cm^2). Since the only unknown in this equation is r_{perm}, a numerical root-finding algorithm can be applied to Equation 5.33 to solve for r_{perm} when Equation 5.33 takes the following form:

$$f(r_{perm}) = \frac{l}{S}\frac{r_{perm}\cdot E}{T}\left(\frac{T_{STP}}{P_{STP}}\right)\left[\frac{E\cdot\lambda}{(\lambda+r_{perm})}\frac{1}{V_{PV}} - \frac{E\cdot r_{perm}}{(\lambda+r_{perm}}\right)\frac{1}{V_{IV}}\Bigg]^{-1} - K_p \tag{5.34}$$

Using the `fsolve` function from the `scipy` library in Python, the permeation rate constant r_{perm} was found to be $6.8\times10^{-12}\,\text{s}^{-1}$. Substituting this value into Equation 5.32, the radon activity is calculated to be 0.9 Radons/Day for one PTFE seal. Accounting for all four PTFE seals, the total radon activity due to permeation is estimated to be 3.7 Radons/Day. It's important to note that the parameters for all seals were considered constant, despite a minor geometric difference in one of the seals.

As a comparison, the radon emanation rate from eight elastomer seals tested in PICO-40L was reported to be 134.55 ± 4.91 Radons/day [65]. In contrast, the radon emanation rate for a single Parker PTFE seal, measured at Queen's University (see Appendix A), was found to be 6.39 ± 12.16 Radons/day. This results in a total radon rate contribution of approximately 7.6 Radons/day for one PTFE seal in PICO-

500, representing a 55% reduction compared to one PICO-40L elastomer seal. By accounting for the emanation rate and permeation rate of all four PTFE seals, a total radon rate was calculated to be 30.5 Radons/Day. This results highlights the effectiveness of the Parker PTFE seals as low radon background contributors in this type of environment.

5.6.2 Implications for PICO-500 and Beyond

Determining the permeation coefficient K_p and the permeation rate constant r_{perm} for the Parker PTFE seal is crucial for the success of future dark matter search experiments and ultra-low background detectors that incorporate or will incorporate PTFE seals within their detection volumes. This research not only addresses a gap in the existing literature but also lays the groundwork for future studies, particularly those exploring the temperature dependency of the permeation coefficient, an aspect not investigated in this thesis. Given that the temperature-dependent permeation coefficient is expected to follow the Arrhenius equation, it is anticipated that at the operational temperatures of $-40°$C to $-50°$C in PICO-500, the true permeation coefficient—and thus the true radon permeation rate—will be lower than what has been reported here. Moreover, it's known that radon transport through liquids has significantly lower diffusion coefficients compared to transport in gases [66]. If the diffusion time is on the order of the Radon-222 half-life, it could potentially reduce the amount of radon activity in the inner volume. Consequently, the values presented here represent an upper limit for the radon permeation coefficient and permeation rate with respect to PICO-500.

The assessment of the radon permeation coefficient through the Parker PTFE seal, conducted via two independent methods, provides insights into the performance of the seal against radon transport. The evident lack of comprehensive studies on this subject as a whole highlights an area in need of further exploration and the creation of standardized methods for testing radon permeation rates.

Chapter 6

PICO-500 Quartz Vessel Cleaning

6.1 Introduction

The first run of PICO-60, which used a CF_3I target, demonstrated the need for the implementation of cleaning procedures for the quartz vessels prior to detector assembly. Anomalous events were observed, which mimicked a WIMP signal in the acoustic detection system [67]. However, these anomalous events consistently occurred after an expansion of the detector, which goes against the expectation of a constant WIMP signal in time, and had higher event rates near the walls and the Freon-water buffer [67]. An investigation into particulate contamination within the inner vessel of the PICO-60 detector revealed significant levels of dust and other particulates [67]. This led to the adoption of specialized cleaning procedures aimed at comprehensively removing all types of particulates. The implementation of these procedures, coupled with detailed sample analysis, was essential in achieving an anomaly-free background in the second run of PICO-60 [67]. This chapter outlines effective strategies for the removal of particulates and dust from quartz vessel surfaces. Building upon and refining methods previously used in PICO-60 and PICO-40L, a cleaning protocol for both the inner and outer surfaces of the PICO-500 quartz vessels was developed. This protocol aims to meet the IEST-STD-CC1246D-25 standard, which specifies cleanliness levels for various particulate size bins [68].

6.2 Cleaning Cart

The PICO-500 cleaning cart, referred to as the PICO-500 Dishwasher [69], is engineered to circulate, filter, and heat cleaning fluid and is equipped with two Sandpiper air-operated double diaphragm (AODD) pumps, a Blacoh pulsation dampener to dampen fluid pressure oscillations, and dual 20" filter housings with 0.05-micron TefTec PTFE membrane cartridges [70]. It also features two Omega heater tapes wrapped around a stainless steel PTFE lined flex hose to increase fluid temperature to improve soap activation, along with pressure and temperature sensors, and a pH sensor to verify the rinsing process. Inline water temperatures were found to stabilize at 30°C from the external heating. Control and data acquisition are facilitated by a National Instruments Compact Fieldpoint I/O, which interfaces with a LabVIEW program. The plumbing utilizes Chlorinated-PVC (CPVC) for its high temperature tolerance and vast chemical compatibility, ensuring that all wetted components are plastic to prevent the possibility of metallic deposition on the quartz surfaces. This allows the ability to use 20% nitric acid, which is a strong oxidizing acid that can dissolve metals, making it effective for removing metal ion deposits from quartz surfaces if necessary.

Additionally, for operator safety, the cleaning cart is fully enclosed with acrylic panels utilizing the 8020 aluminum extrusion frame slots, and all hand-operated valves can be actuated from the top of the cart. The inside of the cart can be accessed from two panel doors for maintenance and sample taking.

A Piping and Instrumentation Diagram, along with a labelled CAD model of the PICO-500 dishwasher, are shown in Figures 6.1 and 6.2, respectively.

6.2.1 Cleaning DAQ Software Overview

A LabVIEW program developed for the cleaning procedures provides user control over the cleaning cart via a graphical interface (Figures 6.3 and 6.4). It manages the com-

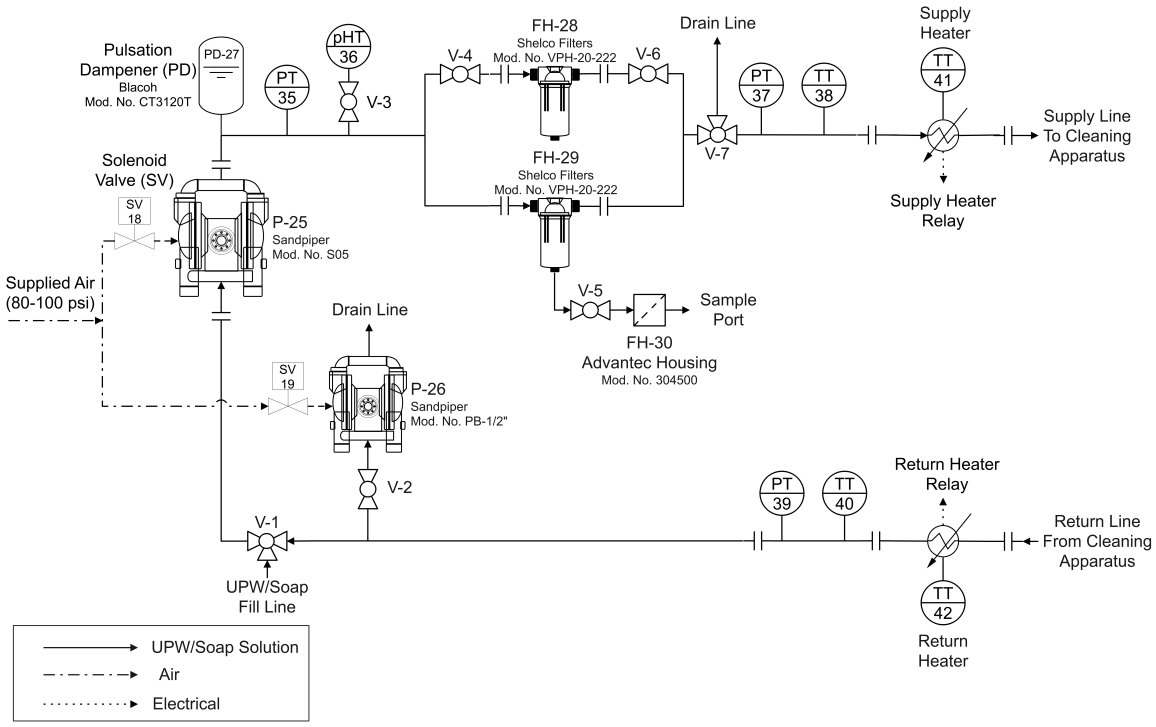

Figure 6.1: Piping and Instrumentation Diagram of the cleaning cart (Dishwasher) used for cleaning the PICO-500 quartz vessels.

pressed air input to operate the diaphragm pumps, which are regulated by normally closed solenoid valves, and also controls the heater tapes via two relay switches. The program includes fail-safes for unsupervised operations, such as automatic shutdown for detected leaks by monitoring average pressures, and thermal runaway protection to prevent heater tape temperatures from exceeding 180°C. Users can choose between two modes: 'manual' for tasks that involve filling, draining, sample taking, and general testing; and 'circulation' for automatic operation of the pump and heater tapes with the aforementioned built-in fail-safes.

The program also saves the data of the pressure, temperature, and pH readings into an Excel file for further analysis. Remote viewing is possible through a webcam feed, allowing oversight of difficult to access areas. User inputs and switch activations are logged into a separate Excel file, providing detailed documentation of operations.

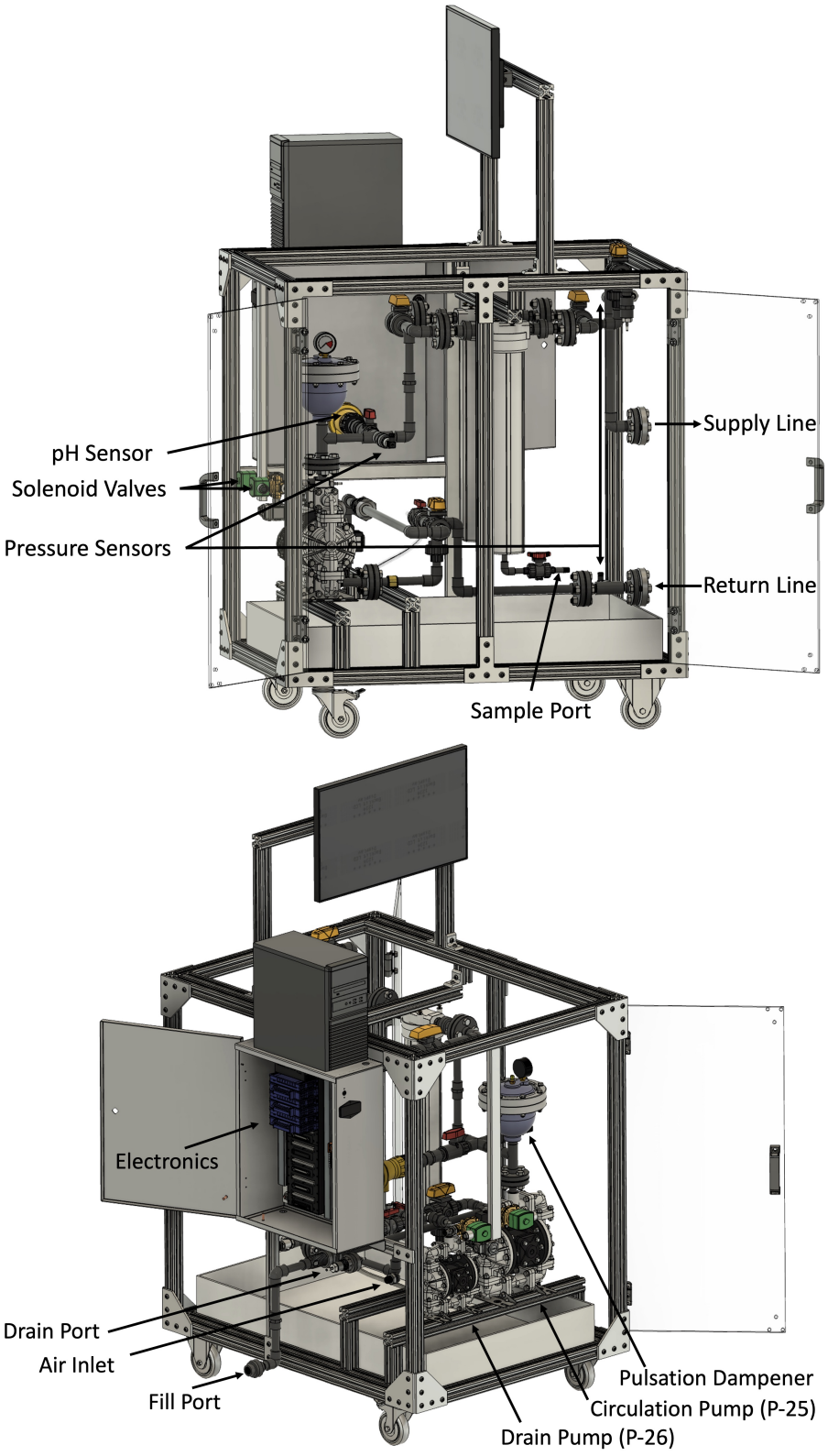

Figure 6.2: Labelled CAD model of the PICO-500 Dishwasher.

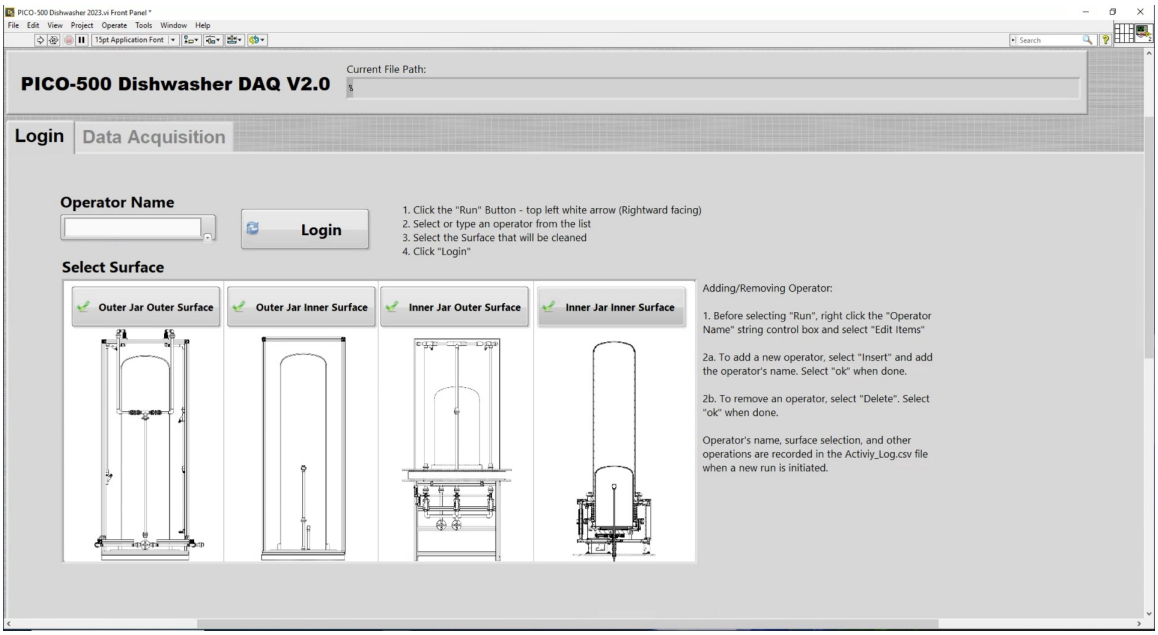

Figure 6.3: PICO-500 Dishwasher DAQ V2.0 interface (Part 1): Users log in by selecting their name and the surface to be cleaned.

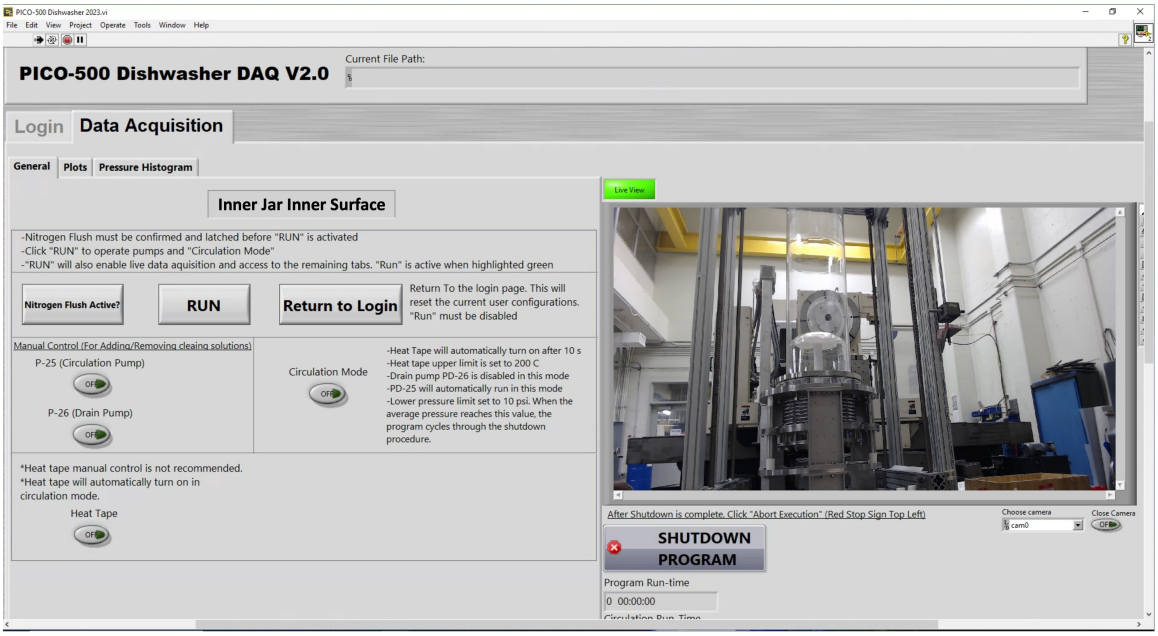

Figure 6.4: PICO-500 Dishwasher DAQ V2.0 Interface (Part 2): This tab enables users to control system components, including pumps and heaters, and to monitor sensor data through the 'Plots' tab menu.

6.3 Standard Cleaning Procedures

To establish a baseline for cleanliness, the cleaning system, defined as the PICO-500 Dishwasher and the surface cleaning setup, circulates UPW for a 24-hour period before the introduction of Alconox. This baseline assessment allowed for monitoring the level of cleanliness and the reduction of particulates over time. For uniform cleaning of all surfaces, a solution of 0.08-0.1 grams of Alconox per liter of UPW was used, which represents the highest concentration that avoids excessive foaming and has a typical pH range of 8.0-8.9. The quartz vessels were cleaned with this solution for 1-2 days. Following this cleaning cycle, the system was thoroughly flushed with UPW until the pH sensor readings aligned with the UofA's UPW water supply line, which has a pH range of 6.0-6.5, and until no visual signs of detergent residue were present. Figure 6.5 shows the soap flushing process from a cleaning test run. The flushing involved intermittent 10 minute circulations to ensure thorough mixing and dilution of the UPW and Alconox solution. After the detergent was removed, the system circulated UPW for an additional 1-2 hours before a sample was collected, with a second sample taken after another 1-2 hours of circulation.

To address potential radon contamination during cleaning, mitigation strategies are implemented for each surface, typically by maintaining a slight positive pressure of nitrogen gas at 8 psi to flush the lab air from the cleaning setup volume or employing a vacuum where possible. Detailed mitigation techniques for each surface are provided in their respective sections.

Nitrogen gas drying procedures follow the cleaning steps and is a continuation of the nitrogen gas purging. Typically, drying periods with nitrogen last up to 24 hours, as determined by visual inspection of the drying progress.

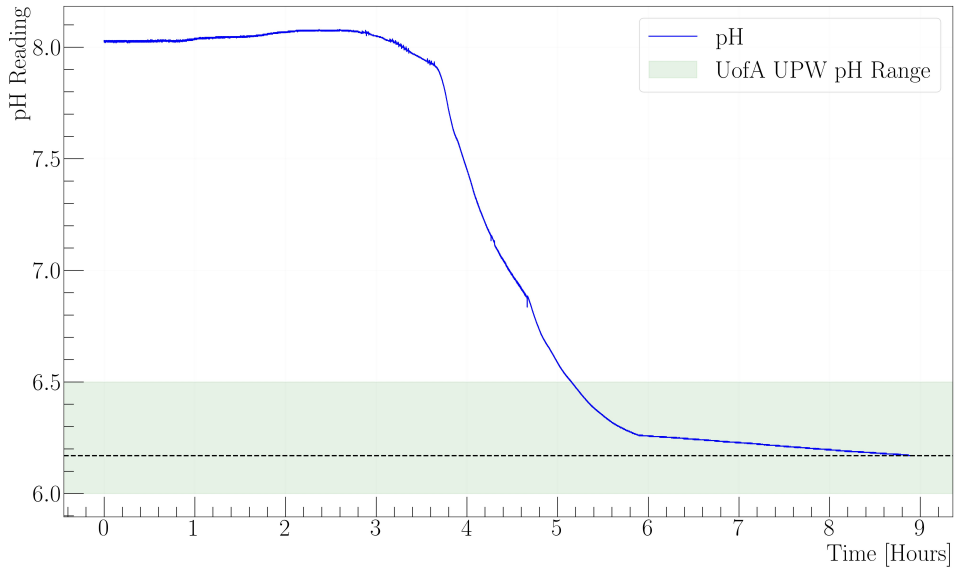

Figure 6.5: Change in pH levels during a UPW flushing after a soap cleaning cycle using Alconox. The black horizontal line indicates the pH stabilization point.

6.3.1 Outer Quartz Vessel

Outside Surface

The outer quartz vessel cleaning setup for the outer surface includes two 120° and two 60° fulljet spray nozzles for comprehensive coverage of one quadrant of the outer quartz vessel. A Piping and Instrumentation Diagram, along with a labelled CAD model of the cleaning setup are shown in Figures 6.6 and 6.7. The vessel is sealed against an HDPE base plate using an HDPE split flange, M10 bolts torqued to 96 in-oz, and a 1/4" Viton O-ring. The nozzles are strategically placed along two adjacent corners to optimize spray reach and pressure. For complete vessel cleaning, the enclosure must be manually lifted and rotated to cover all quadrants sequentially. Additional plumbing at the base of the enclosure enables supply line connection points on each side. The two spray nozzle lines can operate both together and independently, a feature adapted from observing varied pressure levels during tests: dual-line operation reaches up to 34 psi, while a single line achieves 48 psi. The manufacturer recommends maintaining a target pressure between 20-80 psi per nozzle to achieve the specified spray angle [71].

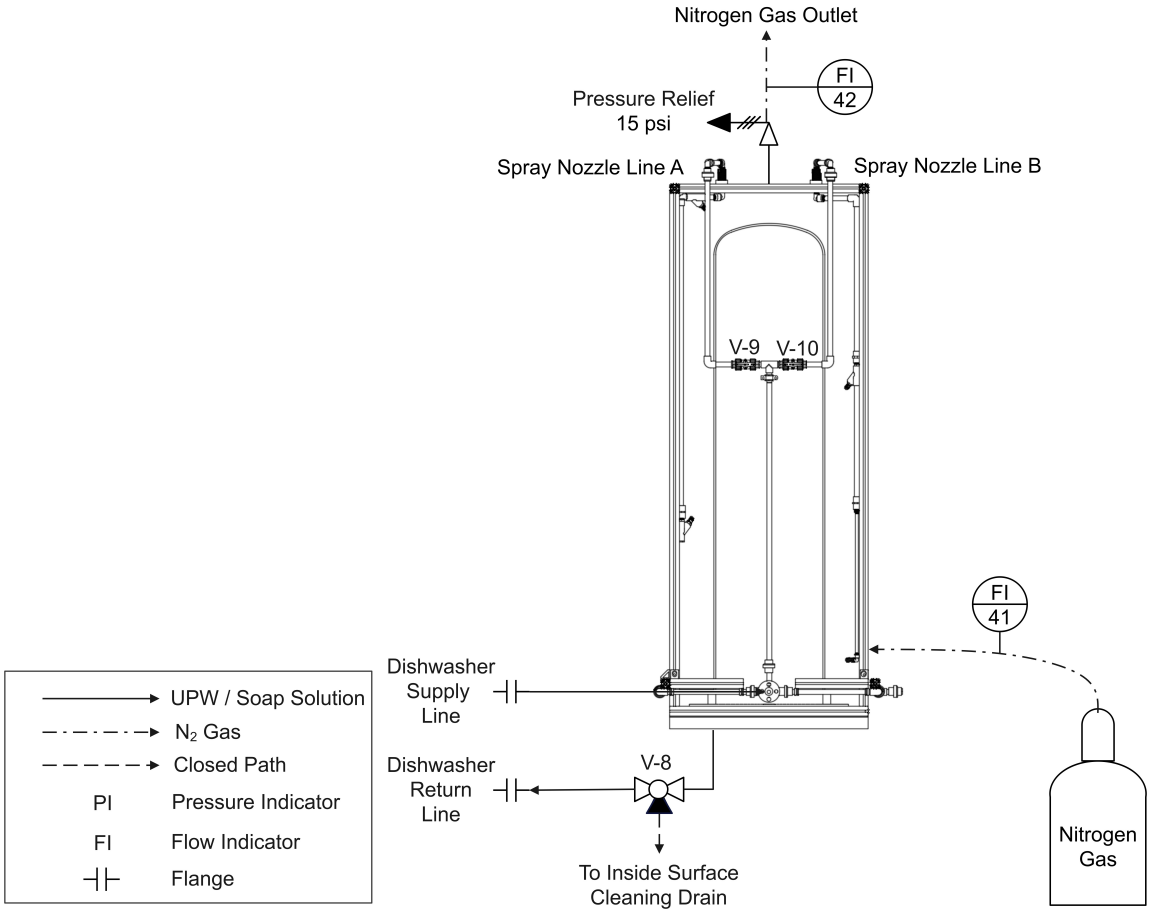

Figure 6.6: Piping and Instrumentation Diagram of the cleaning setup for the outside surface of the outer quartz vessel.

A 1/4" PTFE tube functions as the nitrogen gas inlet and includes a flow indicator. The top of the enclosure features a 1/2" diameter opening designated as the nitrogen gas outlet, fitted with a 15 psi pressure relief valve and a flow indicator. The larger size of this opening is critical to prevent internal pressurization.

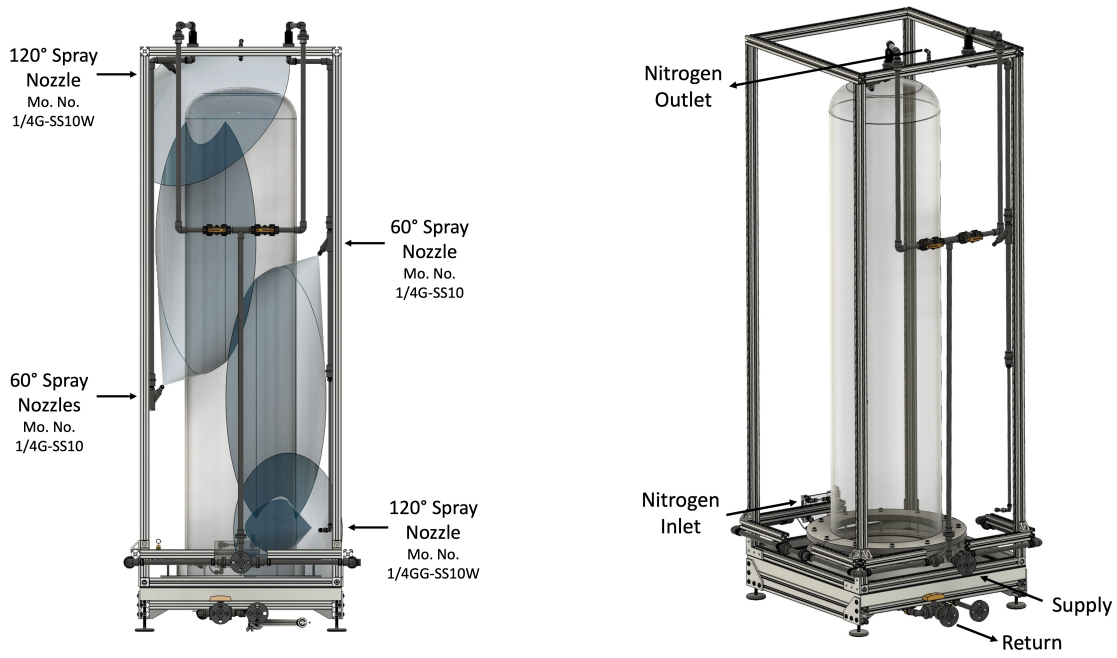

Figure 6.7: CAD model showing the outer surface cleaning setup of the outer quartz vessel, demonstrating the spray pattern and flow processes.

Inside Surface

The cleaning process for the inner surface of the outer quartz vessel uses the same cleaning setup as that of the outer surface. However, the supply line from the dishwasher connects to the inlet of the inner cleaning connection, and the orientation of valve V-8 (Figure 6.8) is changed to pump from the drain used for inside cleaning. The system features a self-propelling PTFE 360° Tankjet spray nozzle [72], which is centrally positioned inside the quartz vessel and capable of reaching 35 psi during normal operations.

This system uses positive nitrogen gas pressure to displace ambient lab air, utilizing a coaxial line configuration that combines a 1/4" PTFE hose within a 1/2" CPVC pipe inside the cleaning setup. This configuration adapts to a KF-25 vacuum line on the outer connection. A modified KF-25-to-1/4" compression fitting adapter allows the PTFE hose to be coaxial while ensuring a seal through the compression of the Swagelok fitting ferrules. Nitrogen gas exits through a KF-25 tee port, with a 15 psi pressure relief valve attached to prevent system overpressurization. A labelled CAD

model of this cleaning setup is shown in Figure 6.9.

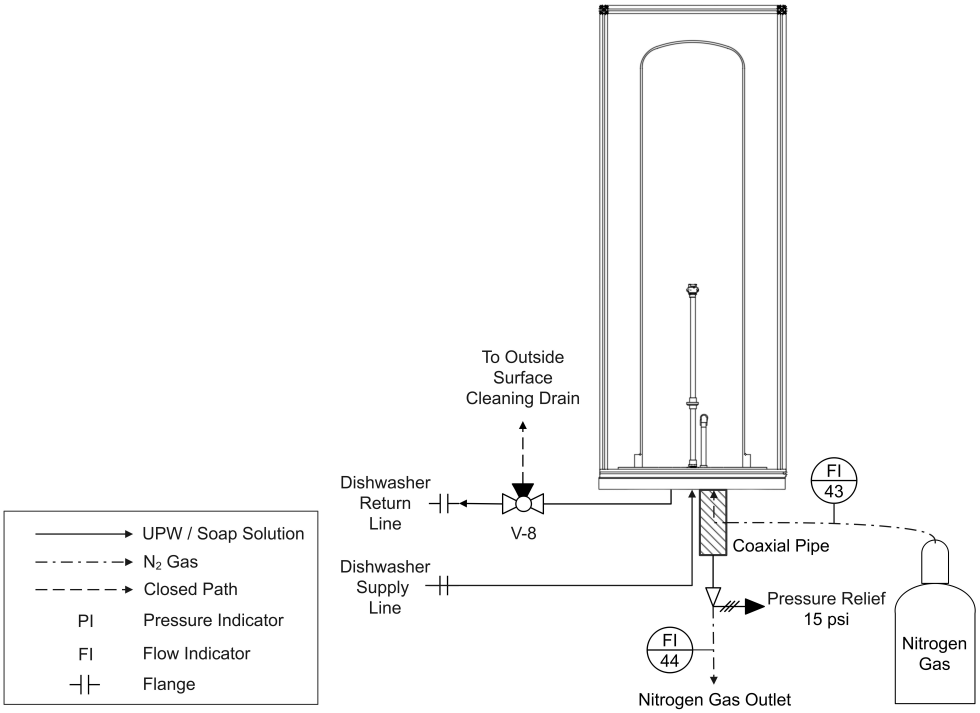

Figure 6.8: Piping and Instrumentation Diagram of the inside surface cleaning of the outer quartz vessel.

6.3.2 Inner Quartz Vessel

Outside Surface

The cleaning setup for the outer surface of the inner quartz vessel includes three PVDF nozzles, each with a 120° spray angle, arranged in a circular formation above the vessel. To minimize unnecessary contact with this active target surface, flange connections were omitted. Instead, the inner volume of the quartz vessel is subjected to a vacuum, compressing a 1/4" Viton O-ring between the vessel and the HDPE base plate. This effect is achieved with an acrylic vacuum plate that seals against the bottom of the base plate also using a 1/4" Viton O-ring. Equipped with a vacuum gauge and valve, the vacuum plate allows for monitoring and maintaining the vacuum seal without the continuous operation of the vacuum pump. The evacuation of the inner volume also serves as a radon mitigation step by preventing ambient radon

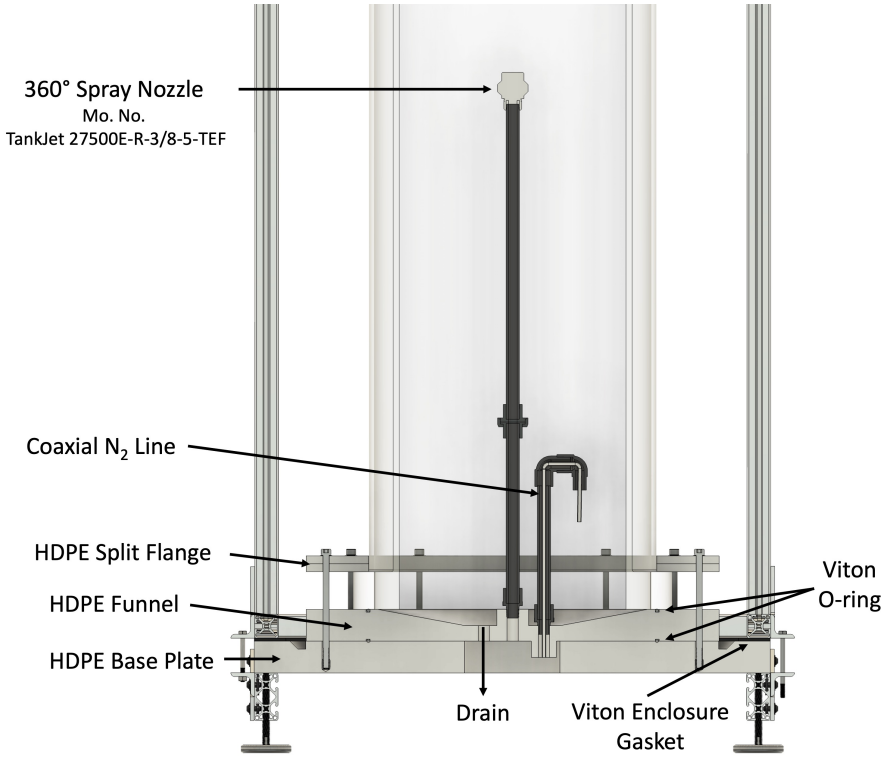

Figure 6.9: Labelled CAD model of the outer quartz vessel cleaning setup.

exposure. Additionally, the system is enclosed using a standard HDPE tank modified with a custom hot-gas-welded HDPE flange to act as an enclosure. A 4-way split aluminum top flange is placed on top of the HDPE flange to prevent deformation during the sealing phase. This enclosure is sealed against the HDPE base plate with an in-house-made 871 mm diameter Viton O-ring and fastened to an aluminum base flange with twenty-four 1/2" bolts. Empirical testing determined that the minimum required torque to seal the enclosure effectively is 50 in-lbs.

Initial tests revealed that activating all three spray nozzles simultaneously failed to achieve the necessary pressure for effective cleaning. The pressure of the system averaged only 7 psi, which was deemed poor in terms of performance [71]. Furthermore, a nitrogen flush system was necessary to facilitate proper radon mitigation. To address these concerns, a manifold was designed with six 3-way valves and incorporated into the setup, allowing one nozzle to be operated at a time for cleaning, while repurposing the remaining two nozzle lines for nitrogen gas inflow and outflow. Oper-

ating one nozzle increased the system pressure to an average of 35 psi. Both nitrogen gas lines are outfitted with flow indicators, and a 15 psi pressure relief valve was installed on the outflow line. Figure 6.10 illustrates the Piping and Instrumentation Diagram for each operational mode. Alternating among these configurations ensures both comprehensive cleaning of the inner quartz vessel and effective radon mitigation. Figures 6.11 and 6.12 both display labelled CAD models illustrating spray angles and referenced components.

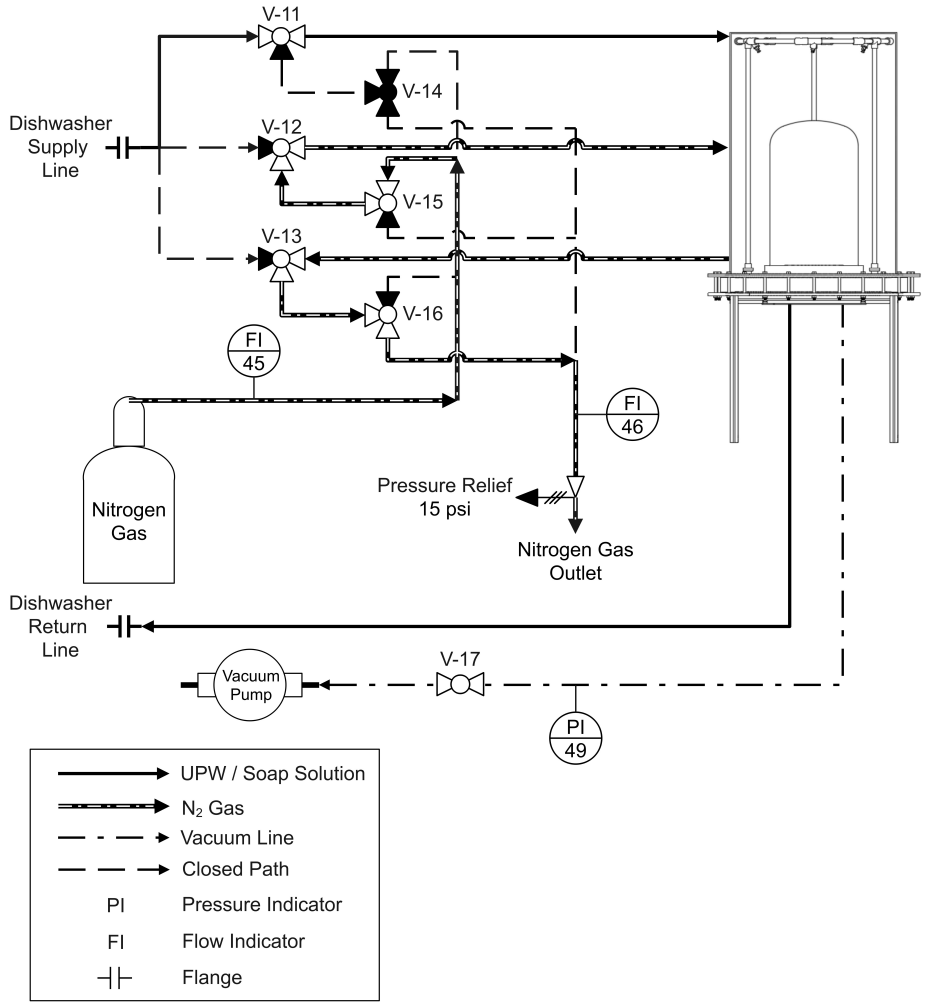

Figure 6.10: Piping and Instrumentation Diagram of the outer surface cleaning of the inner quartz vessel (Orientation 1).

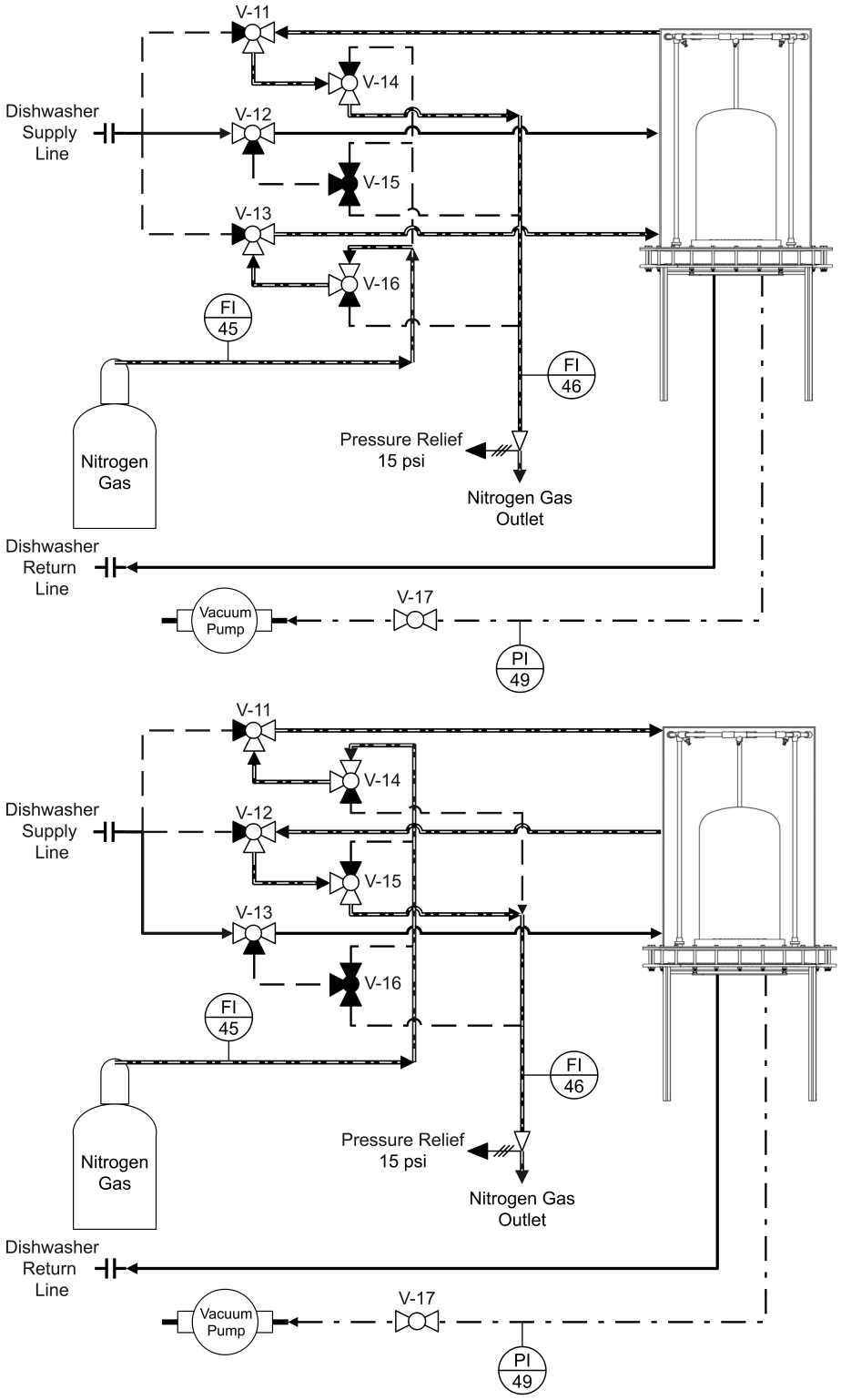

Figure 6.10: Piping and Instrumentation Diagram of the outer surface cleaning of the inner quartz vessel (Orientations 2 and 3).

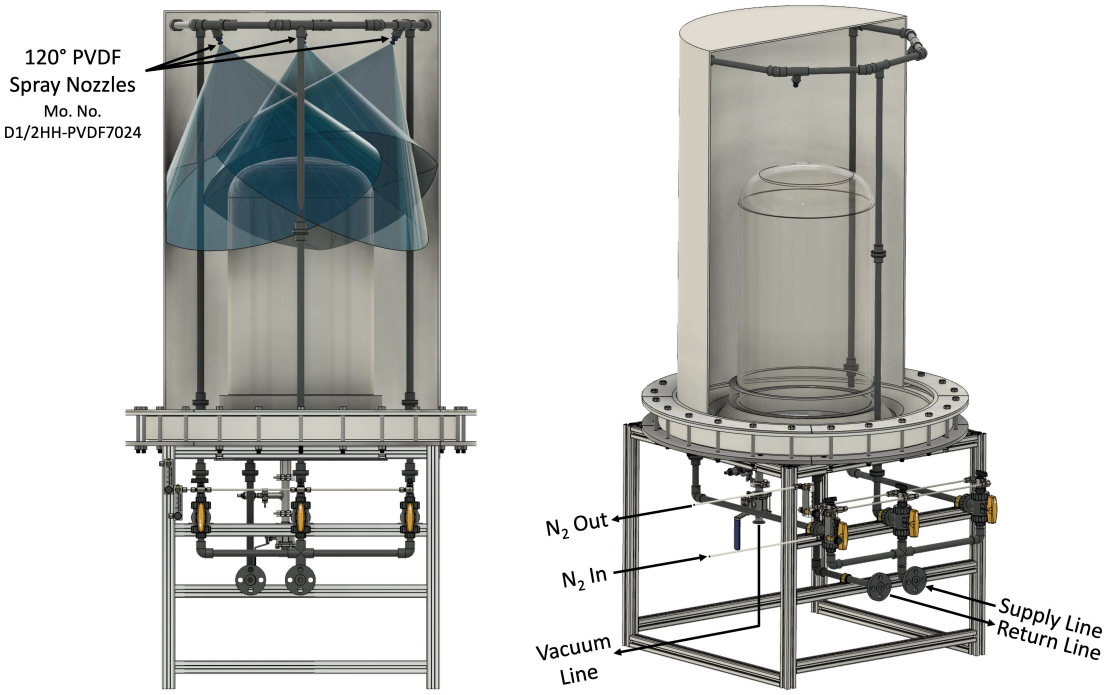

Figure 6.11: CAD model of the inner quartz vessel cleaning setup of the outer surface showing spray angles and flow processes.

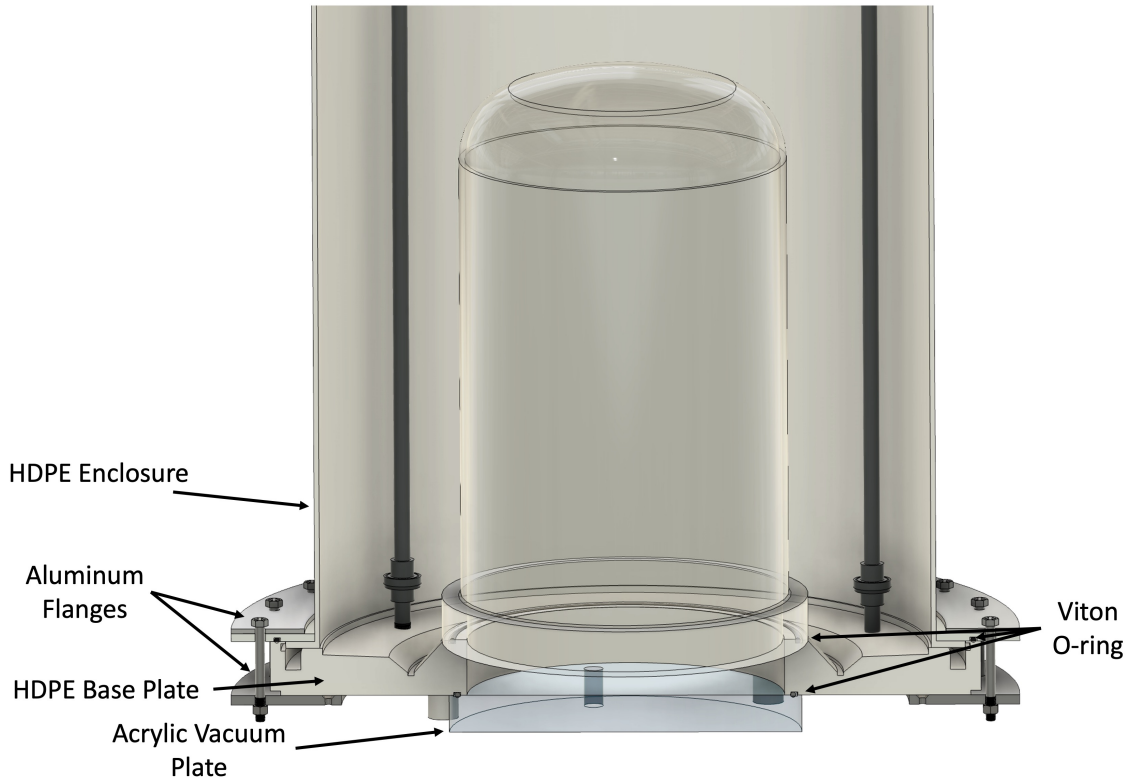

Figure 6.12: Labelled CAD model of the outer surface cleaning setup for the inner quartz vessel, highlighting the cleaning system components.

Inside Surface

The inner surface of the inner quartz vessel is set to be cleaned during the inner vessel (IV) assembly, utilizing a custom HDPE flange that interfaces with an acrylic cleaning plate, originally designed for PICO-40L cleaning procedures. A Piping and Instrumentation Diagram is shown in Figure 6.13. A centrally positioned inlet line to the 360° spray nozzle is coaxial to the drain line as shown in Figure 6.14. Additionally, the design incorporates a coaxial nitrogen gas feed and outlet system, featuring a 15 psi pressure relief valve on the outlet, mirroring the technique used for radon mitigation on the inner surface of the outer vessel.

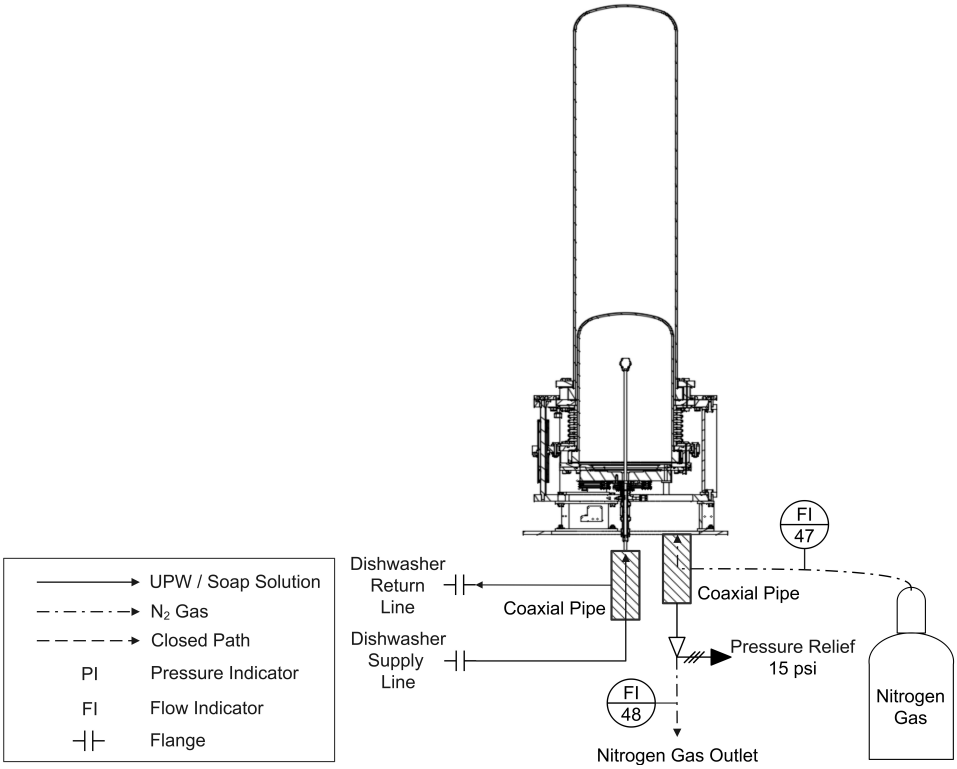

Figure 6.13: Piping and Instrumentation Diagram of the inner quartz vessel cleaning setup on the inner vessel assembly table.

Although only limited testing was performed at the University of Alberta of this setup, the implementation of a 360° PTFE Tankjet spray nozzle is expected to achieve pressure levels sufficient for comprehensive cleaning based on the results from the inner surface of the outer quartz vessel.

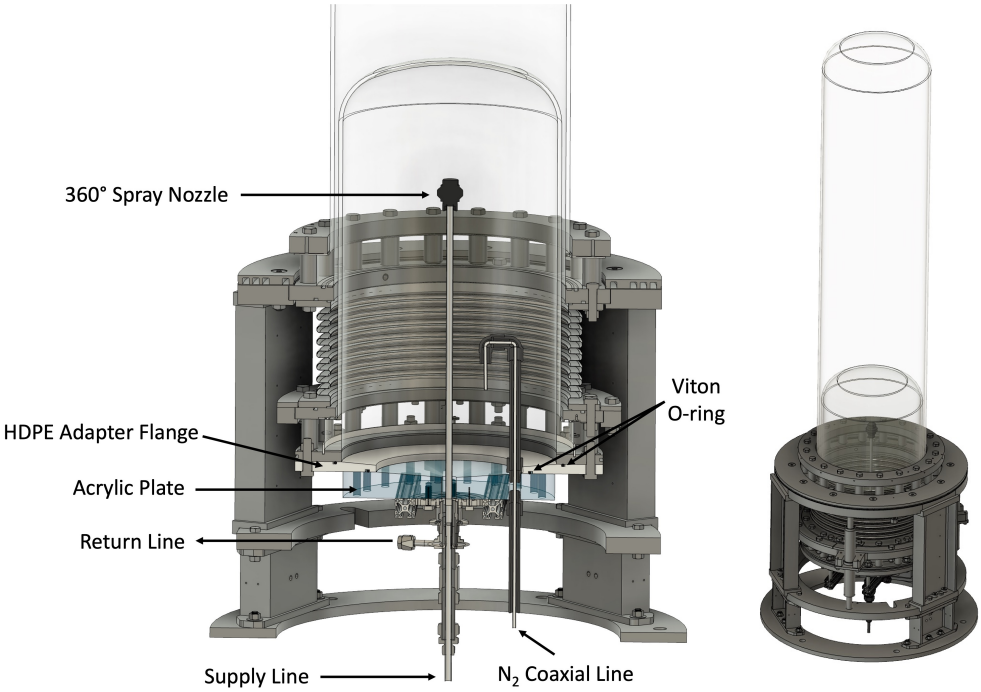

Figure 6.14: Labelled CAD model illustrating the cleaning setup for the inner surface of the inner quartz vessel during the detector assembly.

6.4 Sampling Procedure

The initial step in the sampling procedure involves disconnecting and removing the primary filter housing from the PICO-500 Dishwasher at the CPVC threaded unions. Additionally, there is a provision for the removal and cleaning of the secondary filter housing after every other sample. To avoid contamination from external sources, double-gloving procedures and measures to minimize exposure to lab air are implemented. Threaded union caps are installed on the main lines and the filter housing lines during disassembly as a first step to maintain minimal exposure. The filter housing is only opened at a UPW source to allow for thorough rinsing of both the housing and the filter cartridge, specifically targeting settled particulates that could inaccurately indicate a lower water cleanliness level, thereby potentially skewing the results. After reinstalling the filter housing, the system is set to circulate UPW, with 1-2 litres of water purged through the sample port to eliminate any remaining settled particulates. Water sampling for particulates is conducted using an Advantec filter

housing, equipped with a 0.2-micron, 25 mm diameter PTFE hydrophilic membrane filter. The subsequent installation of the Advantec housing and the passage of one liter of UPW through the sample filter, while circulating, ensures that the filtered water accurately represents the true suspended particulate size and count distribution (Figure 6.15).

Figure 6.15: Sampling the UPW after a cleaning cycle of the outer quartz vessel.

For sample retrieval, the Advantec housing must be completely dismantled within a clean room while following clean room protocols (Figure 6.16). The sample is then carefully placed in a petri dish using clean, sterile tweezers, and sealed in a plastic sealable bag for a 24-hour drying period. The procedure also includes rinsing the Advantec housing and components with UPW before installing a new filter sample and storing it in a protective bag when not in use.

6.5 Sample Analysis and Results

Sample Analysis

The analysis of the sample is conducted using a microscope to image the hydrophilic PTFE membrane filter. Figure 6.17 displays an optical image of a filter used during the testing phase for cleaning the outer surface of the outer quartz vessel, captured at 10x magnification. The image reveals small particulates, the origins and compo-

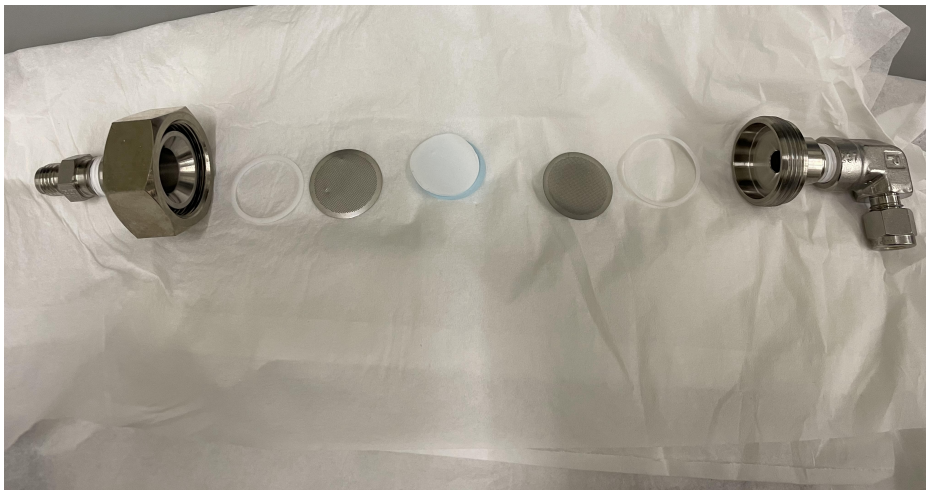

Figure 6.16: Dismantled Advantec filter housing.

sition of which remain unidentified. To ensure a comprehensive analysis, 45-50 non-overlapping images are captured, covering $\geq 10\%$ of the filter area. Overlaps between images are avoided by shifting each subsequent image 1.2 mm in the x-axis and 0.8 mm in the y-axis when near the edge of the filter. The set of images is analyzed using a image processing script in Matlab, which quantifies the particulate size (measured along the longest axis) and count through image analysis techniques. The analysis aims to compare the particulate concentration distribution against three IEST standards: IEST-STD-CC1246D-25, IEST-STD-CC1246D-50, and IEST-STD-CC1246D-100, with the goal of meeting the requirements set by the IEST-STD-CC1246D-25 standard, as illustrated in Figures 6.18, 6.19, and 6.20. Due to time constraints, a complete cleaning operation and sampling of the inner surface of the inner quartz vessel was not conducted.

Results

Particulate concentration within the IEST-STD-CC1246D-25 standard range was typically achieved within a 5 to 7 day continuous cleaning run. It is noted that the absence of nitrogen purging systems, inconsistent heating periods, supplied UPW that was of sub-optimal quality, and operations performed in a non-clean room environ-

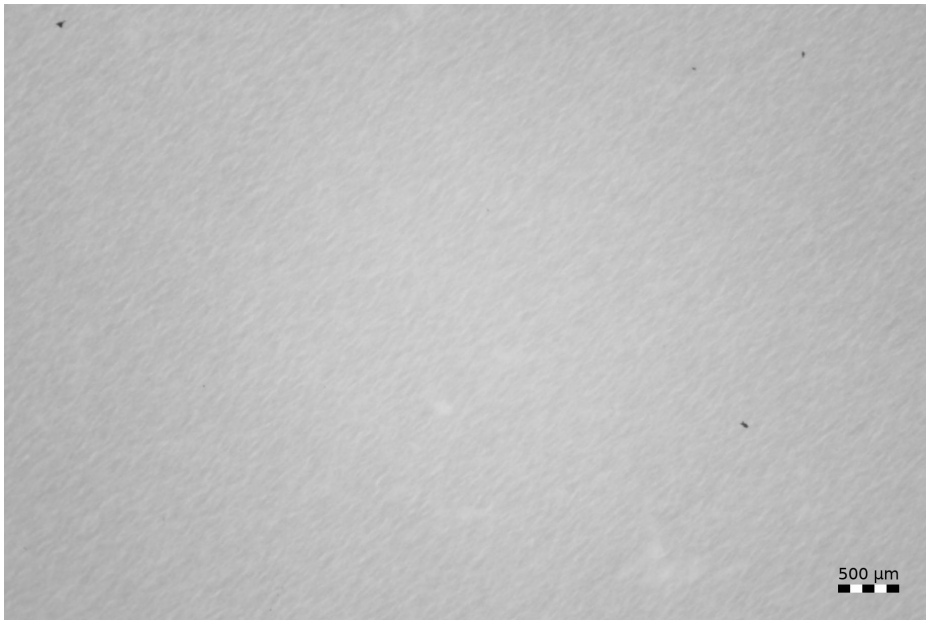

Figure 6.17: Microscopic image at 10x magnification of a section from sample EP-280823-OJOS-1, revealing particulates of unknown composition and origin.

ment during these runs were factors that directly impacted the results. These issues, along with variations in sample-taking techniques, led to differences in the particulate concentration distributions. However, meeting the IEST-STD-CC1246D-25 standard was still achieved through the application of proper sampling techniques.

As a demonstration of particulate reduction over time, the sample filter area-corrected total particulate concentration was calculated for each sample. The data of the outer vessel inside surface and outside surface were modelled with a generalized exponential decay function:

$$C(t) = C_R + (C_0 - C_R)\, e^{-\frac{t}{\tau}} \tag{6.1}$$

Where $C(t)$ represents the total particulate concentration at time t, C_R is the residual particulate concentration, C_0 is the initial particulate concentration, and τ is the time constant.

Figure 6.21 shows the results for the inner surface of the outer quartz vessel after operating the cleaning system for 21 days, with intermittent stops for sample col-

lection. The variability in the results is attributed to experimentation with different sample collection techniques. Notably, implementing stringent and consistent sample collection measures (Section 6.4) for the outer surface of the outer quartz vessel led to significant improvements in the results, as shown in Figure 6.22. The outlier observed on day 3, was a result from a leak in the Advantec filter housing due to a warped O-ring. For the second measurement that day, the O-ring was replaced, proper sampling procedures were followed, and the results remained consistent with particulate reduction over time.

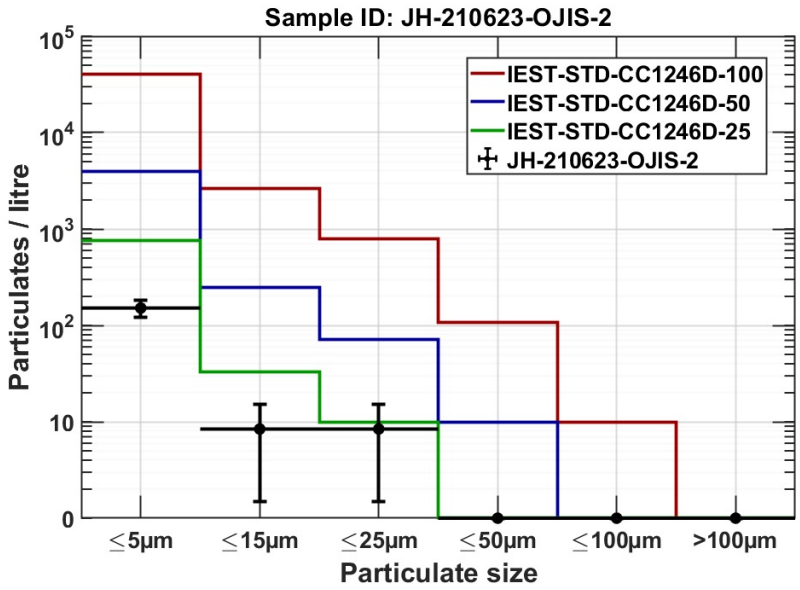

Figure 6.18: Particulate concentration on the inner surface of the outer quartz vessel after 15 days of continuous cleaning. Results agree with the IEST-STD-CC1246D-25 standard. Error bars of each bin represent the 90% confidence interval.

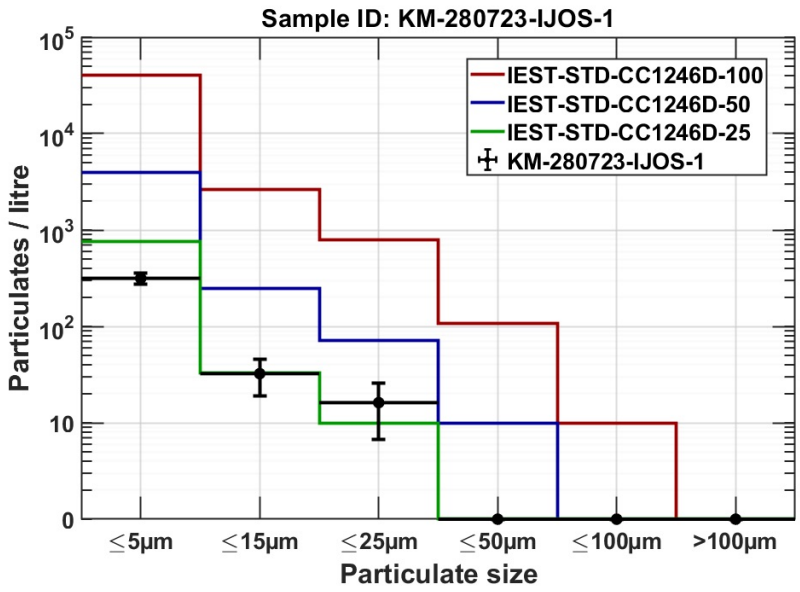

Figure 6.19: Particulate concentration on the outer surface of the inner quartz vessel after a 7 day period of continuous cleaning. Results agree within error of the IEST-STD-CC1246D-25 standard. Error bars of each bin represent the 90% confidence interval.

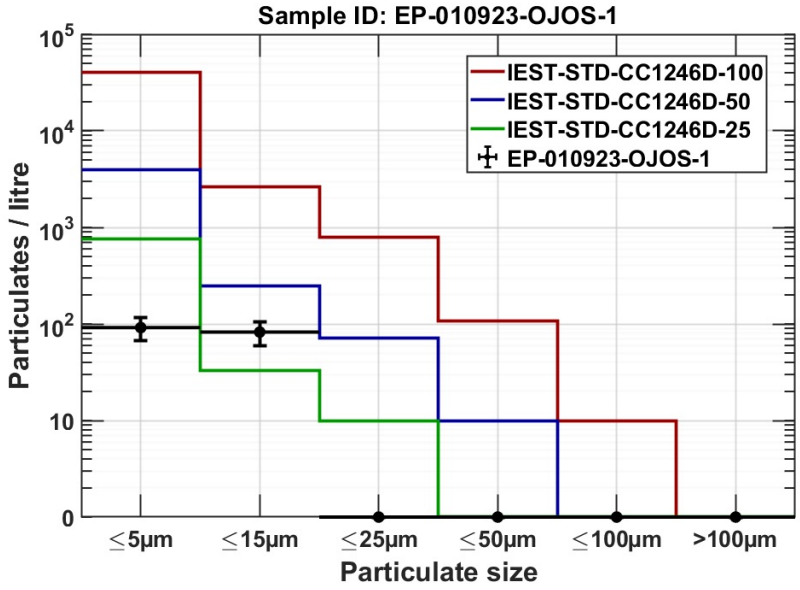

Figure 6.20: After a continuous 5 day cleaning period, the particulate concentration on the outer surface of the outer quartz vessel still exceeded the IEST-STD-CC1246D-25 standard in the 15 µm size bin. Additional cleaning time is necessary to effectively reduce particulates in this bin. Error bars of each bin represent the 90% confidence interval.

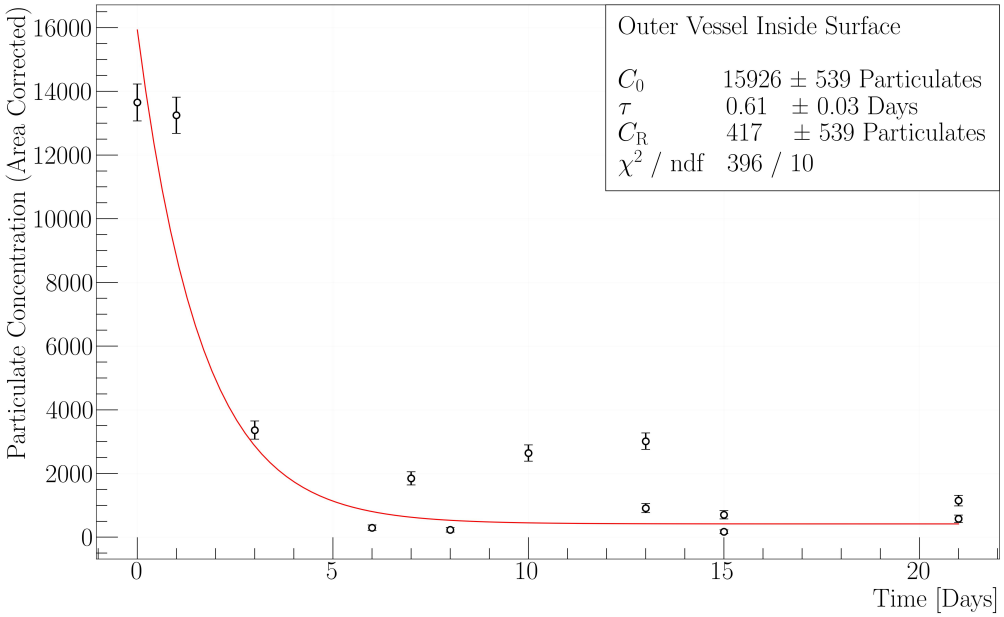

Figure 6.21: Particulate reduction of the inner surface of the outer quartz vessel during a 21 day cleaning test. Error bars represent the 90% confidence intervals for the total particulate counts.

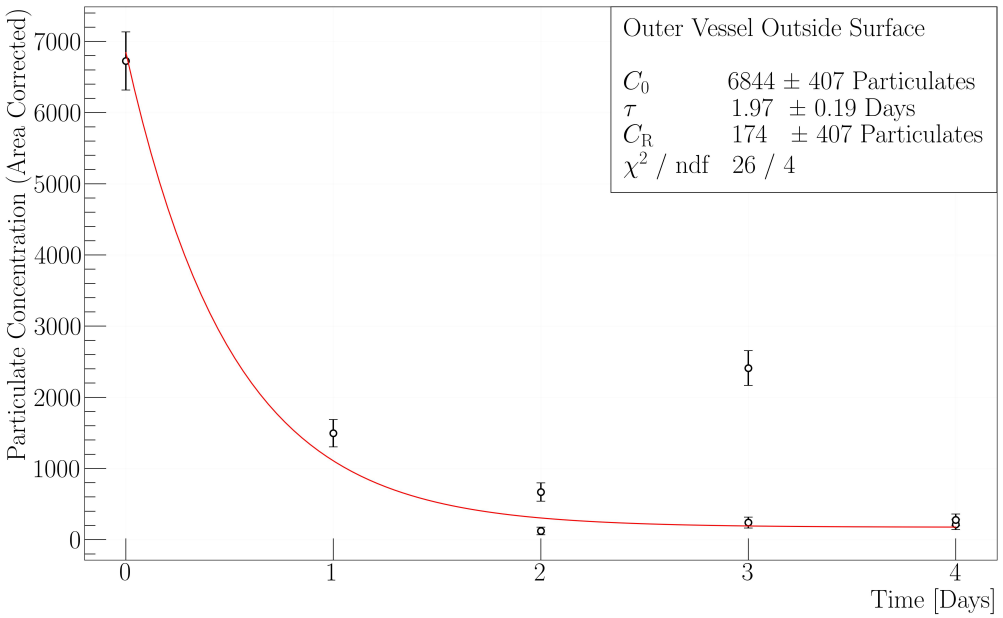

Figure 6.22: Particulate reduction of the inner surface of the outer quartz vessel during a 5 day cleaning test. Error bars represent the 90% confidence intervals for the total particulate counts.

6.6 Summary

In order to achieve anomalous-free backgrounds in PICO-500, proper cleaning procedures must be implemented. Meeting the IEST-STD-CC1246D-25 standard necessitated the development and testing of custom cleaning systems, focusing on sufficient cleaning fluid pressure for particulate removal, as well as system isolation and radon mitigation to avoid airborne contamination during extended cleaning sessions in SNOLAB. Additionally, sampling techniques were refined to ensure minimal contamination from settled particulates in the sampling line by removing and cleaning the filter housings before each sample. While the cleanliness levels of the labs at the University of Alberta prevented consistently reaching IEST-STD-CC1246D-25, it was demonstrated that reaching this standard is attainable with the existing setup.

Chapter 7

Conclusion and Future Work

The PICO-500 dark matter search experiment, which is the next-generation, tonne-scale bubble chamber detector designed by the PICO collaboration, is expected to achieve world-leading sensitivities in WIMP-proton spin-dependent interactions. This world-leading sensitivity is dependent on minimizing backgrounds through various mitigation methods. Past PICO detectors, such as PICO-60, have demonstrated the importance of proper cleaning protocols to eliminate unexpected events resembling WIMP interactions caused by particulates within the active volume of the detector. These events, termed "anomalous," were effectively addressed by implementing cleaning procedures for the synthetic quartz vessels designed to meet the IEST-STD-CC1246D-25 standard.

In anticipation of ensuring anomaly-free backgrounds in the PICO-500 experiment, customized cleaning systems were developed and tested at the University of Alberta using natural quartz vessels. These systems focused on optimizing cleaning fluid pressure to efficiently remove particulates from the quartz surfaces, preventing contamination through proper system isolation and sealing, mitigating radon exposure using positive-pressure nitrogen gas systems and evacuated volumes, and implementing effective sample collection methods. Despite challenges in consistently meeting the IEST-STD-CC1246D-25 standard in a non-cleanroom environment at the University of Alberta, it was proven that achieving this standard is attainable when robust sample-taking strategies are in place.

The recommissioning of the University of Alberta's radon emanation chamber detector was essential for measuring the radon permeation rate through a Parker spring-energized PTFE seal. This seal is a scaled-down version of those to be used

in the PICO-500 inner vessel. Two independent methods were used to determine the radon permeation coefficient: one using an extrapolation from measurements of the five lower mass noble gases, relating the log of the permeation coefficients to the square of their atomic diameter; the other directly measured radon activity permeating through the seal. The extrapolated radon permeation coefficient was calculated to be $K_p = 5.10^{+0.92}_{-1.10} \times 10^{-10}\ \frac{\mathrm{cm^3(STP)\,cm}}{\mathrm{s\,cm^2\,cm\text{-}Hg}}$, while the direct method provided a coefficient of $K_p = 5.37 \pm 0.49 \times 10^{-10}\ \frac{\mathrm{cm^3(STP)\,cm}}{\mathrm{s\,cm^2\,cm\text{-}Hg}}$. These results are in agreement within their respective errors. Furthermore, this study opens up future research areas, including investigating the temperature dependence of the radon permeation coefficient of the Parker PTFE seal. Such research would provide a more accurate estimate of the radon permeation rate under the sub-zero (°C) operating temperatures of PICO-500. Based on the experimentally determined radon permeation coefficient at room temperature, an upper limit for the radon activity in the detection volume of PICO-500 due to the emanation and permeation of radon through the Parker PTFE seals was calculated to be 30.5 Radons/day.

The limited research on radon permeation through various sealing materials highlights a significant gap in the scientific literature. There is a growing need for more thorough investigations and standardized methods to accurately determine radon permeation coefficients and rates as low background detectors look to achieve increasingly lower backgrounds. Developing these standardized testing protocols could significantly improve the sensitivity and reliability of future ultra-low background detectors. Additionally, it could lead to a comprehensive catalog of materials with documented radon permeation and emanation rates.

While this thesis focuses on studies tailored for the PICO-500 detector, the ultimate goal would be to guide future research in radon permeation experiments. It aims to serve as a foundation to standardize radon permeation tests, and to contribute to the advancement of radon permeation research, particularly within the context of ultra-low background detectors.

Bibliography

[1] B. Zwicky, J. Meyling, and D. Appell, "Fritz Zwicky and the earliest prediction of dark matter", Physics World **34**, 24 (2021), DOI: 10.1088/2058-7058/34/05/28.

[2] F. Zwicky, "Die Rotverschiebung von extragalaktischen Nebeln", Helvetica Physica Acta **6**, 110–127 (1933).

[3] H. Andernach and F. Zwicky, "English and Spanish Translation of Zwicky's (1933) The Redshift of Extragalactic Nebulae", (2017), arXiv:1711.01693v1 [astro-ph.IM].

[4] Planck Collaboration, N. Aghanim, Y. Akrami, et al., "Planck 2018 results - VI. Cosmological parameters", A&A **641**, A6 (2020), DOI: 10.1051/0004-6361/201833910.

[5] J. L. Feng, "Dark Matter Candidates from Particle Physics and Methods of Detection", Annual Review of Astronomy and Astrophysics **48**, 495–545 (2010), arXiv:1003.0904v2 [astro-ph.CO].

[6] National Nuclear Data Center, Brookhaven National Laboratory, *NuDat (Nuclear Structure and Decay Data)*, Accessed: August 26, 2023, https://www.nndc.bnl.gov/nudat3/.

[7] Parker, *PTFE Seals Design Guide*, (2019), Accessed: August 26, 2023, https://www.parker.com/content/dam/Parker-com/Literature/Praedifa/Catalogs/Catalog_PTFE-Seals_PTD3354-EN.pdf.

[8] V. Rubin and K. Ford, "Rotation of the Andromeda Nebula from a Spectroscopic Survey of Emission Regions", The Astrophysical Journal **159**, 379 (1970).

[9] NASA, CXC, CfA, et al., *1E 0657-56: NASA Finds Direct Proof of Dark Matter*, (2006), Accessed: October 2, 2023, https://chandra.harvard.edu/photo/2006/1e0657/.

[10] E. Hubble and M. Humason, "The Velocity-Distance Relation among Extra-Galactic Nebulae", Astrophysical Journal **74**, 43 (1931).

[11] G. Bertone and D. Hooper, "History of dark matter", Rev. Mod. Phys. **90**, 045002 (2018), DOI: https://doi.org/10.1103/RevModPhys.90.045002.

[12] F. Zwicky, "On the Masses of Nebulae and of Clusters of Nebulae", Astrophysical Journal **86**, 217 (1937), DOI: 10.1086/143864.

[13] E. Corbelli and P. Salucci, "The extended rotation curve and the dark matter halo of M33", Monthly Notices of the Royal Astronomical Society **311**, 441-447 (2000), DOI: 10.1046/j.1365-8711.2000.03075.x.

[14] NASA, ESA, *Hubble captures a "lucky" galaxy alignment*, (2011), Accessed: October 2, 2023, https://esahubble.org/images/potw1151a/.

[15] D. Clowe, M. Bradač, A. H. Gonzalez, et al., "A Direct Empirical Proof of the Existence of Dark Matter*", The Astrophysical Journal **648**, L109 (2006).

[16] ESA and Planck Collaboration, *Planck CMB*, (2013), Accessed: October 2, 2023, https://www.esa.int/ESA_Multimedia/Images/2013/03/Planck_CMB.

[17] C. Alcock, R. A. Allsman, et al., "The MACHO Project: Microlensing Results from 5.7 Years of Large Magellanic Cloud Observations", The Astrophysical Journal **542**, 281 (2000), DOI: 10.1086/309512.

[18] E. Bulbul, M. Markevitch, et al., "Detection of an Unidentified Emission Line in the Stacked X-Ray Spectrum of Galaxy Clusters", The Astrophysical Journal **789**, 13 (2014), DOI: 10.1088/0004-637X/789/1/13.

[19] S. Giagu, "WIMP Dark Matter Searches With the ATLAS Detector at the LHC", Frontiers in Physics **7**, (2019), DOI: 10.3389/fphy.2019.00075.

[20] K. Olive, "Review of Particle Physics", Chinese Physics C **38**, 090001 (2014), DOI: 10.1088/1674-1137/38/9/090001.

[21] J. Aalbers, S. S. AbdusSalam, et al, "A next-generation liquid xenon observatory for dark matter and neutrino physics", **50**, 013001 (2023), DOI: 10.1088/1361-6471/ac841a.

[22] C. A. J. O'Hare, A. M. Green, J. Billard, et al., "Readout strategies for directional dark matter detection beyond the neutrino background", Physical Review D **92**, 063518 (2015), DOI: 10.1103/physrevd.92.063518.

[23] J. Cooley, "Overview of non-liquid noble direct detection dark matter experiments", Physics of the Dark Universe **4**, 92-97 (2014), DOI: https://doi.org/10.1016/j.dark.2014.10.005.

[24] W. M. Haynes et al., *CRC Handbook of Chemistry and Physics*, 95th ed. (Taylor & Francis Group, 2014).

[25] N. Smith, "The SNOLAB deep underground facility", The European Physical Journal Plus **127** (2012).

[26] R. Agnese et al. (SuperCDMS Collaboration), "Projected sensitivity of the SuperCDMS SNOLAB experiment", Phys. Rev. D **95**, 082002 (2017), DOI: 10.1103/PhysRevD.95.082002.

[27] C. E. Aalseth, F. Acerbi, P. Agnes, et al., "DarkSide-20k: a 20 tonne two-phase LAr TPC for direct dark matter detection at LNGS", The European Physical Journal Plus **133**, (2018), DOI: 10.1140/epjp/i2018-11973-4.

[28] E. Aprile et al. (XENON Collaboration), "First dark matter search with nuclear recoils from the XENONnT experiment", Physical Review Letters **131**, (2023), DOI: 10.1103/physrevlett.131.041003.

[29] J. Aalbers et al., "First Dark Matter Search Results from the LUX-ZEPLIN (LZ) Experiment", Physical Review Letters **131**, (2023), DOI: 10.1103/physrevlett.131.041002.

[30] C. Amole et al. (PICO Collaboration), "Dark matter search results from the complete exposure of the PICO-60 C_3F_8 bubble chamber", Physical Review D **100**, (2019), DOI: 10.1103/physrevd.100.022001.

[31] E. Alfonso-Pita, M. Baker, E. Behnke, et al., "Snowmass 2021 Scintillating Bubble Chambers: Liquid-noble Bubble Chambers for Dark Matter and CEνNS Detection", (2022), arXiv:2207.12400 [physics.ins-det].

[32] C. B. Krauss, "PICO-60 Results and PICO-40L Status", Journal of Physics: Conference Series **1468**, 012043 (2020), DOI: 10.1088/1742-6596/1468/1/012043.

[33] G. Giroux, "Search for Dark Matter with the PICO-500 Experiment", Journal of Physics: Conference Series **2156**, 012068 (2021), DOI: 10.1088/1742-6596/2156/1/012068.

[34] J. Marshall and V. Marshall, "Ernest Rutherford the 'true discoverer' of radon", Bull. Hist. Chem. **28** (2003).

[35] World Health Organization, *Radon*, (2023), Accessed: September 12, 2023, https://www.who.int/news-room/fact-sheets/detail/radon-and-health.

[36] J.-X. Wang, T. C. Andersen, and J. J. Simpson, "An electrostatic radon detector designed for water radioactivity measurements", Nuclear Instruments and Methods in Physics Research Section A: Accelerators, Spectrometers, Detectors and Associated Equipment **421**, 601-609 (1999), DOI: https://doi.org/10.1016/S0168-9002(98)01230-3.

[37] Canadian Cancer Society, *Radon*, Accessed: September 12, 2023, https://cancer.ca/en/cancer-information/reduce-your-risk/know-your-environment/radon.

[38] Canadian General Standards Board, "Radon Control Options for New Construction in Low-rise Residential Buildings", (2019).

[39] S. Bruenner, D. Cichon, G. Eurin, et al., "Radon daughter removal from PTFE surfaces and its application in liquid xenon detectors", European Physical Journal C **81**, (2021), DOI: 10.1140/epjc/s10052-021-09047-2.

[40] P. Pagelkopf, M. Gründel, and J. Porstendörfer, "The Charged Fraction of the ^{218}Po Ions in Air Under Environmental", Radioactivity in the Environment **7**, 448-453 (2005), DOI: https://doi.org/10.1016/S1569-4860(04)07052-4.

[41] D. Baxter, "Eliminating Backgrounds in the Search for Dark Matter with the PICO-60 Bubble Chamber", PhD thesis (Northwestern University, 2018).

[42] S. Hanchurak, "Development of a High Sensitivity Radon Emanation Detector", MSc thesis (University of Alberta, 2014).

[43] L. Balogh et al. (NEWS-G collaboration), "The NEWS-G detector at SNOLAB", Journal of Instrumentation **18**, T02005 (2023), DOI: 10.1088/1748-0221/18/02/T02005.

[44] Hamamatsu, *Si PIN Photodiode Datasheet*, (2012), Accessed: September 11, 2023, https://www.hamamatsu.com/content/dam/hamamatsu-photonics/sites/documents/99_SALES_LIBRARY/ssd/s3204-08_etc_kpin1051e.pdf.

[45] L. Landau, "On the energy loss of fast particles by ionization", J. Phys. (USSR) **8**, 201–205 (1944).

[46] P. Vavilov, "Ionization losses of high-energy heavy particles", Sov. Phys. JETP **5**, 749–751 (1957).

[47] S. Pommé and B. Caro Marroyo, "Improved peak shape fitting in alpha spectra", Applied Radiation and Isotopes **96**, 148-153 (215), DOI: https://doi.org/10.1016/j.apradiso.2014.11.023.

[48] Pylon Electronics Inc., *Datasheet for Radon Calibration Source RN-1025*, (2019), Accessed: September 12, 2023, https://pylonelectronics-radon.com/wp-content/uploads/2019/08/DS123R4-RN-TH-1025.pdf.

[49] S. Matteucci et al., *Transport of Gases and Vapors in Glassy and Rubbery Polymers*, (John Wiley & Sons, Ltd, 2006), https://onlinelibrary.wiley.com/doi/pdf/10.1002/047002903X.ch1.

[50] T. Graham, "On the Absorption and Dialytic Separation of Gases by Colloid Septa", Philosophical Transactions of the Royal Society of London **156**, 399–439 (1866).

[51] R. H. Petrucci, W.S. Harwood, and F.G. Herring, *General Chemistry: Principles and Modern Applications*, 8th ed. (Prentice Hall, 2002).

[52] J. Wisniak, "Thomas Graham. II. Contributions to diffusion of gases and liquids, colloids, dialysis, and osmosis", Educación Química **24**, 506-515 (2013), DOI: https://doi.org/10.1016/S0187-893X(13)72521-7.

[53] L. S. H. Czichos T. Saito, *Springer Handbook of Materials Measurement Methods*, Springer Handbook of Materials Measurement Methods (Springer Berlin Heidelberg, 2007).

[54] T.C. Merkel et al, "Gas Sorption, Diffusion, and Permeation in Poly(2,2-bis(trifluoromethyl)-4,5-difluoro-1,3-dioxole-co-tetrafluoroethylene)", Macromolecules **32**, 8435 (1999), DOI: 10.1021/ma990685r.

[55] S.J. Schowalter, C.B. Connolly, and J.M. Doyle, "Permeability of noble gases through Kapton, butyl, nylon, and 'Silver Shield'", Nuclear Instruments & Methods in Physics Research Section A-Accelerators Spectrometers Detectors and Associated Equipment **615**, 267-271 (2010), DOI: 10.1016/j.nima.2010.01.041.

[56] Omega Engineering, Inc., *PX119 Series Compact Pressure Transducers*, Accessed: March 20, 2024, https://assets.omega.com/pdf/test-and-measurement-equipment/pressure/pressure-transducers/PX119.pdf.

[57] INFICON, *PxG55x Series Operating Manual*, Accessed: March 20, 2024, https://www.inficon.com/media/5795/download/TINA56E1_PxG55x_Operating-manual.pdf?v=1&inline=true&language=en.

[58] Innovative Sensor Technology, *TSic50x Series Temperature Sensors*, Accessed: March 20, 2024, https://www.ist-ag.com/sites/default/files/downloads/DTTSic50x_E.pdf.

[59] M. Silberberg, *Chemistry: The Molecular Nature of Matter and Change*, 7th ed. (McGraw-Hill Education, New York, 2015).

[60] International Organization for Standardization, *Plastics — film and sheeting — determination of gas-transmission rate — part 1: differential-pressure method*, ISO 15105-1, (2002).

[61] D. W. Breck, *Zeolite Molecular Sieves: Structure, Chemistry, and Use* (Wiley, New York, 1974).

[62] H. G. Hammon, K. Ernst, and J. C. Newton, "Noble gas permeability of polymer films and coatings", J. Appl. Polym. Sci. **21**, 1989-1997 (1977), DOI: 10.1002/app.1977.070210725.

[63] SNOLAB, *Gamma Detector Counting Results*, (2020), Accessed: March 20, 2024, https://www.snolab.ca/users/services/gamma-assay/HPGe_samples_pico_master.html.

[64] K. Dering, *PICO-500 bubble chamber PV design conditions & loading*, PICO, QUDO-PFH-SK-0000-01 Rev 00, (2021), Accessed: March 20, 2024.

[65] D. Chauhan, "Radon Emanation of PICO 40L vessel for the PICO Experiment Using SNOLAB's Surface Radon Board System", Internal Document, (2022).

[66] B. Singh, S. Singh, and H. Virk, "Radon diffusion studies in air, gravel, sand, soil and water", Nuclear Tracks and Radiation Measurements **22**, 455-458 (1993), DOI: 10.1016/0969-8078(93)90107-F.

[67] P. Mitra, "PICO-60: A Dark Matter Search Experiment with C_3F_8 in a Bubble Chamber", PhD thesis (University of Alberta, 2018).

[68] E. N. Borson, "IEST-STD-CC1246D: Product Cleanliness Levels and Contamination Control Program", CleanRooms (2005).

[69] PICO Collaboration, *PICO-500 Dishwasher Manual and Training Procedures*, Document Number: PICO-PFH-DET-1007, (2024).

[70] Graver Technologies, *TefTEC Filtration Solutions Catalog*, (2022), Accessed: March 8, 2024, https://assets-global.website-files.com/605bb73f62e039589786b760/633c88415ed8d3499a20586e_TefTEC-10-22.pdf.

[71] Spraying Systems Co., *Full cone spray nozzle datasheet*, (2023), Accessed: March 8, 2024, Spray.com, https://www.spray.com/-/media/dam/industrial/usa/sales-material/catalog/cat75hyd_us_full-cone_b.pdf.

[72] Spraying Systems Co., *Tankjet 27500 tank cleaning catalog*, (2023), Accessed: March 8, 2024, Spray.com, https://www.spray.com/-/media/dam/industrial/usa/sales-material/excerpt/tankjet_27500_tank-cleaning-catalog.pdf.

Appendix A: Radon Emanation Rate of the Parker PTFE Seals

A PICO-500 scale Parker PTFE seal was provided to Queen's University for radon emanation rate measurements during a time when the UofA radon emanation detector was temporarily out of service. Consecutive evaluations of the emanation rate were conducted utilizing the Lucas cell method. The first measurement indicated a radon emanation rate of -5.00 $\pm$ 15.84 Radons/day, and the second measurement showed a rate of 22.73 $\pm$ 18.97 Radons/day. The negative emanation rate observed in the first measurement, with error margins that include zero, is interpreted as a statistical artifact. The weighted average of these two measurements yields a radon emanation rate of 6.39 $\pm$ 12.16 Radons/day. Detailed summaries and background rates of each measurement are provided in the following two pages for further reference.

PICO 1st Extraction O-Ring

Inputs

Date	**Mar 30,2022**	uncertainty
Chamber	**3**	
Lucas cell #	**4**	
Source material		
Weight (kg)	**0.000**	n/a
Surface area (m^2)	**0.000**	n/a
Emanation time (days)	**5.000**	n/a
Counting time (days)	**2.927**	n/a
Number of counts	**76**	12.99
Lucas cell background (counts/day)	**16.11**	**4**
Chamber background emitter rate (atoms/day)	**25**	**10**

Constants

Rn-222 half-life	3.8235	n/a
Rn-222 decay constant (day^-1)	0.1813	n/a
Lucas cell single-alpha efficiency (SNO)	0.74	0.04
Efficiency from concentrator trap to cell (SNO)	0.64	0.03
Efficiency from primary to concentrator trap	0.75	0.04
Efficiency from chamber to primary trap (SNO)	1.00	0.05

Output

Counts less Lucas cell background	28.85	17.49
Decayed radon atoms in cell	12.99	7.90
Decayed radon atoms in concentrator trap	20.30	12.39
Decayed radon atoms in primary trap	27.07	16.58
Decayed radon atoms in chamber	27.07	16.63
Radon atoms in chamber when counting started	65.74	40.39
Emission rate (atoms/day)	20.00	12.29
Source emitter rate (atoms/day) =	**-5.00**	15.84
Source emitter rate (atoms/(m^2*h)) =	**#DIV/0!**	#DIV/0!
Source emitter rate (atoms/(kg*day)) =	**#DIV/0!**	#DIV/0!

PICO 2nd Extraction O-Ring

Inputs

Date	**Ap 8, 2022**	uncertainty
Chamber	**3**	
Lucas cell #	**4**	
Source material		
Weight (kg)	**0.000**	n/a
Surface area (m^2)	**0.000**	n/a
Emanation time (days)	**4.000**	n/a
Counting time (days)	**3.095**	n/a
Number of counts	**112**	15.77
Lucas cell background (counts/day)	**16.11**	**4**
Chamber background emitter rate (atoms/day)	**25**	**10**

Constants

Rn-222 half-life	3.8235	n/a
Rn-222 decay constant (day^-1)	0.1813	n/a
Lucas cell single-alpha efficiency (SNO)	0.74	0.04
Efficiency from concentrator trap to cell (SNO)	0.64	0.03
Efficiency from primary to concentrator trap	0.75	0.04
Efficiency from chamber to primary trap (SNO)	1.00	0.05

Output

Counts less Lucas cell background	62.14	20.05
Decayed radon atoms in cell	27.99	9.14
Decayed radon atoms in concentrator trap	43.74	14.44
Decayed radon atoms in primary trap	58.31	19.48
Decayed radon atoms in chamber	58.31	19.70
Radon atoms in chamber when counting started	135.80	45.87
Emission rate (atoms/day)	47.73	16.12
Source emitter rate (atoms/day) =	**22.73**	18.97
Source emitter rate (atoms/(m^2*h)) =	**#DIV/0!**	#DIV/0!
Source emitter rate (atoms/(kg*day)) =	**#DIV/0!**	#DIV/0!

Appendix B: Radon DAQ Runs list

Refer to the tables on the next pages for more details.

Table B.1: Radon measurement results from the vacuum holding tank and emanation chamber detector, analyzed via the Polonium-214 decay channel. The file naming convention is `UofA_Rn_run_XXXX_dd_mm_yyyy`, where `XXXX` represents the sequential number of radon runs.

Description	Run Number	Background Rate (Rn/hour)	Po-214 Decay Channel Efficiency	Source Activity (Bq)	Rn Permeation Rate Constant ($\times 10^{-10}$ s^{-1})	Rn Permeation Coefficient ($\times 10^{-10} \frac{cm^3(STP) \cdot cm}{s \cdot cm^2 \cdot cm\text{-}Hg}$)
Radon Calibration	3123-3227	36 ± 4	-	426	-	-
HV-Efficiency	3230-3249	36 ± 4	-	82	-	-
Emanation System Background	3252-3279	36 ± 4	$(2.343 \pm 0.003)\%$	-	-	-
Radon Permeation of the Parker Seal	3281-3408	36 ± 4	$(2.343 \pm 0.003)\%$	909	206 ± 1	5.33 ± 0.69

Table B.2: Noble gas permeation results from the vacuum holding tank-gas permeation chamber system. The file naming convention is `UofA_Permeation_run_XXXX_dd_mm_yyyy`, where `XXXX` represents the sequential number of noble gas permeation runs.

Gas	Run Number	Initial Pressure (mBar)	Average Temperature (°C)	Gas Volumetric Flow Rate ($\times 10^{-5}$ $\frac{\text{cm}^3\text{(STP)}}{\text{s}}$)	Permeation Coefficient ($\times 10^{-10} \frac{\text{cm}^3\text{(STP)}\cdot\text{cm}}{\text{s}\cdot\text{cm}^2\cdot\text{cm-Hg}}$)
Helium (Heated)	37-40	1647	31.3	19.2 ± 0.4	26.13 ± 3.44
Neon	18-23	1866	23.9	9.7 ± 0.1	12.44 ± 1.71
Argon	8-12	1915	23.8	6.2 ± 0.4	14.22 ± 3.06
Krypton	28-32	1824	23.8	4.4 ± 0.2	8.92 ± 1.72
Xenon	24-27	1770	23.8	4.0 ± 0.2	7.90 ± 1.30

Appendix C: Instrumentation List and Electrical Schematics

Refer to the tables on the next pages for more details.

Table C.1: Instrumentation list of the radon emanation system.
*Denotes a logarithmic calibration scale.

Identifier	Instrument	Make / Model	Range	Uncertainty	Calibration Scale	Calibration Offset
N/A	Vacuum Pump	Adixen ACP-15	-	-	-	-
CP16	Diaphragm Pump	KFN MPU2762-N814	-	-	-	-
FM17	Gas Flow Meter	N/A	0-4 SCFM	±0.5 SFCM	N/A	N/A
PT18*	Pressure Transducer	Inficon PCG550	$5 \times 10^{-5} - 1500$ mBar	±5%	0.0199952	-5.56162
PT19	Pressure Transducer	Omega PX119-030AI	0-30 psia 0-2068 mBar	±1.2 mBar	2.45962 ADC/mBar	-521.913 mBar
PT20*	Pressure Transducer	Inficon PCG550	$5 \times 10^{-5} - 1500$ mBar	±5%	0.00976562	-5.5
TT21	Temperature Sensor	IST TSic 501F	-10-60°C	±0.07°C	0.0683594 ADC/°C	-10°C
TT22	Temperature Sensor	IST TSic 501F	-10-60°C	±0.07°C	0.0683594 ADC/°C	-10°C
TT23	Temperature Sensor	IST TSic 501F	-10-60°C	±0.07°C	0.0683594 ADC/°C	-10°C
TT24	Temperature Sensor	IST TSic 501F	-10-60°C	±0.07°C	0.0683594 ADC/°C	-10°C
HV	High Voltage	Bertan 375N	0-5 kV	±10 V	9.92771 ADC/V	0 V
RN-1025	Radon-222 Source	Pylon RN-1025	0-930 Bq	N/A	-	-

Table C.2: Instrumentation list of the PICO-500 Cleaning Cart (Dishwasher).

Identifier	Instrument	Make / Model	Range	Calibration Scale	Calibration Offset
PT35	Pressure Transducer	Omega PN: PX309-150GI	0-150 psi	9375 psi/mA	-37.5 psi
pHT36	pH Transducer	GF Piping Systems Electrode: Signet 3-2734 Sensor: 2751	0-14	875 pH/mA	-3.5 pH
PT37	Pressure Transducer	ICON PN: LP150-PF	0-150 psi	9375 psi/mA	-37.59375 psi
TT38	Thermocouple	Omega PN: SA1 Series	0-175°C	25718.8°C/mV	18.99°C
PT39	Pressure Sensor	Omega PN: PX309-150GI	0-150 psi	9375 psi/mA	-37.5 psi
TT40	Thermocouple	Omega PN: SA1 Series	0-175°C	25274.7°C/mV	18.98°C
TT41	Thermocouple	Omega PN: SA1 Series	0-175°C	25718.8°C/mV	18.99°C
TT42	Thermocouple	Omega PN: SA1 Series	0-175°C	25474.7°C/mV	19.28°C

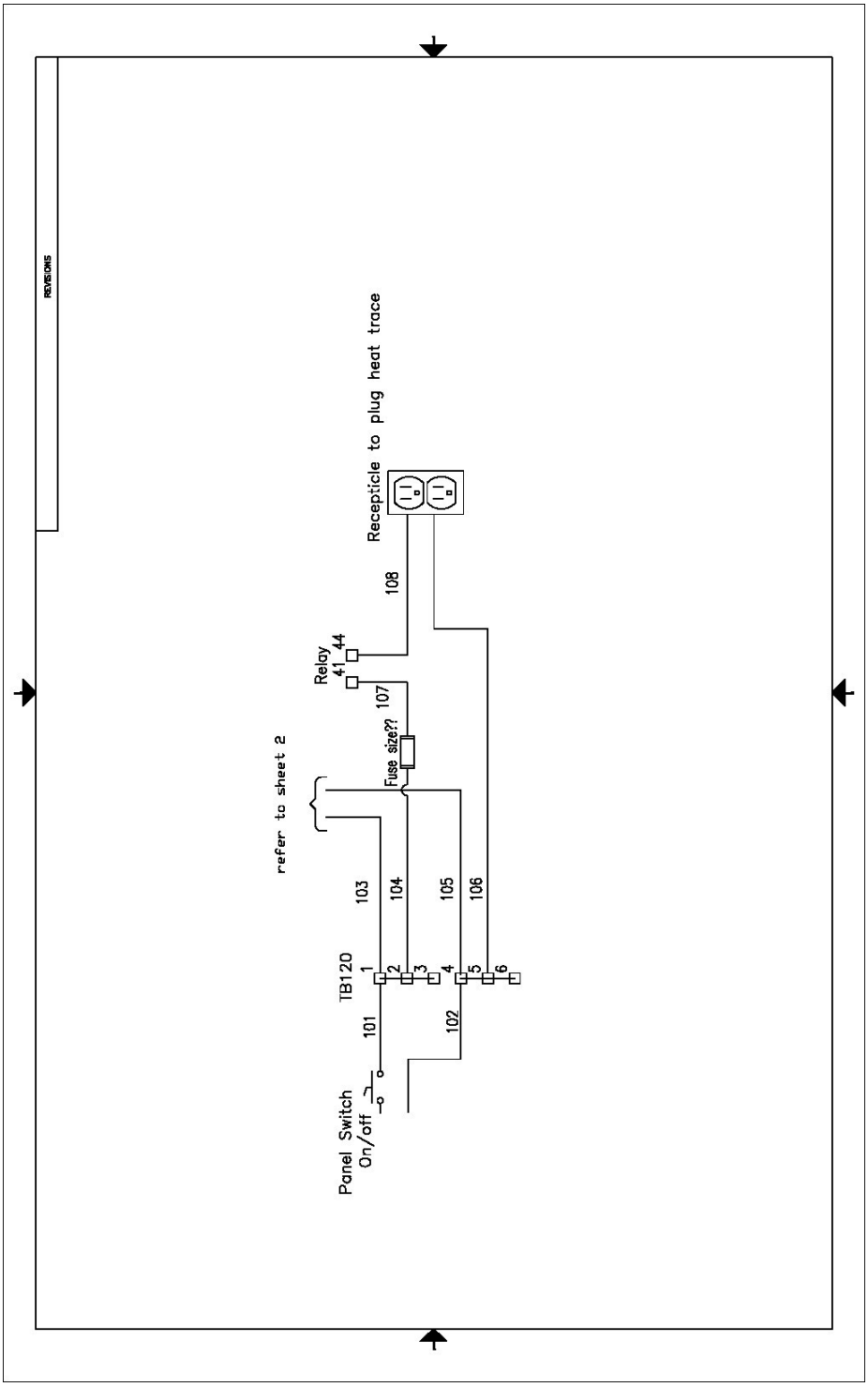

Figure C.1: Electrical schematic of the 120 V circuit for the PICO-500 Dishwasher with a panel switch, terminal block TB120, a relay, and a receptacle for the two heat traces.

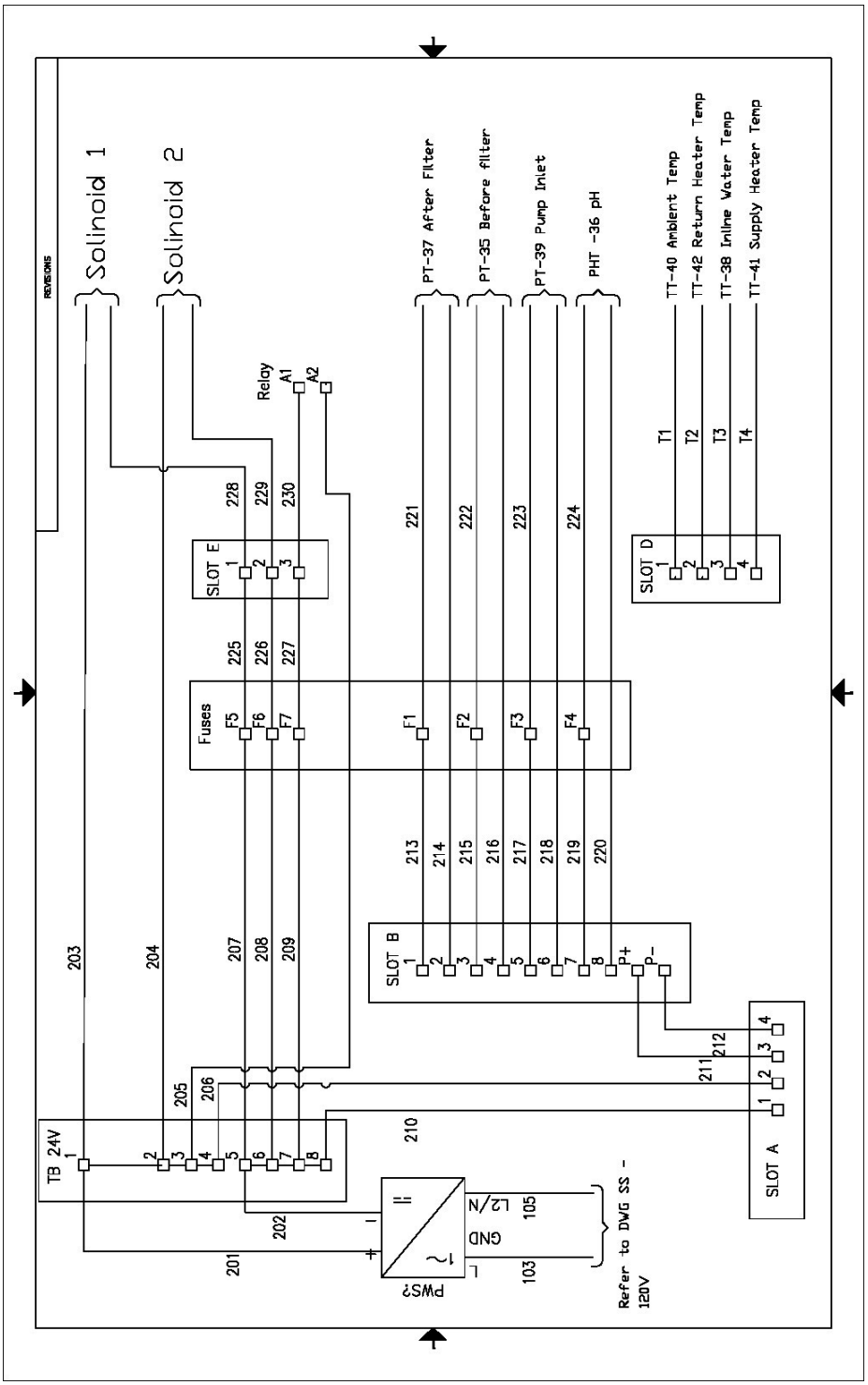

Figure C.2: Electrical schematic diagram of the 24 V circuit for the PICO-500 Dishwasher.

Appendix D: Permeation Coefficient Conversion Table

The table on the following page presents experimentally determined permeation coefficients for each noble gas, expressed in various units.

Table D.1: Permeation coefficients of the six noble gases through a Parker flange seal Prädifa series NAE, FlexiSeal® in various units.
*Denotes the unit conversion using the standard unit 1 Barrer as the reference.

Gas	$\times 10^{-10}\,\frac{\mathrm{cm^3(STP)\cdot cm}}{\mathrm{s\cdot cm^2\cdot cm\text{-}Hg}}$	Barrer	$\times 10^{-15}\,\frac{\mathrm{mol}}{\mathrm{s\cdot m\cdot Pa}}$	$\times 10^{-16}\,\frac{\mathrm{mol\cdot mm}}{\mathrm{s\cdot cm^2\cdot Pa}}$	$\times 10^{-22}\,\frac{\mathrm{cm^3(STP)\cdot mm}}{\mathrm{Day\cdot cm^2\cdot \frac{Bq}{m^3}}}$
Helium (Heated)	26.13 ± 3.44	26.13 ± 3.44	8.75 ± 1.15	8.75 ± 1.15	-
Neon	12.44 ± 1.71	12.44 ± 1.71	4.16 ± 0.57	4.16 ± 0.57	-
Argon	14.22 ± 3.06	14.22 ± 3.06	4.76 ± 0.10	4.76 ± 0.10	-
Krypton	8.92 ± 1.72	8.92 ± 1.72	2.99 ± 0.58	2.99 ± 0.58	-
Xenon	7.90 ± 1.30	7.90 ± 1.30	2.64 ± 0.44	2.64 ± 0.44	-
Radon	5.37 ± 0.49	5.37 ± 0.49	1.80 ± 0.16	1.80 ± 0.16	6.72 ± 0.62
*Conversion	1×10^{-10}	1	3.348×10^{-16}	3.348×10^{-17}	1.25×10^{-22}